Joint application of ground-based transient electromagnetics and airborne electromagnetics

I n a u g u r a l – D i s s e r t a t i o n

zur

Erlangung des Doktorgrades

der Mathematisch-Naturwissenschaftlichen Fakultät

der Universität zu Köln

vorgelegt von

Annika Steuer

aus Köln

2008

Berichterstatter:	Prof. Dr. Bülent Tezkan
	Prof. Dr. Andreas Kemna
Tag der mündlichen Prüfung:	26. November 2008

ABSTRACT

The focus of this thesis lies on the joint application of ground-based and airborne electromagnetic methods for the investigation of a glacial valley. For the first time two different airborne electromagnetic (AEM) surveying methods were employed to determine the resistivity structure of a single geological target: the frequency-domain helicopter-borne electromagnetic (HEM) system operated by the Federal Institute for Geosciences and Natural Resources (BGR), Germany, and the time-domain SkyTEM system developed at the University of Aarhus, Denmark. For verification of the airborne results, ground-based transient electromagnetics (TEM) and 2D resistivity surveying were also performed.

The target survey area was the Cuxhaven valley in northern Germany, a significant local groundwater reservoir. The course of this buried valley was revealed by drillings, and the shape determined by reflection seismics along several transects across the valley. Electrical and electromagnetic methods were applied to investigate the structure of the valley fill, consisting of gravel, sand, silt and clay. Here, the extension and the thickness of clay layers are of particular interest. They have a low hydraulic permeability and often serve as protection for underlying aquifers against pollution from the surface.

The HEM survey clearly resolves a thin conductive layer at 20 m depth and a deeper conductive layer below 40 m depth inside the valley. These layers are confirmed by 2D resistivity survey results and identified by a lithological log as clay layers. The thickness of the deeper clay is not definitely determined by standard HEM inversions due to the limited investigation depth of the HEM system. In contrast, the SkyTEM survey does not resolve the shallow clay, but does resolve the thickness of the deeper one inside the valley, and reveals an additional conductive layer at about 180 m depth outside the valley. The SkyTEM results are consistent with ground-based TEM soundings. Neither the frequency-domain method nor the normal-moment time-domain methods were able to detect the base of the valley using conventional interpretation methods. Solely high-moment ground-based TEM measurements determined a resistivity contrast at about 300 m depth, which matches with the Quaternary base known from a seismic section.

The standard tools for presenting AEM data are apparent-resistivity maps and resistivity-depth sections. Although the large and dense data sets are favorable for 3D interpretation, it is still not common to perform 3D inversion in AEM, as the effort in terms of computing time is too high. Therefore, 1D inversion models are still used to display 3D resistivity distributions by stitching together the 1D layered inversion models. Besides the 3D inversion the combination of different data sets in one inversion scheme is an ongoing research issue. One approach is the classical joint inversion, which results in one resistivity model at the shared survey sites, whereas each site is regarded as individual. In this thesis I follow a different approach: spatially constrained inversion (SCI).

SCI is a technique where different data sets are combined in one inversion scheme and spatial constraints are applied to the resistivity structure revealed at adjacent survey sites. Thus, the method is particularly useful for large data sets as obtained in AEM. Using spatial constraints, information can be propagated horizontally to

adjacent models. With this technique it is then possible to resolve layers which are locally poorly resolved. SCI was originally developed at University of Aarhus for SkyTEM data. In this thesis I adapt the technique for the use on HEM data and apply it to both, SkyTEM and HEM data of the Cuxhaven valley using *a priori* information from geology, drilling, and seismics.

Systematic studies of the SCI parameters show that a) the inversion results applying SCI are less dependent on the starting model in comparison to single-site inversion, b) HEM data resolve the base of a conductive layer which can be identified as the Lauenburg clay, and c) SkyTEM data reveal the base of the Cuxhaven valley which is also confirmed by a seismic section and high-moment TEM measurements.

The influence of the valley geometry on the 1D inversion results were systematically studied by 3D forward modeling of different slope geometries. 1D inversions of the synthetic data across the slope were performed with and without constraints between neighboring sites. The resulting 1D models are affected by the slope and simulate a valley base at shallower depth than in the 3D model. Using constraints again decreases the dependency on the starting model.

This thesis demonstrates that 1.) by the joint application of ground-based and airborne electromagnetic methods, 2.) by the application of the SCI including *a priori* information and 3.) by explaining 2D effects of valley slopes using a 3D forward code, a better understanding of the structure of the Cuxhaven valley is obtained.

ZUSAMMENFASSUNG

Ein Schwerpunkt dieser Arbeit ist die gemeinsame Anwendung von boden- und aerogeophysikalischen Methoden zur Erkundung einer eiszeitlichen Rinne. Hier wurden erstmals zwei verschiedene aeroelektromagnetische Methoden eingesetzt, um die Widerstandsstruktur in einem Messgebiet zu bestimmen: das HEM-System, das im Frequenzbereich misst und von der Bundesanstalt für Geowissenschaften und Rohstoffe (BGR) betrieben wird und das SkyTEM-System, das im Zeitbereich misst und an der Universität von Aarhus entwickelt wurde. Zur Verifikation der aeroelektromagnetischen Ergebnisse wurden bodengeophysikalische Messungen des elektrischen Widerstandes im vergleichbaren Tiefenbereich mit folgenden Methoden durchgeführt: Transient-Elektromagnetik und 2D-Geoelektrik.

Das Messgebiet war die Cuxhavener Rinne in Norddeutschland, ein wichtiges, lokales Grundwasserreservoir. Der Verlauf der Rinne wurde durch Bohrungen ermittelt und die Form wurde mit Reflexionsseismik entlang einiger die Rinne kreuzenden Profile bestimmt. Elektrische und elektromagnetische Methoden wurden angewendet, um die Struktur der Rinnenfüllung zu untersuchen, die aus Kiesen, Sanden und Tonen besteht. Besonders interessant ist hierbei die Ausdehnung und die Dicke von Tonschichten. Diese besitzen eine geringe hydraulische Permeabilität und dienen damit häufig zum Schutz der darunterliegenden grundwasserführenden Schichten vor Verschmutzungen von der Erdoberfläche.

Innerhalb der Rinnen lösen die HEM-Messungen deutlich eine dünne leitfähige Schicht in 20 m Tiefe und einen tiefer gelegenen Leiter ab 40 m Tiefe auf. Diese Schichten werden durch Ergebnisse von 2D-Geoelektrik Messungen bestätigt und mithilfe eines lithologischen Profils als Tonschichten identifiziert. Die Mächtigkeit der tiefer liegenden Tonschicht kann aufgrund der begrenzten Eindringtiefe nicht ohne weiteres mit HEM bestimmt werden. Im Gegensatz dazu lösen die SkyTEM-Messungen nicht die oberflächennahe Tonschicht auf, dafür aber die Mächtigkeit der tieferen Tonschicht innerhalb der Rinne, und sie ermitteln eine weitere leitfähige Schicht in etwa 180 m Tiefe außerhalb der Rinne. Die SkyTEM-Ergebnisse stimmen mit bodengestützten TEM-Messungen überein. Weder die Frequenzbereichs- noch die Zeitbereichsmethoden (mit gewöhnlichem Sendemoment) können mit konventionellen Interpretationsverfahren die Basis der Rinne detektieren. Lediglich bodengestützte TEM-Messungen mit sehr großem Sendemoment ermitteln einen Widerstandskontrast in etwa 300 m Tiefe, der mit der Quartärbasis übereinstimmt, welche aus einer Seismiksektion bekannt ist.

Standardmäßig werden aeroelektromagnetische Daten als Karten des scheinbaren spezifischen Widerstands und als Widerstands-Tiefen-Schnitte präsentiert. Obwohl sich die großen und dichten Datensätze dafür anbieten, ist es aufgrund der sehr hohen Rechenzeiten in der Aeroelektromagnetik immer noch nicht üblich 3D-Inversionen durchzuführen. Stattdessen werden 1D-Inversionsmodelle benutzt, um 3D-Widerstandsverteilungen durch die Aneinanderreihung der geschichteten Halbraummodelle darzustellen. Neben der 3D-Inversion ist die Verknüpfung verschiedener Datensätze in einem Inversionsverfahren zur Zeit ein aktuelles Forschungsthema. Ein Ansatz stellt die klassische 1D *joint inversion* dar, dessen Ergebnis ein Widerstandsmodell an den gemeinsamen Messpunkten ist, wobei jeder Messpunkt

für sich betrachtet wird. In dieser Arbeit bin ich einem weiteren Ansatz nachgegangen: *spatially constrained inversion* (SCI, räumlich verknüpfte Inversion).

Die SCI ist eine Inversionstechnik die von der hohen Datendichte auf andere Art und Weise profitiert indem sie gleichzeitig mehrere Datensätze in einem Inversionsschema miteinander verknüpft. Durch das Setzen von Randbedingungen, so genannten *constraints*, können Informationen zu benachbarten Modellen verteilt werden. Mit dieser Technik ist es dann möglich, Schichten aufzulösen, die lokal schwach aufgelöst sind. Die SCI wurde an der Universität von Aarhus für SkyTEM-Daten entwickelt. Ich habe diese Technik für die Anwendung auf HEM-Daten adaptiert und sie auf SkyTEM- und HEM-Daten der Cuxhavener Rinne unter Einbeziehung von *a priori* Informationen angewendet.

Systematische Untersuchungen der SCI Parameter zeigen: a) Ergebnisse der SCI sind weniger abhängig vom Startmodell als die der Einzelinversionen, b) durch die Hinzunahme von Randbedingungen lösen HEM-Daten die Basis der tiefer gelegenen Tonschicht auf, die als Lauenburger Ton identifiziert wurde und c) SkyTEM-Daten ermitteln die Basis der Cuxhavener Rinne, die durch eine Seismiksektion und TEM-Messungen mit großem Sendemoment bestätigt wird.

In einer Modellstudie untersuche ich, inwieweit sich die Simplifizierung der Rinnenstruktur auf 1D-Schichtmodelle an den Messpunkten auswirkt. Hierbei modelliere ich mit einem 3D-Vorwärtsprogramm TEM-Daten entlang eines Querprofiles über 2D-Rinnenstrukturen mit unterschiedlichen Geometrien. Anschließend invertiere ich die synthetischen Daten mit einem 1D-Inversionsprogramm mit und ohne *constraints*. Die resultierenden 1D-Modelle werden durch die Rinnenflanken beeinflusst und simulieren eine flachere Rinnenbasis. Durch die Verwendung der *constraints* nimmt die Abhängigkeit von der Wahl des Startmodells ab.

Diese Arbeit zeigt, dass 1.) durch die gemeinsame Anwendung boden- und luftgestützter elektromagnetischer Methoden, 2.) durch die Anwendung von SCI unter Einbeziehung von *a priori* Informationen und 3.) durch die Erklärung von 2D-Effekten der Rinnenflanken mithilfe einer 2D-Modellstudie, ein besseres Verständniss der Struktur der Cuxhavener Rinne erreicht wird.

Contents

List of Figures

List of Tables

Chapter 1

Introduction

Keeping in mind the words of *Box* [1979]: "All models are wrong — (but) some are useful.", in this work I take you on "The search for a useful model ...".

1.1 EM methods for hydrogeological investigations

Electric and electromagnetic (EM) methods are the most important geophysical techniques for groundwater studies [*Nobes*, 1996] and they are frequently used for the characterization of sedimentary aquifers. Hydrogeological structures can be derived from the electrical conductivity distribution of the subsurface. The sensitivity of these geophysical techniques to the conductivity structure is caused by variations in porosity, water saturation, conductivity of the pore fluid, and clay content [*Archie*, 1942].

General discussions on the use of EM techniques for shallow geophysical applications including groundwater studies are found in, *e.g.*, *McNeill* [1990], *Nobes* [1996], *Tezkan* [1999], and *Pellerin* [2002]. Several case histories for the successful application of EM methods in hydrogeological investigations have been published, *e.g.*, by *Palacky* [1983]. *Turberg et al.* [1994] presented the results of a hydrogeological investigation of porous environments using the radio-magnetotelluric (RMT) technique. They showed a correlation between the geophysical and the lithological heterogeneity and an indirect relation to the hydraulic behavior of the aquifer system. *Fitterman and Stewart* [1986] applied transient electromagnetics (TEM) to different groundwater exploration problems, *Christensen and Sørensen* [1998] and *Auken et al.* [2003] used the TEM method for hydrogeophysical investigations in Denmark.

As EM methods are based on the propagation of EM fields, both, ground-based and airborne electromagnetic (AEM) measurements are feasible. The first AEM system, a fixed-wing system operated in frequency-domain, was tested successfully in Canada in 1948 [*Fountain*, 1998], and the heyday of AEM began with mineral exploration. Since then, technological innovations have been fast-paced. With the development of multi-frequency high-resolution helicopter EM systems (HEM), the focus steered away from mineral exploration and moved towards environmental and groundwater applications. In the past decade developments in helicopter

time-domain systems proceeded in such a way, that high-resolution measurements are now possible also in time-domain. *Fountain* [1998], *Witherly* [2000], *Nabighian and Macnae* [2005], and *Fountain* [2008] present historical reviews on AEM. Recent examples for helicopter-borne groundwater investigations with frequency-domain systems are given in *Siemon et al.* [2004; 2007*b*] and *Steuer* [2008], and with time-domain systems in: *Jørgensen et al.* [2006], *Kjærstrup and Erfurt* [2006], and *Scheer et al.* [2006].

Different EM methods can be jointly used to reduce the layer equivalences, which is an inherent problem in EM modeling, and thus enhance model resolution. *Schwarz and Krüger* [1997], for example, combined RMT and TEM for groundwater prospecting. *Meju et al.* [1999] combined vertical electrical soundings (VES), TEM and audio magnetotellurics (AMT) to map an aquifer in the Parnaiba Basin in the northeast of Brazil and showed that a combination of different methods helps to overcome the equivalence problem. HEM and TEM have been successfully combined for hydrogeological investigations, *e.g.*, by *Fitterman and Deszcz-Pan* [2001] for saltwater mapping in the Everglades National Park in Florida, USA, and by *Stadtler et al.* [2004] for groundwater studies in Namibia.

1.2 EM modeling and inversion

The standard tools for presenting AEM data are apparent-resistivity maps and conductivity-depth sections. As 1D inversion is the state of the art, cross sections are derived from stitched together layered half-space models.

As the effort in terms of computing time is too high, it is still not common to perform 3D inversion in AEM, although the large and dense data sets are favorable for 3D interpretation, and 1D inversion models are still used to display the 3D resistivity distribution. *Hodges and Siemon* [2008] present a comparison of several 1D inversion approaches applied on HEM data, for example, differential resistivity conductivity-depth transforms [*Macnae et al.*, 1998], SVD-Marquardt discrete layer inversion [*Huang and Palacky*, 1991], laterally constrained inversion (LCI) [*Siemon et al.*, 2007*a*] and simulated annealing [*Yin and Hodges*, 2007]. Spatially constrained inversion (SCI) is a 1D inversion technique to benefit from large and dense data sets in another way. It was developed at *Aarhus University* for the inversion of airborne TEM data [*Viezzoli et al.*, 2008]. Through spatial constraints information can be spread horizontally to adjacent models. This technique enables one to resolve layers which are otherwise locally poorly resolved.

For multi-dimensions there are several developments as well in both modeling and inversion. For direct current and magnetotelluric data 2D inversions are common, *e.g.*, *Siripunvaraporn and Egbert* [2000] and *Rodi and Mackie* [2001]. Approaches for 3D inversion in time-domain are, *e.g.*, *Newman and Commer* [2005] and *Commer* [2003] with a 3D constrained inversion. *Ellis* [1998] and *Chen et al.* [1998] presented a 2.5D inversion on AEM data and *Xie and Li* [1999] proposed an algorithm for 3D EM inversion. A review of 3D EM modeling and inversion can be found in *Oristaglio and Spies* [1999].

1.3 This thesis

In Chapter 2 I give a short introduction to EM theory. I present the basic Maxwell equations and the derivation of the wave equations with their solutions for the methods used in this study.

Chapter 3 gives an introduction to conventional 1D inversion theory and evaluation. Additionally, the theory of recent approaches, such as laterally and spatially constrained inversion, are described.

Chapter 4 reports on a field example for the application of EM methods in groundwater investigations. The investigation target is the buried Cuxhaven valley in northern Germany, which is a significant local groundwater reservoir. After a short introduction to buried valleys in general, the location and the geology of the Cuxhaven valley are described. Furthermore, the geophysical surveys and systems with their basic data analysis are described in the order they were acquired at the Cuxhaven valley. The focus is on AEM methods: the frequency-domain HEM system operated by the Federal Institute for Geosciences and Natural Resources, Germany, and the time-domain SkyTEM system developed at Aarhus University, Denmark. I compare the airborne 1D inversion results in detail with the results of established ground-based geophysical methods such as the continuous vertical electrical sounding (CVES) method and TEM and discuss the advantages, disadvantages and limitations of each helicopter-borne EM method.

In Chapter 5, additional to single-site 1D inversion techniques I applied spatially constrained inversion (SCI). I adapted the SCI technique, which was developed for SkyTEM data, for the use on HEM data and applied it on the HEM and SkyTEM data of the Cuxhaven valley involving *a priori* information. I studied the influence of the starting models, different strengths and weightings of the constraints and compared the SCI results to single-site inversion results.

In Chapter 6 I show the results of a 3D modeling study to determine the sensitivity of 1D inversions to multidimensional structures, like buried valleys. I modeled transients at a section over 2D valleys with different depths, widths and slopes, using the 3D modeling code of *Druskin and Knizhnerman* [1988]. After finding a suitable grid, I compared the calculated transients at the center of the valleys with the transient of the corresponding layered half-space, to get an impression of the 2D effects on the data. Then I analyzed the influence on the 1D inversions by inverting the synthetic data with and without constraints on the model parameters.

Chapter 7 concludes the main results of the field example, the investigation with the SCI and the 3D modeling study.

Chapter 2

Methods

Electrical and electromagnetic methods provide information about the subsurface resistivity distribution. As current is injected directly into the subsurface, direct current (DC) electrical methods must necessarily be applied on the ground. Electromagnetic (EM) methods are based on the propagation of EM fields, which induce currents in the subsurface and therefore both ground-based and airborne EM measurements are feasible. EM methods are categorized into frequency-domain and time-domain methods.

A successful application of DC and EM methods for differentiating subsurface resistivity structures requires a sufficiently large resistivity contrast between the target and the surrounding material. Both methods are often used in hydrogeological surveys to differentiate conductive formations such as clay-bearing layers, which can be aquitards, from more resistive ones such as gravel and sand layers, which often serve as productive aquifers. As the electrical conductivity of groundwater depends on its mineral content, DC and EM methods are useful to distinguish between fresh-, brackish-, and saltwater.

2.1 Basics of EM

The basic equations of electromagnetism can be found in many physics books. I will present them since they are essential for the understanding of the EM methods in geophysics and for the derivation of quantities such as: diffusion depth, skin depth, and so forth.

EM methods are applied in geophysical explorations to exploit the electrical conductivity σ of the ground. The property of the electrical conductivity is a determining factor for the propagation of EM waves in a medium.

Table 2.1 gives an overview of the used quantities and their units.

Meaning	Symbol	SI Unit
electric field	$\mathbf{E}$	$\frac{\mathrm{V}}{\mathrm{m}}$
(electric field intensity)		
electric displacement field	$\mathbf{D}$	$\frac{\mathrm{As}}{\mathrm{m}^2}$
(electric flux density)		
magnetic field	$\mathbf{B}$	$\mathrm{T} = \frac{\mathrm{Vs}}{\mathrm{m}^2}$
(magnetic flux density)		
magnetic field intensity	$\mathbf{H}$	$\frac{\mathrm{A}}{\mathrm{m}}$
current density	$\mathbf{j}$	$\frac{\mathrm{A}}{\mathrm{m}^2}$
electric charge	q	$\frac{\mathrm{As}}{\mathrm{m}^3}$
electrical permittivity	$\epsilon = \epsilon_0 \epsilon_r$	$\frac{\mathrm{As}}{\mathrm{Vm}}$
permittivity of free space	$\epsilon_0 = 8.854 \cdot 10^{-12}$	$\frac{\mathrm{As}}{\mathrm{Vm}}$
dielectric constant	ϵ_r	non-dimensional
magnetic permeability	$\mu = \mu_0 \mu_r$	$\frac{\mathrm{Vs}}{\mathrm{Am}}$
permeability of free space	$\mu_0 = 4\pi \cdot 10^{-7}$	$\frac{\mathrm{Vs}}{\mathrm{Am}}$
relative permeability	μ_r	non-dimensional
electrical conductivity	σ	$\frac{\mathrm{S}}{\mathrm{m}} = \frac{\mathrm{A}}{\mathrm{Vm}}$
resistivity	ρ	$\Omega\mathrm{m} = \frac{\mathrm{Vm}}{\mathrm{A}}$
frequency	f	$\mathrm{Hz} = \frac{1}{\mathrm{s}}$
angular frequency	$\omega = 2\pi f$	$\frac{1}{\mathrm{s}}$
angular wavenumber	k	non-dimensional
Del operator	$\nabla = (\frac{\partial}{\partial x}, \frac{\partial}{\partial y}, \frac{\partial}{\partial z})$	non-dimensional
Laplace operator	$\delta = \nabla^2 = \frac{\partial^2}{\partial x^2} + \frac{\partial^2}{\partial y^2} + \frac{\partial^2}{\partial z^2}$	non-dimensional

Table 2.1: *Variables, constants, and differential operators in electromagnetism. Vectors and matrices are represented by bold characters.*

2.1.1 Maxwell's equations

The propagation of EM fields in a homogeneous infinite medium is described by Maxwell's equations:

1. **Gauss's Law:** The field of an isolated electric charge q can be represented by field lines that radiate outward:

$$\nabla \cdot \mathbf{D} = q.$$

   In a neutral medium the electric charge (density) can be neglected: $q \approx 0$.

2. **Gauss's Law for magnetism:** The divergence of a magnetic field is always zero and hence magnetic field lines are solenoidal:

$$\nabla \cdot \mathbf{B} = 0.$$

3. **Faraday's Law of induction:** Moving a conductor through a magnetic field produces an electromotive force which is directly proportional to the speed of movement:
$$\nabla \times \mathbf{E} = -\frac{\partial \mathbf{B}}{\partial t}. \tag{2.1}$$

4. **Ampère's Circuital Law:** Currents and displacement currents generate magnetic fields:
$$\nabla \times \mathbf{H} = \mathbf{j} + \frac{\partial \mathbf{D}}{\partial t}. \tag{2.2}$$

In linear materials the **D** and **B** fields are related to **E** and **H** by:

$$\mathbf{D} = \epsilon \cdot \mathbf{E}, \tag{2.3}$$
$$\mathbf{B} = \mu \cdot \mathbf{H}, \tag{2.4}$$

and **Ohm's Law** is valid:

$$\mathbf{j} = \sigma \cdot \mathbf{E}. \tag{2.5}$$

2.1.2 Telegraph equations

Taking the curl of Equation 2.1 provides two decoupled wave equations considering $\nabla \times (\nabla \times \mathbf{F}) = \nabla(\nabla \cdot \mathbf{F}) - \nabla^2\mathbf{F}$ and Maxwell's equations [*Ward and Hohmann*, 1988]. These wave equations are also called Telegraph equations:

$$\nabla^2\mathbf{E} - \mu\epsilon\frac{\partial^2\mathbf{E}}{\partial t^2} - \mu\sigma\frac{\partial\mathbf{E}}{\partial t} = 0, \tag{2.6}$$
$$\nabla^2\mathbf{H} - \mu\epsilon\frac{\partial^2\mathbf{H}}{\partial t^2} - \mu\sigma\frac{\partial\mathbf{H}}{\partial t} = 0. \tag{2.7}$$

In the simplest case, the 1D case, where the fields are changing in z direction (with z directed downwards into the surface of the earth), the Telegraph equations 2.6 and 2.7 simplify to:

$$\frac{\partial^2\mathbf{F}}{\partial z^2} - \mu\epsilon\frac{\partial^2\mathbf{F}}{\partial t^2} - \mu\sigma\frac{\partial\mathbf{F}}{\partial t} = 0 \qquad \text{with} \qquad \mathbf{F} \in \{\mathbf{E}, \mathbf{H}\}.$$

To solve the Telegraph equations, a sinusoidal wave is assumed:

$$\mathbf{F}(\omega) = \mathbf{F_0}e^{i\omega t} \qquad \text{with} \qquad \mathbf{F} \in \{\mathbf{E}, \mathbf{H}\} \quad , \quad \mathbf{F_0} \in \{\mathbf{E_0}, \mathbf{H_0}\}.$$

2.1.3 Helmholtz equations

In frequency domain the partial derivative of a sinusoidal wave with respect to time corresponds to the multiplication with $i\omega$ and the Telegraph equations simplify to:

$$\nabla^2\mathbf{F} + k^2\mathbf{F} = 0 \qquad \text{with} \qquad \mathbf{F} \in \{\mathbf{E}, \mathbf{H}\}. \tag{2.8}$$

The Equations 2.8 are called Helmholtz equations, where k^2 is the square of the angular wavenumber of the EM wave:

$$k^2 = \omega^2\mu\epsilon - i\omega\mu\sigma. \tag{2.9}$$

The first term of the right hand side of Equation 2.9 represents the displacement current, the second part the conduction current.

The Helmholtz equations simplify in the 1D case where the fields vary only in z direction to:

$$\frac{\partial^2 \mathbf{F}}{\partial z^2} + k^2 \mathbf{F} = 0 \qquad \text{with} \qquad \mathbf{F} \in \{\mathbf{E}, \mathbf{H}\}.$$

2.1.4 Diffusion equations

The conductivity of typical earth materials range from $10^{-4} - 100 \, \frac{\mathrm{S}}{\mathrm{m}}$. The dielectric constant of the earth materials range from $\epsilon_r = 3 - 40$ [*Davis and Annan*, 1989] and from $\epsilon_r = 4 - 8$ for most earth materials, *i.e.*, the electrical permittivity for most earth materials is $\epsilon = \epsilon_0 \epsilon_r \leq 7.1 \cdot 10^{-11} \, \frac{\mathrm{sS}}{\mathrm{m}}$. These estimations legimitate that at frequencies less than 10 kHz displacement currents are neglected against conduction currents:

$$\frac{\omega \, \mu \, \sigma}{\omega^2 \mu \, \epsilon} = \frac{\sigma}{\omega \, \epsilon} \geq \frac{10^{-4}}{2 \, \pi \cdot 10^4 \cdot 7.1 \cdot 10^{-11}} \approx 22, \tag{2.10}$$

Often, the conductivities are higher than $10^{-3} \, \frac{\mathrm{S}}{\mathrm{m}}$ and the neglect of displacement currents is also valid for higher frequencies.

For $\frac{\sigma}{\omega \, \epsilon} \gg 1$ the square of the angular wavenumber k in Equation 2.9 simplifies to $k^2 = -i\omega\mu\sigma$ and the Helmholtz equations in frequency domain can be written as:

$$\frac{\partial^2 \mathbf{F}}{\partial z^2} - i\omega\mu\sigma\mathbf{F} = 0 \qquad \text{with} \qquad \mathbf{F} \in \{\mathbf{E}, \mathbf{H}\}. \tag{2.11}$$

In time domain the Telegraph equations are used:

$$\frac{\partial^2 \mathbf{F}}{\partial z^2} - \mu\sigma\frac{\partial \mathbf{F}}{\partial t} = 0 \qquad \text{with} \qquad \mathbf{F} \in \{\mathbf{E}, \mathbf{H}\}. \tag{2.12}$$

Equations 2.11 and 2.12 describe the diffusion of the EM field in the ground and are called diffusion equations.

2.1.5 The electrical conductivity

The propagation of the EM field depends on three physical properties of the ground: the electrical conductivity σ, the magnetic permeability μ and the electrical permittivity ϵ. The electrical conductivity is the most important one and has three origins: the electronic conductivity of the rock, the electrolytic conductivity of the pore fluid, and in special cases the threshold conductivity between rock and pore fluid.

Archie's law

In sedimentary environments the electrical conductivity of the ground mainly depends on its clay content, porosity, mineral content, and water-saturation [*Archie*, 1942].

The porosity is defined as the ratio of the void space in a rock and its total volume:

$$\Phi = \frac{V_{void}}{V_{total}}.$$

The void space may contain air, gas, or pore fluid. The range of the porosity is between 0 and 1. Typical values are 0.01 for solid granite or 0.5 for peat or clay.

Archie's law relates the electrical conductivity, or more commonly, the resistivity ρ of fluid saturated clay-free sediments with the resistivity of the pore fluid ρ_f and the porosity Φ:

$$\rho = a \cdot \Phi^{-m} \rho_f. \tag{2.13}$$

The proportionality factor a (often fixed to 1) and the cementation exponent m have to be determined empirically. For unconsolidated rocks, such as sand, m has been observed near to 1.3 and increases with cementation. *Keller* [1988] proposes $a = 0.88$ and $m = 1.37$ for sediments with a porosity range of 25–45%.

If a part of the pore space is filled with air or gas, the isolating effect causes an increase of the resistivity and Archie's law can be written as [*Keller*, 1988]:

$$\rho = a \cdot \Phi^{-m} S^{-n} \rho_f. \tag{2.14}$$

Here, Φ is the volume fraction of pore space filled with air or gas and the saturation S is the fraction of pore space filled with fluid. At total saturation there holds $S = 1$. The saturation exponent n has values between 1 and 2 [*Jäger*, 1997] and is often fixed to 2.

The ion exchange capacity of clays or mineralized pore-fluid causes an interaction between the pore fluid and the rock [*Waxman and Smits*, 1968]. The resulting bilayer is characterized by the threshold conductivity σ_t for pore fluid [*Keller*, 1988] and Archie's law (Equation 2.14, valid for pure sands) can be expanded to [*Weidelt*, 1997]:

$$\rho = a \cdot \Phi^{-m} S^{-n} \rho_f + \rho_t. \tag{2.15}$$

One has to keep in mind that the clay must be wet for the conduction process to take place.

2.2 Continuous Vertical Electrical Soundings

Apparent resistivities are directly derived from DC currents injected into the ground using electrode pairs and electrical potentials measured between other pairs of electrodes. As the investigation depth generally increases as electrode separation increases, the vertical resistivity structure is obtained by varying the electrode separation. A detailed description of the resistivity method is given in, *e.g.*, *Telford et al.* [1990]. Multi-electrode or 2D resistivity surveying [*Griffiths and Turnbull*, 1985; *Dahlin*, 1996], also called continuous vertical electrical sounding (CVES), provides much higher productivity and better data quality than conventional 1D Schlumberger or Wenner surveys. Modern multi-electrode systems having automatically switching electrodes control the measurements using a predefined measurement

protocol [*Griffiths et al.*, 1990]. The survey's product is a high-resolution resistivity section down to a depth limited by the outer electrode distance and the current injected.

2.3 Time-domain Electromagnetics

Time-domain or transient EM (TEM) methods use a primary field that consists of a series of pulses separated by periods of switched-off primary fields. The primary field usually has the geometry of a vertical magnetic dipole or a horizontal electrical dipole, the latter is used, *e.g.*, for long-offset TEM [*Strack*, 1992]. The fast switch-off of a steady current flowing through a transmitter loop as primary field excitation causes a transient secondary signal as response. Figure 2.1 illustrates that the propagation of EM fields can be approximated by the equivalent current filament concept of *Nabighian and Macnae* [1991], which is also termed smoke-ring concept.

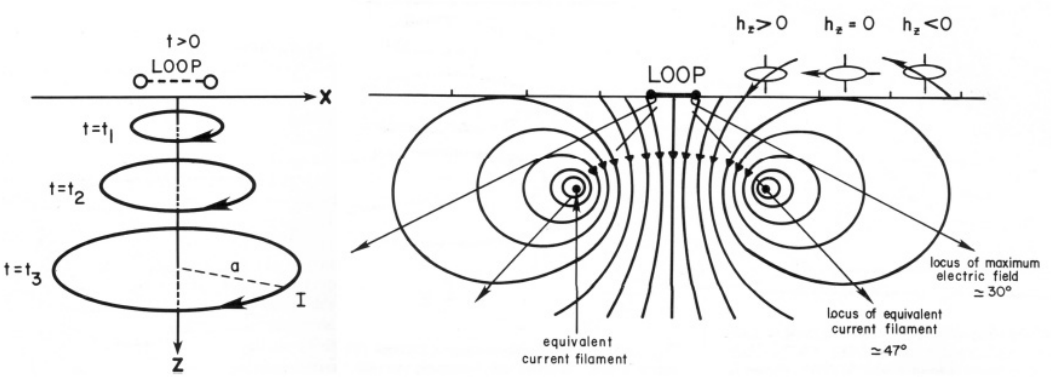

Figure 2.1: *The propagation of EM fields is illustrated by the smoke-ring concept: The induced current system migrates downward and outward with time [Nabighian and Macnae, 1991].*

The vertical field component H_z is the most important quantity of the secondary field and can be measured using an induction coil in absence of the primary field. The time-domain data are presented at discrete time gates after averaging repeated transmissions of a transient signal. A detailed discussion of the TEM method is presented by, *e.g.*, *Nabighian and Macnae* [1991].

2.3.1 Airborne TEM

Airborne TEM systems are traditionally used in mineral exploration. Worldwide several systems have been developed which differ in their geometries, dipole moments and data bandwidths. Helicopter-borne systems (*e.g.*, AeroTEM, HoisTEM, or VTEM) offer better spatial resolution and can be flown at lower altitude than fixed-wing systems such as GEOTEM or TEMPEST, but they are generally more expensive to operate [*Sattel*, 2006].

The first European helicopter-borne TEM system, the SkyTEM system [*Sørensen*

and Auken, 2004], has been developed at the University of Aarhus for large-scale groundwater investigations. This system is described in detail in Chapter 4.6.1.

2.3.2 Solving the diffusion equation in time domain

In Section 2.1.3 the diffusion equation in time domain was derived for 1D fields in a homogeneous medium (Equation 2.12):

$$\frac{\partial^2 \mathbf{F}}{\partial z^2} - \mu\sigma\frac{\partial \mathbf{F}}{\partial t} = 0 \qquad \text{with} \qquad \mathbf{F} \in \{\mathbf{E}, \mathbf{H}\}.$$

Nabighian and Macnae [1991] introduced the primary magnetic field as step function which should simulate the turn-off at $t = 0$:

$$H_0(t) = \begin{cases} H_0 & t < 0 \\ 0 & t > 0. \end{cases}$$

The transient fields at $t > 0$ and $z \geq 0$ are given by:

$$E_x(z,t) = \frac{2H_0}{\sigma\sqrt{\pi}} \cdot \theta \cdot e^{-\theta^2 z^2} \tag{2.16}$$

and

$$H_y(z,t) = H_0 \cdot \text{erfc}(\theta z),$$

with

$$\theta = \sqrt{\frac{\sigma\mu}{4t}},$$

the complementary error function

$$\text{erfc}(x) = 1 - \text{erf}(x),$$

and the error function

$$\text{erf}(x) = \frac{2}{\sqrt{\pi}} \int_0^x e^{-\xi^2} d\xi. \tag{2.17}$$

This notation is independent of the configuration and enables the derivation of the diffusion depth.

Diffusion depth

Setting the derivative of $E_x(z,t)$ with respect to time to zero, we find a depth for every time at that the local electrical field reaches its maximum. This depth is called diffusion depth d_{dif}:

$$d_{dif} = \sqrt{\frac{2t}{\sigma\mu}} \approx \sqrt{\frac{2t}{\sigma\mu_0}} \approx 1262 \cdot \sqrt{t[\,\text{s}\,] \cdot \rho[\,\Omega\text{m}\,]}. \tag{2.18}$$

This maximum moves downward with a velocity of:

$$v = \sqrt{\frac{2}{\sigma\mu t}}.$$

Solution for the central-loop configuration over a homogeneous half-space

In this thesis I consider TEM methods operated in central-loop configuration, where a horizontal receiver loop is located in the center of a horizontal transmitter loop (Figure 2.2) therefore in the following I will concentrate on this configuration.

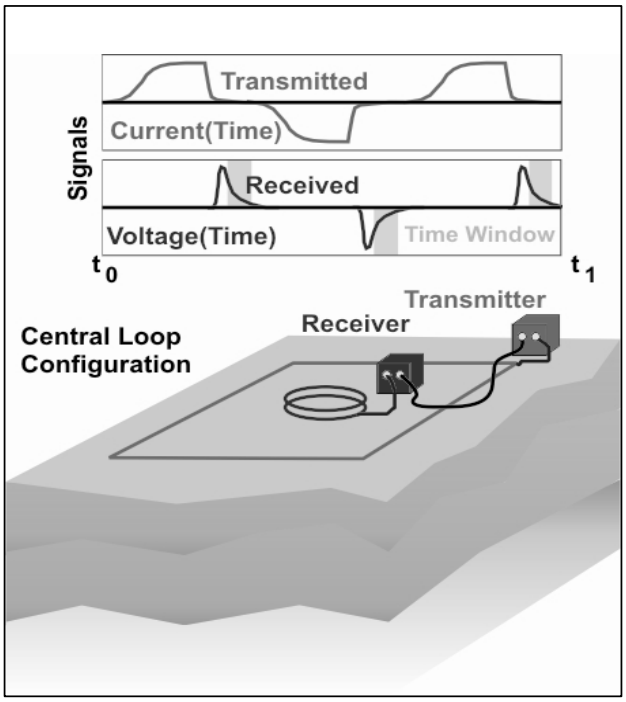

Figure 2.2: *TEM central-loop configuration and scheme of transmitted and received TEM waveforms.*

The equations for the quasi-static fields of various sources on the surface of a homogeneous half-space are published by, *e.g.*, *Spies and Frischknecht* [1991]. The general expressions for the vertical magnetic field H_z and its time derivative $\frac{\partial H_z}{\partial t}$ in the center of a horizontal transmitter loop with radius a and transmitter current I are:

$$H_z = \frac{It}{\sigma\mu_0 a^3} \cdot [(2(\theta a)^2 - 3) \cdot \text{erf}(\theta a) + \frac{6}{\sqrt{\pi}} \cdot \theta a \cdot e^{-(\theta a)^2}] \tag{2.19}$$

$$\frac{\partial H_z}{\partial t} = \frac{-I}{\sigma\mu_0 a^3} \cdot [3 \cdot \text{erf}(\theta a) - \frac{2}{\sqrt{\pi}} \cdot \theta a \cdot (3 + 2(\theta a)^2) \cdot e^{-(\theta a)^2}] \tag{2.20}$$

with the error function $\text{erf}(x)$ of Equation 2.17 and the induction number α:

$$\alpha = \theta a = \sqrt{\frac{\sigma\mu_0}{4t}} \cdot a$$

Before turning-off the primary field, H_z holds the direct current value ($t < 0$):

$$H_z^0 = \frac{I}{2a}$$

The general expressions of Equations 2.19 and 2.20 are valid over the complete range of induction numbers. They can be simplified to formulas of the "early-time asymptote" and the "late-time asymptote", valid for high induction numbers and small induction numbers, respectively.

Early-time asymptote With $t \to 0$ and $\theta a = \alpha \gg 1$ Equation 2.19 reduces to:

$$H_z^e = \frac{I}{2a}[1 - \frac{6t}{\sigma\mu_0 a^2}]$$

$$\Rightarrow \qquad \frac{\partial H_z^e}{\partial t} = \frac{-3I}{\sigma\mu_0 a^3}$$

$$\Rightarrow \qquad \rho_a^e = \frac{1}{\sigma} = \frac{-\mu_0 a^3}{3I}\frac{\partial H_z}{\partial t}$$

Late-time asymptote With $t \to \infty$ and $\theta a = \alpha \ll 1$ Equation 2.19 can be written as:

$$H_z^l = \frac{I\sigma^{3/2}\mu_0^{3/2}a^2}{30\pi^{1/2}t^{3/2}} \tag{2.21}$$

$$\Rightarrow \qquad \frac{\partial H_z^l}{\partial t} = \frac{-I\sigma^{3/2}\mu_0^{3/2}a^2}{20\pi^{1/2}t^{5/2}} \tag{2.22}$$

$$\Rightarrow \qquad \rho_a^l = \frac{I^{2/3}\mu_0 a^{4/3}}{20^{2/3}\pi^{1/3}t^{5/3}}\left(\frac{-\partial H_z}{\partial t}\right)^{-2/3} \tag{2.23}$$

The voltage U induced in the receiver loop covering the area A_R is proportional to the time derivative of the vertical magnetic field $\frac{\partial H_z}{\partial t}$:

$$U = -\mu_0 A_R \frac{\partial H_z}{\partial t} \tag{2.24}$$

From Equations 2.21 and 2.24 we get for the late-time apparent resistivity:

$$\Rightarrow \qquad \rho_a^l = \left(\frac{I \cdot A_T \cdot A_R}{U}\right)^{2/3} \cdot \left(\frac{1}{t}\right)^{5/3} \cdot \frac{\mu_0^{2/3}}{20^{2/3}\pi} \tag{2.25}$$

where A_T is the area of the transmitter loop and A_R is the area of the receiver loop.

The solution for the horizontally layered half-space is expressed in wavenumber domain [*Ward and Hohmann*, 1988]:

$$H_z = \frac{Ia}{2} \int_0^\infty e^{-\nu_1(z+h)} + R_{TE}\, e^{\nu_1(z-h)} \frac{\lambda^2}{\nu_1} J_1(\lambda a)\, d\lambda, \tag{2.26}$$

with $\nu_1 = \sqrt{\lambda^2 + i\omega\mu_0/\rho_1}$. λ is the wave number, R_{TE} is the reflection coefficient, and J_1 is the Bessel function of first kind and first order.

Depth of investigation

The definition of the depth of investigation d_{inv} is one attempt to appraise the theoretical capability of a method.

Spies [1989] terms the time when a buried inhomogeneity can be measured first, as time of departure t_d. It is derived from Equation 2.18 and defined as the time when the maximum of the EM field reaches a given depth, *e.g.*, the depth of the buried inhomogeneity:

$$t_d = \frac{\sigma_{av}\mu d^2}{2}. \tag{2.27}$$

The average conductivity σ_{av} of the overlying section is given by:

$$\sigma_{av}(z) = \frac{S(z)}{z} \quad \text{with} \quad S(z) = \int_0^\infty \sigma(z) dz, \tag{2.28}$$

where $S(z)$ is the cumulative conductance down to depth z.

The feasibility to receive an exploitable signal at time t_d depends on many factors, such as the signal strength of the primary field (the transmitter moment), the sensitivity of the instrumentation, and the noise level [*Spies*, 1989], *i.e.*, for detecting the buried inhomogeneity the response at the time of departure has to be higher than the noise level.

Spies [1989] approximates the depth of investigation for the central-loop configuration as:

$$d_{inv} = 0.48 \left(\frac{I}{\sigma\eta_v}\right)^{1/3} \quad \text{for} \quad a = 3\, d_{dif} \quad \text{far zone (early time),} \tag{2.29}$$

$$d_{inv} = 0.55 \left(\frac{I \cdot A_T}{\sigma\eta_v}\right)^{1/3} \quad \text{for} \quad a = 1.7\, d_{dif} \quad \text{intermediate zone,} \tag{2.30}$$

$$d_{inv} = 0.55 \left(\frac{I \cdot A_T}{\sigma\eta_v}\right)^{1/5} \quad \text{near zone (late time).} \tag{2.31}$$

Here, I is the transmitter current, A_T is the loop area of the transmitter coil, a is the radius of the transmitter coil, and η_v is the voltage noise level after stacking (typically 0.5 nV/m^2).

The exponent of $1/5$ in Equation 2.31 makes it difficult to increase the investigation depth in the near zone, *e.g.*, to double the investigation depth, a transmitting moment ($TM = I \cdot A_T$) of factor 32 is necessary.

2.4 Frequency-domain Electromagnetics

Frequency-domain EM can be subdivided in active and passive methods. Passive methods do not need their own transmitters, *e.g.*, magnetotellurics (MT) where the primary fields are natural EM variations of the external magnetic field, or radio magnetotellurics (RMT) which uses radio and very low frequency (VLF) transmitters. Active methods generate their own primary fields at discrete frequencies. As different frequencies have different diffusion depths, frequency-domain EM provides depth sounding.

2.4.1 Helicopter-borne EM

Helicopter-borne frequency-domain EM systems utilize several transmitter and receiver coils simultaneously. The transmitter signals, the primary magnetic fields, are generated by sinusoidal current flow through the transmitter coils at discrete frequencies. The oscillating primary magnetic fields induce eddy currents in the subsurface. These currents, which depend on the conductivity distribution of the subsurface, generate the secondary magnetic fields. The secondary magnetic fields measured by the receiver coils are divided by the primary magnetic fields expected at the center of the receiver coils and the ratio is measured in parts per million (ppm). As the secondary fields are very small with respect to the primary fields, the primary fields have to be "bucked". The orientation of the transmitter coils is horizontal or vertical; and the receiver coils are oriented in a maximally coupled position resulting in horizontal coplanar, vertical coplanar, or vertical coaxial coil systems. Typically, 4–6 frequencies are used on modern HEM systems. A scheme of HEM is outlined at Figure 4.6. For basics in detail see *Frischknecht et al.* [1991] and *Palacky and West* [1991] or more recently *Siemon* [2006*a*] .

2.4.2 Solving the diffusion equation in frequency-domain

In Section 2.1.3 the diffusion equation in frequency-domain was derived for 1D fields in a homogeneous medium (Equation 2.11):

$$\frac{\partial^2 \mathbf{F}}{\partial z^2} - i\omega\mu\sigma\mathbf{F} = 0 \qquad \text{with} \qquad \mathbf{F} \in \{\mathbf{E}, \mathbf{H}\}$$

The solution of the diffusion equation in frequency-domain depends on the geometry of the primary field.

Solution for a uniform field (plane wave) over a layered half-space

Over a layered half-space EM fields can be regarded as plane waves at a large distance from their transmitters (distance bigger than some wave lengths). Due to the high refractive index between the quasi-nonconducting air layer and the conductive ground, the incident primary wave is refracted strongly and enters into the ground nearly vertically. The solution of the diffusion equation can be calculated straightforwardly [*Wait*, 1953]. The MT and RMT methods benefit from the plane wave solution.

Solution for a magnetic dipole field over a layered half-space

The HEM method uses frequencies ranging from 300 Hz to 200 kHz. With the velocity of propagation of $c \approx 3 \cdot 10^8 \frac{\mathrm{m}}{\mathrm{s}}$ and $\lambda = \frac{c}{f}$ we get wave lengths of 100–1.5 km. As the sensor distance to the ground is about 30–100 m, the plane wave solution can not be utilized. The primary field is still an inhomogeneous magnetic dipole field and an integral in the wavenumber domain has to be solved (Equation 2.32).

The relative secondary field Z_k induced of a transmitting coil at the altitude h, in a receiver coil at the horizontal distance s, over a N-layered half-space with resistivities $\rho_n(n = 2, \dots N)$ and thicknesses $t_n(n = 2, \dots N-1)$ is derived by *Wait* [1962; 1982]:

$$Z_k = \frac{H}{H_0} = s^2 \int_0^\infty \lambda R_1 e^{-2h\lambda} f_k(\lambda s) d\lambda. \tag{2.32}$$

The function f_k $(k = 1, 2, 3)$ considers following coil configurations:

$k = 1:$ horizontal coplanar,

$k = 2:$ vertical coplanar,

$k = 3:$ vertical coaxial.

The corresponding functions f_k are given as:

$$f_1(\lambda s) = \lambda s \cdot J_0(\lambda s), \tag{2.33}$$
$$f_2(\lambda s) = J_1(\lambda s), \tag{2.34}$$
$$f_3(\lambda s) = [J_1(\lambda s) - \lambda s \cdot J_0(\lambda s)]/2. \tag{2.35}$$

J_0 and J_1 are the Bessel functions of first kind of zero and first order, respectively.

The (complex) reflection factor R_1 in Equation 2.32 depends on the vertical conductivity distribution and the system frequency. For a N-layered half-space R_1 can be calculated by the recurrence formula [*Wait*, 1962; *Frischknecht*, 1967]:

$$R_{n-1} = \frac{K_{n-1} + R_n \cdot e^{-2t_n\nu_n}}{1 + K_{n-1}R_n \cdot e^{-2t_n\nu_n}}, \quad n = N-1, \dots, 2, \tag{2.36}$$

$$K_{n-1} = \frac{\nu_{n-1} - \nu_n}{\nu_{n-1} + \nu_n} \quad \text{and} \quad \nu_n = \sqrt{\lambda^2 + i\omega\mu_0/\rho_n}. \tag{2.37}$$

At the layer boundary to the homogeneous half-space there holds $R_{N-1} = K_{N-1}$.

The air between the coil system and the ground is assumed to be the first layer with resistivity $\rho_1 = \infty$ and thickness $t_1 = h$.

Mundry's approximation The Bessel functions J_0 and J_1 can be expanded into series:

$$J_0(x) \approx 1 - \frac{x^2}{4} + \frac{x^4}{64} - \ldots, \tag{2.38}$$

$$J_1(x) \approx \frac{x}{2} - \frac{x^3}{16} + \frac{x^5}{384} - \ldots. \tag{2.39}$$

The transmitter and receiver coils of HEM systems are usually housed in one bird and the distance between the transmitting and the receiving coils is small compared to the altitude of the system above ground.

Substituting $\kappa = \lambda h$ the relative secondary field for a horizontal coplanar coil configuration ($k = 1$) is:

$$Z_{k=1} = \left(\frac{s}{h}\right)^3 \int_0^\infty \kappa^2 \bar{R}_1 e^{-2\kappa} J_0\left(\kappa \frac{s}{h}\right) d\kappa, \tag{2.40}$$

κ describing the normalized wavenumber.

For small ratios $\frac{s}{h}$ the Bessel function J_0 can be substituted by the first element of its series expansion (that is 1) and the secondary field can be simplified to:

$$Z = \left(\frac{s}{h}\right)^3 \int_0^\infty \kappa^2 \bar{R}_1 e^{-2\kappa} d\kappa = \left(\frac{s}{h}\right)^3 Z'. \tag{2.41}$$

The Mundry approximation (Equation 2.41) is valid for $h \geq 3.3s$ [*Mundry*, 1984].

The reflection factor $\bar{R}_1$ is obtained from R_1 (Equation 2.36) by substituting $\lambda = \frac{\kappa}{h}$.

The relative secondary field $Z = \Re(Z) + i\Im(Z) = R + iQ$ is a complex quantity and can be written as sum of its real component (in-phase) R and its imaginary component (out-of-phase, quadrature) Q. The amplitude A can be approximated by:

$$A = |Z| = \sqrt{R^2 + Q^2} \approx \left(\frac{s}{h}\right)^3 |Z'| = \left(\frac{s}{h}\right)^3 A'. \tag{2.42}$$

The first order approximation of the phase ratio ϵ is:

$$\epsilon = \frac{Q}{R} \approx \frac{\Im(Z')}{\Re(Z')}. \tag{2.43}$$

For a given layering the relative secondary field Z at sensor altitude h can be calculated by using these equations.

2.4.3 Solution of the Helmholtz equation in frequency-domain

For frequencies higher than 10 kHz, displacement currents can not be neglected in general and the exact calculation of the primary field requires the complex wavenumber (Section 2.1.3). *Yin and Hodges* [2005] derive the relative secondary field for a horizontal coplanar coil configuration, taking into account the displacement currents:

$$Z_{k=1} = s^3 \int_0^\infty R_1 \frac{\lambda^3}{\alpha_0} e^{-2h\alpha_0} J_0(\lambda s) d\lambda. \tag{2.44}$$

Here, α_0 is the wavenumber in the air half-space:

$$\alpha_0 = \sqrt{\lambda^2 - \omega^2 \epsilon_0 \mu_0 + i\omega\mu_0/\rho_1}. \tag{2.45}$$

The real part dominates the imaginary part and for frequencies less than 10 kHz the approximation $\alpha_0 \approx \lambda$ can be used.

Numerical calculation of the relative secondary field

There are different techniques for the numerical solution of the integral in Equation 2.44. The most common technique is the fast Hankel transform [*Johanson and Sørensen*, 1979; *Weidelt*, 1988]. Alternatively, for a high sensor altitude relative to the separation of transmitter and receiver coils, Equation 2.44 can be simplified in such way that the numerical Laplace transform can be used [*Fluche*, 1990]. The Laplace transform is calculated more than 10 times faster than the fast Hankel transform [*Sengpiel and Siemon*, 2000].

2.4.4 Half-space model

The secondary field measured generally depends on an unknown conductivity distribution. In order to get a first estimate, the interpretation starts based on the model of a homogeneous half-space. In airborne EM two parameters, the apparent resistivity $\rho_a(f)$ and the apparent distance $D_a(f)$ describe this model. For such an equivalent half-space the number of layers reduces to $n = 2$, the air-layer with $\rho_1 \to \infty$ and the half-space with $\rho_2 = \rho_a(f)$.

The reflection factor reduces to:

$$R_1 = K_1 = \frac{\nu_1 - \nu_2}{\nu_1 + \nu_2} = \frac{\lambda - \nu}{\lambda + \nu} \quad \text{with} \quad \nu = \nu_2 = \sqrt{\lambda^2 + \frac{2i}{p_a^2}}, \tag{2.46}$$

and the skin depth p_a

$$p_a = \sqrt{\frac{2\rho_a}{\omega\mu_0}}. \tag{2.47}$$

Using the Mundry approximation and substituting λ with the wavenumber multiplied by the apparent distance $\kappa = \lambda D_a$, the reflection factor is:

$$R_1 = \frac{\kappa - \bar{\nu}}{\kappa + \bar{\nu}} \quad \text{with} \quad \bar{\nu} = \sqrt{\kappa^2 + 2i\delta_a^2}, \tag{2.48}$$

and

$$\delta_a = \frac{D_a}{p_a}. \tag{2.49}$$

The relative secondary field is:

$$Z = \left(\frac{s}{D_a}\right)^3 \int_0^\infty \frac{\kappa - \bar{\nu}}{\kappa + \bar{\nu}} \kappa^2 e^{-2\kappa} d\kappa = \left(\frac{s}{h}\right)^3 Z'. \tag{2.50}$$

It is obvious that the value of the integral Z' just depends on δ_a. *Mundry* [1984] calculated $A'^{1/3}(\delta_a)$ and $\epsilon(\delta_a)$ curves and approximated these curves on a log-log scale by linear segments. *Siemon* [2001] obtains a more accurate solution by approximating $\delta_a(\epsilon)$ and $A'^{1/3}(\delta_a)$ by polynomials.

Knowing δ_a from $\epsilon = Q/R$, the amplitude $A'^{1/3}$ is obtained from the $A'^{1/3}(\delta_a)$ curve. For a given transmitter-receiver distance s the apparent distance D_a can be calculated from the ratio of A' and the measured amplitude A:

$$D_a = s \frac{A'}{A}^{1/3}. \tag{2.51}$$

The apparent resistivity ρ_a can be determined by transformation of Equation 2.47:

$$\rho_a = \frac{\omega \mu_0}{2} \left(\frac{D_a}{\delta_a}\right)^2. \tag{2.52}$$

In the case of a homogeneous ground, the apparent distance D_a equals the sensor height h for all frequencies and all calculated apparent resistivities ρ_a are identical to the resistivity of the homogeneous half-space.

For an inhomogeneous ground (*e.g.*, a layered half-space), D_a and ρ_a depend on the frequency. The difference between the calculated apparent distance and the measured sensor height is defined as apparent depth d_a [*Fraser*, 1978]:

$$d_a = D_a - h. \tag{2.53}$$

The apparent depth is a measure for the ratio of cover-layer and half-space resistivity. d_a is positive in case of a resistive cover and negative if the cover is more conductive than the half-space [*Siemon*, 2006*a*].

The different depth quantities are illustrated at Figure 2.3.

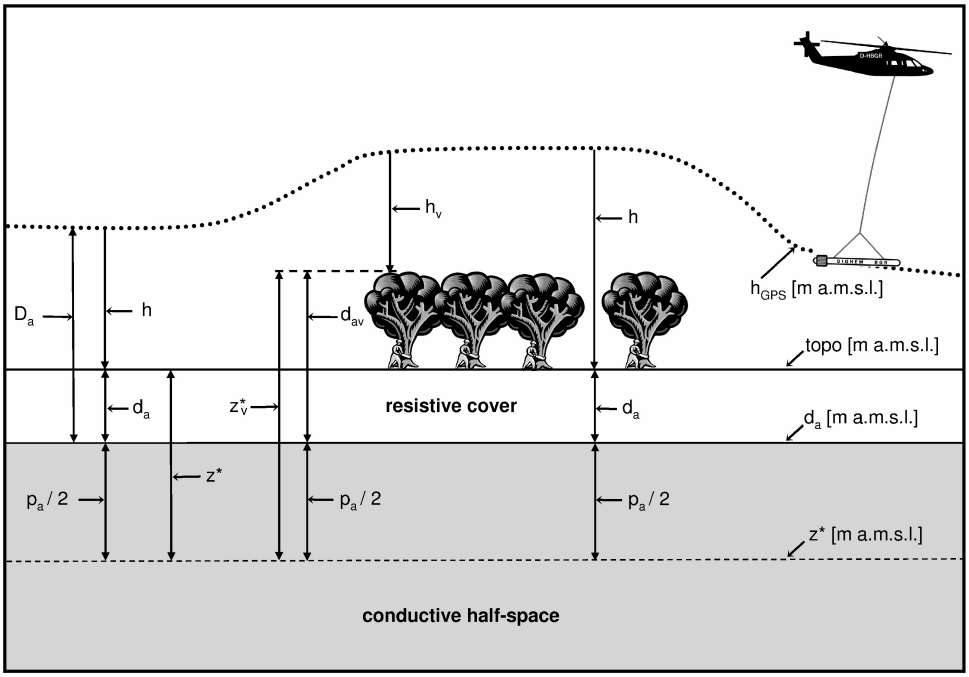

Figure 2.3: *Graphical display of apparent distance D_a, apparent depth d_a, centroid depth z^*, sensor altitude h, sensor elevation h_{GPS}, and topographic elevation $topo$. In case of buildings or trees, the sensor altitude h_v, and thus, the apparent depth d_{av} and the centroid depth z_v^* differ from their correct values, but their associated elevations in m a.m.s.l. (meter above mean sea level) are correct [Siemon, 2006a].*

Centroid depth

In analogy to the centroid depth for a uniform primary field defined by *Schmucker* [1970], *Sengpiel* [1988] introduced a centroid depth z^* for dipole induction. *Siemon* [2001] found that z^* can be calculated simply as:

$$z^* = d_a + \frac{p_a}{2}. \tag{2.54}$$

The centroid depth is a measure for the center of depth of the current system in a homogeneous half-space.

At each measurement site, the apparent resistivity and centroid depth pairs (ρ_a, z^*) are obtained individually for each frequency and then used for the automatic generation of the starting models which are required for 1D inversion.

Chapter 3

Inversion Techniques

In this chapter I will give a short introduction to inversion theory in order to briefly describe the different types of inversion used in this thesis. A detailed description of inversion theory is given by, *e.g.*, *Menke* [1984], *Meju* [1994], or *Tarantola* [2005].

A model will always be a simplification of reality. Based on observations we develop hypotheses for the causative processes and simplify them to mathematical formulations. Then we try to find a special (for our problem) solution of the mathematical formulation.

The modeling or the *forward problem* can be schematically described by:

model parameters $\mathbf{m}_{true} \longrightarrow$ model $g \longrightarrow$ model data $\mathbf{d}'$,

or mathematically: $\mathbf{d}' = g(\mathbf{m}_{true})$.

In many cases we are observing data and are looking for model parameters which explain the data. This procedure is opposite to the forward problem and referred to as *inverse theory*:

observe data $\mathbf{d} \longrightarrow$ model $g^{-1} \longrightarrow$ estimated model parameters $\mathbf{m}_{est}$,

or mathematically: $\mathbf{m}_{est} = g^{-1}(\mathbf{d})$.

Due to ambiguity caused by observation errors it is not possible to derive the model parameters $\mathbf{m}_{est}$ directly from the measured secondary field data $\mathbf{d}$. On the other hand it is possible to predict the model data $\mathbf{d}'$ for a given model $\mathbf{m}_{true}$. During the inversion process the model parameters $\mathbf{m}$ are varied until the model data $\mathbf{d}'$ and measured data $\mathbf{d}$ agree within a given threshold.

A perfect reconstruction of the observed data is normally not possible and the error vector $\mathbf{e} = \mathbf{d} - \mathbf{d}'$ represents the misfit between observed and calculated data. The aim of the inversion is to minimize the misfit, *i.e.*, to find a model that explains the measured data best.

3.1 Classification

One can differentiate between *discrete* inverse problems, where a finite amount of data is collected and the model parameters are expressed as a vector $\mathbf{m}$, and *continuous* inverse problems, where m and d are functions of time and space. In practice many continuous problems are discretized.

If the relation g between the model parameter vector $\mathbf{m}$ and the model data $\mathbf{d}'$ is *linear*, the inverse problem is described by the explicit linear equation:

$$\mathbf{d}' = \mathcal{G}\mathbf{m}, \tag{3.1}$$

with:

$$\begin{aligned} \mathbf{m} &= [m_1, m_2, ..., m_M]^T && \text{model parameters,} \\ \mathbf{d}'(m) = \mathbf{d}' &= [d'_1, d'_2, ..., d'_N]^T && \text{model data,} \\ \mathbf{d} &= [d_1, d_2, ..., d_N]^T && \text{observed data,} \\ \mathcal{G}_{N\times M} & && \text{forward operator, data kernel .} \end{aligned}$$

In the discrete inverse theory Equation 3.1 can be written as:

$$d'_i = \sum_{j=1}^{M} \mathcal{G}_{ij}\, m_j, \qquad i = 1, ..., N.$$

Inversion problems are further classified whether they provide enough information to specify uniquely the model parameters. A problem is termed *under-determined* if there are more unknowns than data ($M > N$) and several solutions exist. If the number of data is equal to the number of parameters ($N = M$) the problem is *even-determined* and exact one solution exists. An *over-determined* problem has more data than unknowns ($N > M$) and too much information for an exact solution. In practice most problems are *mixed-determined*, *i.e.*, some model parameters are over-determined and some are under-determined.

3.2 Least Square Method

Over-determined problems are generally solved using the least square method. Here, a parameter vector $\mathbf{m}$ is determined that minimizes the error vector $\mathbf{e}$ such that the object function, in this case the sum of squares of the error $E = \sum e_i^2$, is minimal. That means that the derivative of E with respect to $\mathbf{m}$ equals zero.

$$\begin{aligned} \frac{\partial E}{\partial \mathbf{m}} &= \frac{\partial}{\partial \mathbf{m}}(\mathbf{e}^T\mathbf{e}) = \frac{\partial}{\partial \mathbf{m}}(\mathbf{d} - \mathcal{G}\mathbf{m})^T(\mathbf{d} - \mathcal{G}\mathbf{m}) \\ &= \frac{\partial}{\partial \mathbf{m}}(\mathbf{d}^T\mathbf{d} - \mathbf{d}^T\mathcal{G}\mathbf{m} - \mathbf{m}^T\mathcal{G}^T\mathbf{d} + \mathbf{m}^T\mathcal{G}^T\mathcal{G}\mathbf{m}) \\ &= -\mathbf{d}^T\mathcal{G} - \mathcal{G}^T\mathbf{d} + \mathcal{G}^T\mathcal{G}\mathbf{m} + \mathbf{m}^T\mathcal{G}^T\mathcal{G} \\ &= -2\mathcal{G}^T\mathbf{d} + 2\mathcal{G}^T\mathcal{G}\mathbf{m} \\ &\stackrel{!}{=} 0 \end{aligned}$$

Presuming that $\mathcal{G}$ is full of rank, so that $\left(\mathcal{G}^T\mathcal{G}\right)^{-1}$ exists, the least square solution is:

$$\mathbf{m}_{est} = \left(\mathcal{G}^T\mathcal{G}\right)^{-1}\mathcal{G}^T\mathbf{d} = \mathcal{G}^\dagger\mathbf{d}. \tag{3.2}$$

The $N \times M$ matrix $\mathcal{G}^\dagger = \left(\mathcal{G}^T\mathcal{G}\right)^{-1}\mathcal{G}^T$ is called the *generalized inverse* of $\mathcal{G}$ or *Moore-Penrose Pseudo-inverse*.

Generally, a L_p-norm is used to minimize the error vector $\mathbf{e}$.

The L_p-norm is defined as:

$$\|\mathbf{e}\|_p = \left(\sum_{i=1}^{N} |e_i|^p\right)^{1/p}.$$

The ability of a L_p-norm for an inversion problem depends on the expected noise characteristics. The influence of outliers grows with increasing order p resulting in a worse reproduction of the general trend of the observed data. The L_1-norm is less sensitive to outliers and should be used for problems with long-tailed or exponential distributed noise. The L_2-norm (which is a modified version of the least square approach) is the best choice for problems with Gaussian or normal distributed noise.

3.2.1 Regularization of the least square solution

The under-determined part may lead to singularities in mixed-determined inverse problems. Stability can be obtained introducing an additional condition as long as the inverse problem is not too under-determined. The combination of prediction error and variability of the model parameters (the length of the solution vector) is minimized and the objective function is:

$$\Phi(\mathbf{m}) = E + \lambda L = \mathbf{e}^T\mathbf{e} + \lambda\mathbf{m}^T\mathbf{m}.$$

The *damping* or *Marquardt factor* λ, which determines the relative importance of E and L, has to be determined empirically. The larger the under-determined parts are, the higher λ has to be chosen. $\lambda = 0$ leads to the undamped least square solution. The vote of λ is a trade-off between the minimization of the prediction error and the under-determined part of the solution.

The solution is called *ridge regression* or *damped least square solution*:

$$\mathbf{m}_{est} = \left(\mathcal{G}^T\mathcal{G} + \lambda\mathcal{I}\right)^{-1}\mathcal{G}^T\mathbf{d}. \tag{3.3}$$

3.3 Newton's Method

The resistivity–depth sounding problem is highly non-linear in frequency-domain as well as in time-domain EM: $\mathbf{d}' = \mathbf{F}(\mathbf{m})$. For non-linear inversion problems no special inversion theories exist.

3.3.1 Linearization by Taylor series

Assuming the model function $\mathbf{F}$ is continuously differentiable, such problems are handled by linearization of $\mathbf{F}$ using Taylor's theorem. The Taylor series of a starting model $\mathbf{m_0}$:

$$d_i' = F_i(m_{0_1}, ..., m_{0_M}) + \sum_{j=1}^{M} \frac{\partial}{\partial m_j} F_i(m_{0_1}, ..., m_{0_M})(m_j - m_{0_j}) \qquad i = 1, ..., N \quad (3.4)$$

is truncated after the first order, and only the linear term (*i.e.*, $M = 1$) is used. In matrix formulation:

$$\begin{aligned} & \mathbf{d}' = \mathbf{d_0'} + \nabla\mathbf{F}(\mathbf{m_0})\,(\mathbf{m} - \mathbf{m_0}) \\ \Leftrightarrow \qquad & \delta\mathbf{d} = \mathcal{G}\,\delta\mathbf{m}. \end{aligned} \quad (3.5)$$

Equation 3.5 has the form of Equation 3.1, with:

$$\begin{aligned} \delta\mathbf{d} &= \mathbf{d}' - \mathbf{d_0'} && \text{data difference vector,} \\ \delta\mathbf{m} &= \mathbf{m} - \mathbf{m_0} && \text{model difference vector,} \\ \mathcal{G}_{N\times M} = \nabla\mathbf{F}(\mathbf{m_0}) &= \begin{pmatrix} \frac{\partial F_1(\mathbf{m}_0)}{\partial m_1} & \cdots & \frac{\partial F_1(\mathbf{m}_0)}{\partial m_M} \\ \vdots & \ddots & \vdots \\ \frac{\partial F_N(\mathbf{m}_0)}{\partial m_1} & \cdots & \frac{\partial F_N(\mathbf{m}_0)}{\partial m_M} \end{pmatrix} && \text{Jacobian matrix.} \end{aligned}$$

The *Jacobian matrix* $\mathcal{G}$ is also called *sensitivity matrix*.

3.3.2 Newton's method

Having a starting model $\mathbf{m}_0$ sufficiently close to the true model $\mathbf{m}_{true}$ and using the model update

$$\mathbf{m}^{i+1} = \mathbf{m}^i + \left(\nabla\mathbf{F}(\mathbf{m}^i)\right)^{-1}\left(\mathbf{d} - \mathbf{F}(\mathbf{m}^i)\right),$$

$\mathbf{m}^{i+1}$ will converge to $\mathbf{m}_{true}$.

To overcome convergence problems Newton's method can be modified, *e.g.*, by inserting a damping factor α. Here, along the line $\mathbf{m} + \delta\mathbf{m}$ the point is searched that minimizes $\left\|\mathbf{F}(\mathbf{m}^i + \alpha\delta\mathbf{m}) - \mathbf{d}\right\|_2$. This step is taken for the model update.

Generally, non-linear inversion problems do not have a unique solution that minimizes the objective function and Newton's iterative method will converge to the minimum next to the starting model $\mathbf{m}_0$, which may be a local, but not the global minimum (Figure 3.1). Therefore, the choice of a reasonable starting model is important, it can often be limited by *a priori* information.

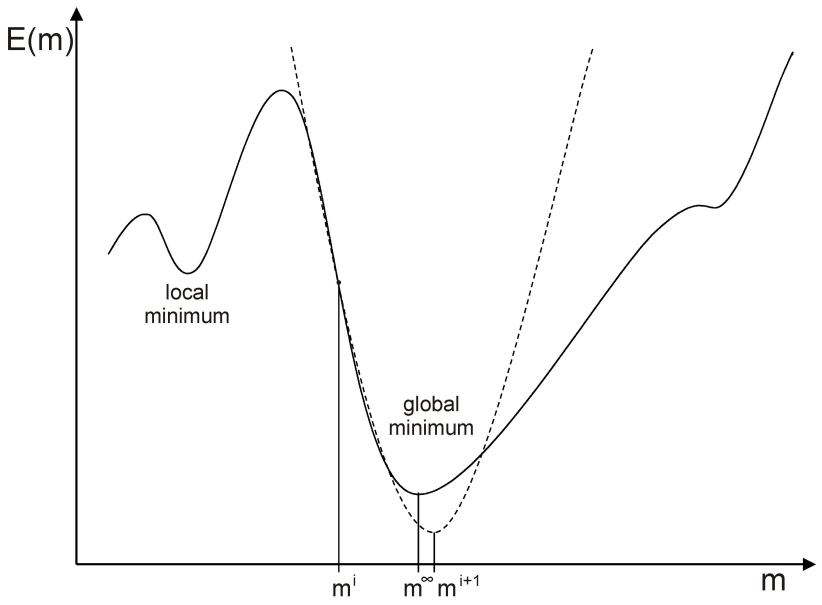

Figure 3.1: *Model update of the Newton method: The solid line shows the error function of the model vector $E(m)$. The Newton method locates the next model update m^{i+1} at the minimum of the paraboloid (dashed line) that is tangent to E at the recent model vector m^i (modified after Menke [1984]).*

3.4 Singular Value Decomposition

The singular value decomposition (SVD) is one method to analyze least square problems. The data kernel $\mathcal{G}_{N\times M}$ is factorized into:

$$\mathcal{G} = \mathcal{U}\Lambda\mathcal{V}^T,$$

where

$\mathcal{U}_{N\times N}$ is an orthogonal matrix, the columns are basis vectors of the data space,
$\mathcal{V}_{M\times M}$ is an orthogonal matrix, the columns are basis vectors of the model space,
$\Lambda_{N\times M}$ is a diagonal matrix with singular values s_i along the diagonal arranged, in decreasing size: $s_1 \geq s_2 \geq \cdots \geq s_p \geq 0, \quad p = \text{rank}(\mathcal{G})$.

Following relations are true:

$$\mathcal{U}^T = \mathcal{U}^{-1} \quad \Leftrightarrow \quad \mathcal{U}\mathcal{U}^T = \mathcal{I}_{N\times N} \qquad \mathcal{U}^T\mathcal{U} = \mathcal{I}_{M\times M}, \tag{3.6}$$

$$\mathcal{V}^T = \mathcal{V}^{-1} \quad \Leftrightarrow \quad \mathcal{V}\mathcal{V}^T = \mathcal{V}^T\mathcal{V} = \mathcal{I}_{M\times M}, \tag{3.7}$$

$$\mathcal{G} = \mathcal{U}\Lambda\mathcal{V}^T \quad \Leftrightarrow \quad \mathcal{G}^T = \mathcal{V}\Lambda\mathcal{U}^T. \tag{3.8}$$

$\mathcal{I}_{N\times N}$, $\mathcal{I}_{M\times M}$ are identity matrices.

Combining the least square solution in Equation 3.2 with the Equations 3.6–3.8 results in:

$$\begin{aligned}\mathbf{m} &= (\mathcal{G}^T\mathcal{G})^{-1}\mathcal{G}^T\mathbf{d} \\ &\overset{3.8}{=} (\mathcal{V}\Lambda\mathcal{U}^T\mathcal{U}\Lambda\mathcal{V}^T)^{-1}\mathcal{V}\Lambda\mathcal{U}^T\mathbf{d} \\ &\overset{3.6}{=} (\mathcal{V}\Lambda\Lambda\mathcal{V}^T)^{-1}\mathcal{V}\Lambda\mathcal{U}^T\mathbf{d} \\ &= (\mathcal{V}^T)^{-1}\Lambda^{-1}\Lambda^{-1}\mathcal{V}^{-1}\mathcal{V}\Lambda\mathcal{U}^T\mathbf{d} \\ &\overset{3.7}{=} \mathcal{V}\Lambda^{-1}\Lambda^{-1}\mathcal{V}^T\mathcal{V}\Lambda\mathcal{U}^T\mathbf{d} \\ &= \mathcal{V}\Lambda^{-1}\mathcal{U}^T\mathbf{d}.\end{aligned}$$

The model estimate with SVD is:

$$\mathbf{m}_{est} = \mathcal{V}\Lambda^{-1}\mathcal{U}^T\mathbf{d} \qquad \text{with} \qquad s_i^{-1} = \begin{cases}\frac{1}{s_i} & s_i > 0 \\ 0 & s_i = 0\end{cases}$$

$$= \mathcal{G}^\dagger\mathbf{d} = \sum_{i=1}^{p}\frac{\mathbf{u}_i\mathbf{d}}{s_i}\mathbf{v}_i.$$

The weakness of this formulation is that the division by s_i may cause singularities, *i.e.*, very small eigenvalues s_i result in very large coefficients which may dominate the solution.

3.4.1 Marquardt-Levenberg method

As described in Section 3.2.1 the problem of singularities can be stabilized by regularization (Tikhonov regularization, ridge regression, or Marquardt-Levenberg method).

After Equation 3.3, the damped least square solution is:

$$\begin{aligned}\mathbf{m} &= (\mathcal{G}^T\mathcal{G} + \lambda\mathcal{I})^{-1}\mathcal{G}^T\mathbf{d} \\ &= \mathcal{G}^\dagger\mathbf{d} \qquad \text{with} \quad \mathcal{G}^\dagger_{N\times M} = (\mathcal{G}^T\mathcal{G} + \lambda\mathcal{I})^{-1}\mathcal{G}^T,\end{aligned}$$

where the Marquardt parameter λ is used to controll the direction and size of the inversion step [*Marquardt*, 1963].

In the formulation of SVD, regularization is achieved by replacing the $\frac{1}{s_i}$ in the Λ^{-1} matrix by

$$\frac{s_i}{s_i^2 + \lambda}$$

[*Jupp and Vozoff*, 1975; *Meju*, 1994] and the model estimate results in:

$$\mathbf{m} = \mathcal{V}\Lambda^{-1}\mathcal{U}^T\mathbf{d} \qquad \text{with} \qquad s_i^{-1} = \begin{cases}\frac{s_i}{s_i^2+\lambda} & s_i > 0 \\ 0 & s_i = 0.\end{cases} \tag{3.9}$$

For $s_i \gg \lambda$ we get the undamped least square solution; for s_i close to zero a positive λ avoids singularity problems. The Marquardt parameter damps the influence of the small singular values which are related to less resolved parameters.

Usually the entries of Λ^{-1} are normalized on the highest value s_1:

$$\mathcal{K} = \begin{pmatrix} \frac{1}{s_1+\frac{\nu^2}{s_1}} & & \\ & \ddots & \\ & & \frac{\frac{s_n}{s_1}}{\frac{s_n^2}{s_1}+\frac{\lambda}{s_1}} \end{pmatrix}.$$

3.5 Evaluation of Inversion Results

3.5.1 Data misfit

One measure for the quality of an inversion result is the data fit, which is derived from the misfit e_i of the observed data d_i and the model data d_i'. The misfit is quantified as root-mean-square deviation (RMS-error), where each datum is weighted by its variance σ_i^2:

$$RMS(\mathbf{e}) = \sqrt{\frac{1}{N}\sum_{i=1}^{N}\frac{1}{\sigma_i^2}(d_i - d_i')^2}. \tag{3.10}$$

In the ideal case the real residual $e_i = d_i - d_i'$ is consistent with the expected deviation σ_i and the data fit is $RMS(\mathbf{e}) = 1$. However, in reality the ground does not conform to a 1D layering, the data are influenced by multidimensional structures and the data fit is $RMS(\mathbf{e}) \geq 1$.

Especially for complex models with many free parameters, good data is no guaranty for a realistic modeling of the observed data. The objective function can have several local minima, therefore the inversion result and the data fit depend on the chosen starting model.

3.5.2 Model uncertainty

If the data fit is considered to be satisfactory, we are interested in the uncertainties of the estimated model parameters. We are looking for the standard deviation $\sigma_{\mathbf{m}} = \Delta\mathbf{m}$ of the model parameters.

Assuming that the data are uncorrelated and the variance $\sigma_{\mathbf{d}}^2$ is statistically the same for all data, the error propagation of the data to the model can be expressed by the *model covariance matrix* $\mathcal{C}_{\mathbf{m}}$:

$$\mathcal{C}_{\mathbf{m}} = \sigma_{\mathbf{d}}^2 \left(\mathcal{G}^T\mathcal{G}\right)^{-1}. \tag{3.11}$$

The diagonal elements of the covariance matrix are the variances $\sigma_{\mathbf{m}}^2$ and the square roots can be interpreted as uncertainties on the model parameters.

3.5.3 Model equivalence

Due to the fact that the measured data are contaminated with errors, the model parameters are not independent of each other and following types of equivalences have to be considered:

- If a conducting layer m lies between two resistive layers, only the product of thickness h_m and resistivity ρ_m can be determined, but not the stand-alone parameters. This type is called *S equivalence* or *minimum type*:

$$\sqrt{\frac{h_m}{\rho_m}} = \text{ const.}$$

- A resistive layer m between two conductive layers is called *T equivalence* or *maximum type*:

$$h_m^2 \cdot \rho_m = \text{ const.}$$

The existence of model equivalences is a problem of single site inversions. *A priori* information can help to limit the models to be considered as starting model.

3.5.4 Model resolution matrix

The model resolution matrix $\mathcal{R}$ is a measure of how independent the model parameters can be predicted, or resolved:

$$\mathbf{m}_{est} = \mathcal{R}\mathbf{m}_{true}$$

and is for the unconstrained least square solution:

$$\mathbf{m}_{est} = \left(\mathcal{G}^T\mathcal{G}\right)^{-1}\mathcal{G}^T\mathbf{d} = \left(\mathcal{G}^T\mathcal{G}\right)^{-1}\mathcal{G}^T\left(\mathcal{G}\mathbf{m}_{true}\right)$$

$$\Rightarrow \mathcal{R} = \left(\mathcal{G}^T\mathcal{G}\right)^{-1}\mathcal{G}^T\mathcal{G} = \mathcal{I}. \tag{3.12}$$

In terms of SVD:

$$\mathcal{R} = \left(\mathcal{V}\Lambda^{-1}\mathcal{U}^T\right)\left(\mathcal{U}\Lambda\mathcal{V}^T\right) = \mathcal{V}\mathcal{V}^T.$$

In the ideal case each model parameter is uniquely determined and $\mathcal{R}$ is an identity matrix. The resolution is perfect. Otherwise, the estimated model parameters are weighted averages of the true model parameters and $\mathcal{R}$ describes, how the true model smears out into the estimated model. The model resolution is independent of the data and only a function of the data kernel.

Meju [1994] remarks that the model resolution matrix is always an identity matrix for the least square inversion without and with *a priori* information. The damped least square solution does not have a perfect solution due to the adding of a constant bias to the eigenvalues. He warns not to overstate the resolution matrix in the evaluation of the inversion results, because a perfect resolution does not automatically represent a reliable model.

3.6 Laterally Constrained Inversion

In sedimentary environments lateral smooth models can be expected. They can be achieved by smoothing the raw data before inversion, which is often done for airborne EM data having a high lateral data density. That is termed smoothing in the data space. An other approach is the laterally constrained inversion (LCI), where constraints are applied between adjacent model parameters during the inversion. The LCI is an example of smoothing in the model space. It is a profile-oriented technique which favors structures following the line direction; neighboring lines are not considered.

The LCI scheme described in this section was developed by the Hydrogeophysics Group of the Aarhus University, Denmark, and is referred to *Auken and Christiansen* [2004] and *Auken et al.* [2005]. This kind of inversion makes sense for continuous 1D data sets from environments where the geology can be represented with quasi-layered models, like sedimentary environments. All 1D data sets of, *e.g.*, continuous resistivity data are inverted in one system. Lateral constraints regularize the inversion by connecting neighboring models (Figure 3.2). Here, two adjacent model parameters are restricted to vary within a specified variance. The result is a layered section with lateral smooth transitions.

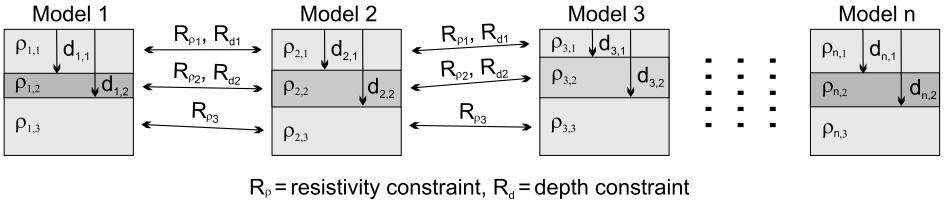

Figure 3.2: *Scheme of the laterally constrained inversion: Neighbored model parameters are connected by constraints. (Figure taken from Auken et al. [2005].)*

Auken and Christiansen [2004] describe the dependence of the observed data $\mathbf{d}_{obs}$ on the model parameters $\mathbf{m}_{true}$ as a non-linear differential forward mapping and linearize the model function using the first term of the Taylor expansion:

$$\delta\mathbf{d}_{obs} + \mathbf{e}_{obs} = \mathcal{G}\,\delta\mathbf{m}_{true}, \tag{3.13}$$

with the Jacobian matrix $\mathcal{G}$. Equation 3.13 has the form of Equation 3.5 and additionally considers the error of the observed data $\mathbf{e}_{obs}$. The covariance matrix for the observed errors is $\mathcal{C}_{obs}$. If we assume that the errors are uncorrelated, then $\mathcal{C}_{obs}$ is a diagonal matrix.

3.6.1 *A priori* information

Auken and Christiansen [2004] follow *Jackson* [1979] and include *a priori* information as additional data set $\mathbf{m}_{prior}$ in the inversion scheme:

$$\delta\mathbf{m}_{prior} + \mathbf{e}_{prior} = \mathcal{I}\,\delta\mathbf{m}_{true}. \tag{3.14}$$

Here, $\mathbf{e}_{prior}$ is the error on the *a priori* model with zero as the expected value and $\mathcal{I}$ is the identity matrix with the dimension of the model vector. The covariance for the *a priori* model is $\mathcal{C}_{prior}$.

3.6.2 Lateral constraints

In an analogous manner *Auken and Christiansen* [2004] connect constraints to the model:

$$\delta\mathbf{r} + \mathbf{e}_r = \mathcal{R}\,\delta\mathbf{m}_{true}. \tag{3.15}$$

Here, $\mathbf{e}_r$ is the error on the constraints with zero as the expected value and $\delta\mathbf{r} = -\mathcal{R}\,\delta\mathbf{m}_0$ provides the identity between the parameters tied by constraints in the roughening matrix, containing 1 and -1 for the constrained parameters, 0 in all other places. The constraints contain information about the geological variability of the model parameters. The variance, or strength of the constraints, is described by the covariance matrix $\mathcal{C}_R$.

3.6.3 Inversion

Combining the Equations 3.13, 3.14 and 3.15 the inversion problem results in:

$$\begin{bmatrix} \delta\mathbf{d}_{obs} \\ \delta\mathbf{m}_{prior} \\ \delta\mathbf{r} \end{bmatrix} + \begin{bmatrix} \mathbf{e}_{obs} \\ \mathbf{e}_{prior} \\ \mathbf{e}_r \end{bmatrix} = \begin{bmatrix} \mathcal{G} \\ \mathcal{I} \\ \mathcal{R} \end{bmatrix} \delta\mathbf{m}_{true}$$
$$\Rightarrow\ \delta\mathbf{d}' + \mathbf{e}' = \mathcal{G}'\,\delta\mathbf{m}_{true}. \tag{3.16}$$

The model estimate

$$\delta\mathbf{m}_{est} = \left(\mathcal{G}'^T\mathcal{C}'^{-1}\mathcal{G}'\right)^{-1}\mathcal{G}'^T C'^{-1}\delta\mathbf{d}' \tag{3.17}$$

minimizes

$$E = \left(\frac{1}{N+M+A}\left(\delta\mathbf{d}'^T\mathcal{C}'^{-1}\delta\mathbf{d}'\right)\right)^{\frac{1}{2}}, \tag{3.18}$$

where N is the number of data, M is the number of model parameters and A is the number of constraints. $\mathcal{C}'$ is the covariance matrix for the joint observation error $\mathbf{e}'$:

$$\mathcal{C}' = \begin{bmatrix} \mathcal{C}_{obs} & & 0 \\ & \mathcal{C}_{prior} & \\ 0 & & \mathcal{C}_R \end{bmatrix}. \tag{3.19}$$

When the data are uncorrelated and only diagonal covariances are used, the misfit criterion simplifies to

$$E = \left(\frac{1}{N+M+A}\sum_{i=1}^{N+M+A}\frac{\delta d_i'^2}{\mathrm{var}(e_i')}\right)^{\frac{1}{2}}. \tag{3.20}$$

Regularization

In order to stabilize the convergence of the inversion process the Marquardt formulation via a Marquardt damping factor λ is used [*Auken and Christiansen*, 2004]. The model update at the n-th iteration in an iterative inversion scheme is:

$$\mathbf{m}_{n+1} = \mathbf{m}_n + \left(\left(\mathcal{G}_n'^T \mathcal{C}'^{-1} \mathcal{G}_n' + \lambda_n \mathcal{I} \right)^{-1} \mathcal{G}_n'^T C'^{-1} \delta \mathbf{d}_n' \right). \tag{3.21}$$

Additionally, *Auken and Christiansen* [2004] use an adaptive damping on the step size for the model update based on the success of the previous iteration.

3.6.4 Sensitivity analysis

The linearized approximation of the covariance matrix of the model estimates, $\mathcal{C}_{est}$, is given by:

$$\mathcal{C}_{est} = \left(\mathcal{G}'^T \mathcal{C}'^{-1} \mathcal{G}' \right)^{-1}. \tag{3.22}$$

Standard deviations on model parameters are calculated as the square root of the diagonal elements in $\mathcal{C}_{est}$. Because the model parameters are represented as logarithms, the analysis gives a standard deviation factor ($STDF$) for the parameter m_s as:

$$STDF(m_s) = \exp \sqrt{C_{est,ss}}. \tag{3.23}$$

In the theoretical case of perfect resolution $STDF = 1$. A factor of $STDF = 1.1$ is approximately equivalent to an error of 10%. Roughly speaking, for well-resolved parameters $STDF \leq 1.2$, for moderately resolved parameters $1.2 < STDF \leq 1.5$, for poorly resolved parameters $1.5 < STDF \leq 2$, and for unresolved parameters $STDF > 2$.

3.6.5 Spatially constrained inversion

Viezzoli et al. [2008] expand the concept of the LCI to the spatially constrained inversion (SCI) which includes both models along and across profiles and applied it on airborne TEM data. The mathematical formulation of the SCI is identical to the LCI formulation (see Section 3.6) and differs mainly in the covariance matrix $\mathcal{C}_R$ which describes the strength of the constraints between the soundings as distance dependent:

$$C_{SCI}(d) = 1 + (c_{ref} - 1) \left(\frac{d}{d_{ref}} \right)^a, \tag{3.24}$$

where d is the distance between the soundings. The reference distance d_{ref}, the reference constraints c_{ref}, and the exponent a have to be obtained empirically.

Details of the practical application of SCI are described in Chapter 5.

Chapter 4

Field Example: The Buried Cuxhaven Valley

4.1 Introduction

Buried valleys in northern Europe were formed by subglacial melt-water erosion during quaternary glaciations and subsequently refilled with gravel, sand, silt, and clay. Today they are often covered by Holocene sediments and thus not always visible in the surface morphology. Figure 4.1 illustrates the geological situation in a schematic cross section. The genesis of buried valleys, or tunnel valleys, is discussed in detail by, *e.g.*, *Cofaigh* [1996], *Dijke and Veldkamp* [1996], *Piotrowski* [1997], *Huuse and Lykke-Andersen* [2000], and *Jørgensen and Sandersen* [2006].

Buried valleys are potential groundwater reservoirs and important for the future supply of drinking water, because they are often filled with highly permeable and porous sediments. The internal structure of buried valleys is non-uniform [*Piotrowski*, 1994]. As a result, hydraulic connections to adjacent groundwater reservoirs and pathways for contaminants from the surface to deeper reservoirs can vary along their course. The natural protection of aquifers in buried valleys against pollution varies depending on the thicknesses of covering clay layers. In the North Sea region, groundwater reservoirs within buried valleys are also vulnerable to saltwater intrusion. This will be of increasing concern over the coming centuries if the sea level might rise.

Within the interregional Buried Valleys (BurVal) project, co-funded by the European Union, glacial valleys in northern Europe have been investigated using various geophysical and hydrogeological methods [*Kirsch et al.*, 2006]. The aim of the BurVal project has been to deliver substantiated knowledge and understanding of the structural and hydraulic properties, to focus on the vulnerability to surface contamination and other human impacts, and to investigate interactions with saltwater intrusions and other groundwater reservoirs. Geophysical methods can contribute to map the course, lateral extent, and internal structure of buried valleys and to determine the hydrogeological properties of the sedimentary infill. The most important condition for a successful application of geophysical methods is a sufficient

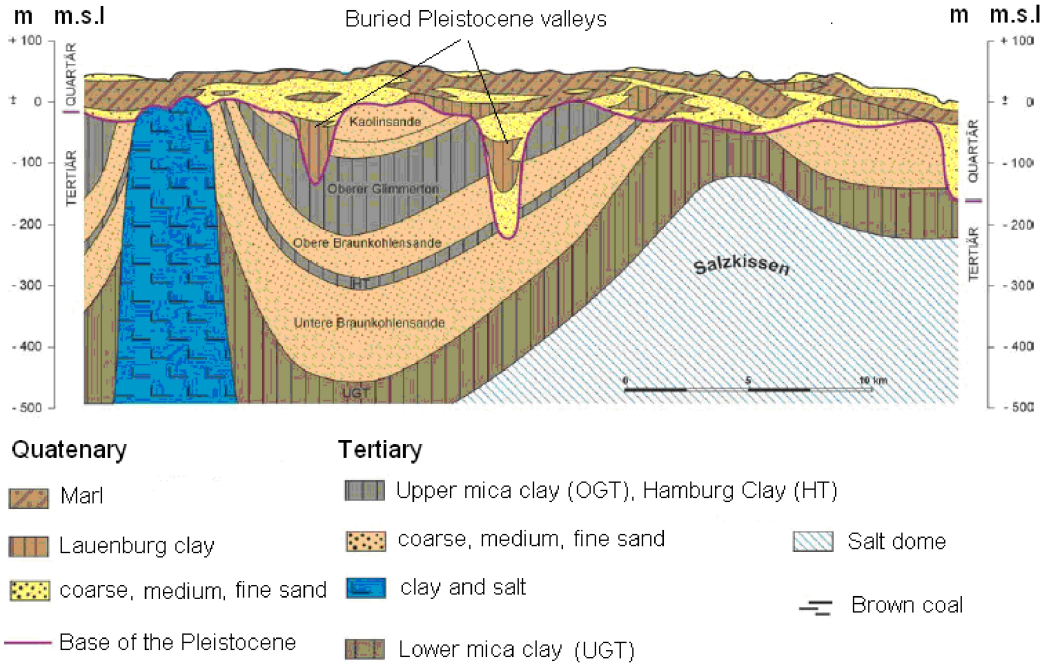

Figure 4.1: *Schematic cross section of a characteristic geological situation in northern Germany: Buried pleistocene valleys cut into Tertiary sediments and ascending salt structures. Aquifers are shown as yellow and light brown dotted sandy layers; aquitards as brown and grey clay layers. The red line marks the boundary between Quaternary and Tertiary sediments (modified after Wiederhold et al. [2002]).*

contrast in the physical parameter under investigation, *e.g.*, electrical conductivity, seismic velocity, or density.

Several papers discuss the importance of geophysical methods for groundwater exploration, especially for the investigation of buried valleys. Resistivity mapping is one of the classical geophysical methods used for groundwater surveys. *Flathe* [1955] investigated the "Possibilities and limitations in applying geoelectrical methods to hydrogeological problems in the coastal areas of North West Germany". Within the BurVal project, pulled array continuous electrical soundings (PACES) [*Sørensen*, 1996] were successfully used at several buried valleys in Denmark, *e.g.*, *Kjærstrup and Erfurt* [2006] and *Jørgensen et al.* [2006]. *Gabriel et al.* [2003] and *Wiederhold et al.* [2005] summarized the results of different geophysical methods applied to buried valleys in northern Germany – including reflection seismic, gravimetric, direct current (DC) resistivity, and helicopter-borne electromagnetic (HEM) methods. *Jørgensen et al.* [2003] presented an integrated application of time-domain electromagnetics (TEM), reflection seismics and exploratory drilling for the investigation of buried valleys in Denmark. *Auken et al.* [2003] described the investigation of buried valleys using TEM and *Danielsen et al.* [2003] presented a 2D model study which shows the limitation of TEM 1D inversion in the determination of the slopes of valleys. The conclusion of all these studies is that a combination of different methods is essential for a detailed understanding of buried valleys. HEM and TEM were successfully combined for hydrogeological investigations, *e.g.*, by *Fitterman and Deszcz-Pan* [2001] for saltwater mapping in the Everglades National Park in Florida, USA, and by *Stadtler et al.* [2004] for groundwater studies in Namibia.

Eberle and Siemon [2006] showed that buried valleys were successfully delineated using HEM at four case studies in Germany and in Namibia. One of them, the Cuxhaven area in northern Germany, was described in detail by *Siemon et al.* [2004]. SkyTEM was also successfully applied in groundwater surveys and at buried valleys by, *e.g.*, *Jørgensen et al.* [2006], *Kjærstrup and Erfurt* [2006], and *Scheer et al.* [2006].

In this chapter I focus on the results of HEM and SkyTEM applied at the Cuxhaven valley, one of the six pilot project areas of the BurVal project [*Rumpel et al.*, 2006]. The airborne results will be compared in detail with established ground-based geophysical methods, such as the continuous vertical electrical sounding (CVES) method and TEM. HEM and conventional DC resistivity results were previously compared along a profile that crosses the northern part of the Cuxhaven valley [*Wiederhold et al.*, 2005]. I discuss the advantages, disadvantages, and limitations of both helicopter-borne EM methods.

4.2 Location and Geology of the Cuxhaven Valley

The Cuxhaven valley (Figure 4.2) was carved into Tertiary sediments by melt-water flow during Pleistocene glacial regression epochs after the Elster glaciation 350,000 years ago [*Kuster and Meyer*, 1979; *Wiederhold et al.*, 2005]. The valley is filled with coarse sand and gravel, overlain by fine and medium grained sand and silt. In the upper part of the valley, deposits of Lauenburg clay exist. Existing geological information and resistivity logs, *e.g.*, that at Figure 4.3, show that a large resistivity contrast exists due to thick layers of clay material embedded in a sandy environment.

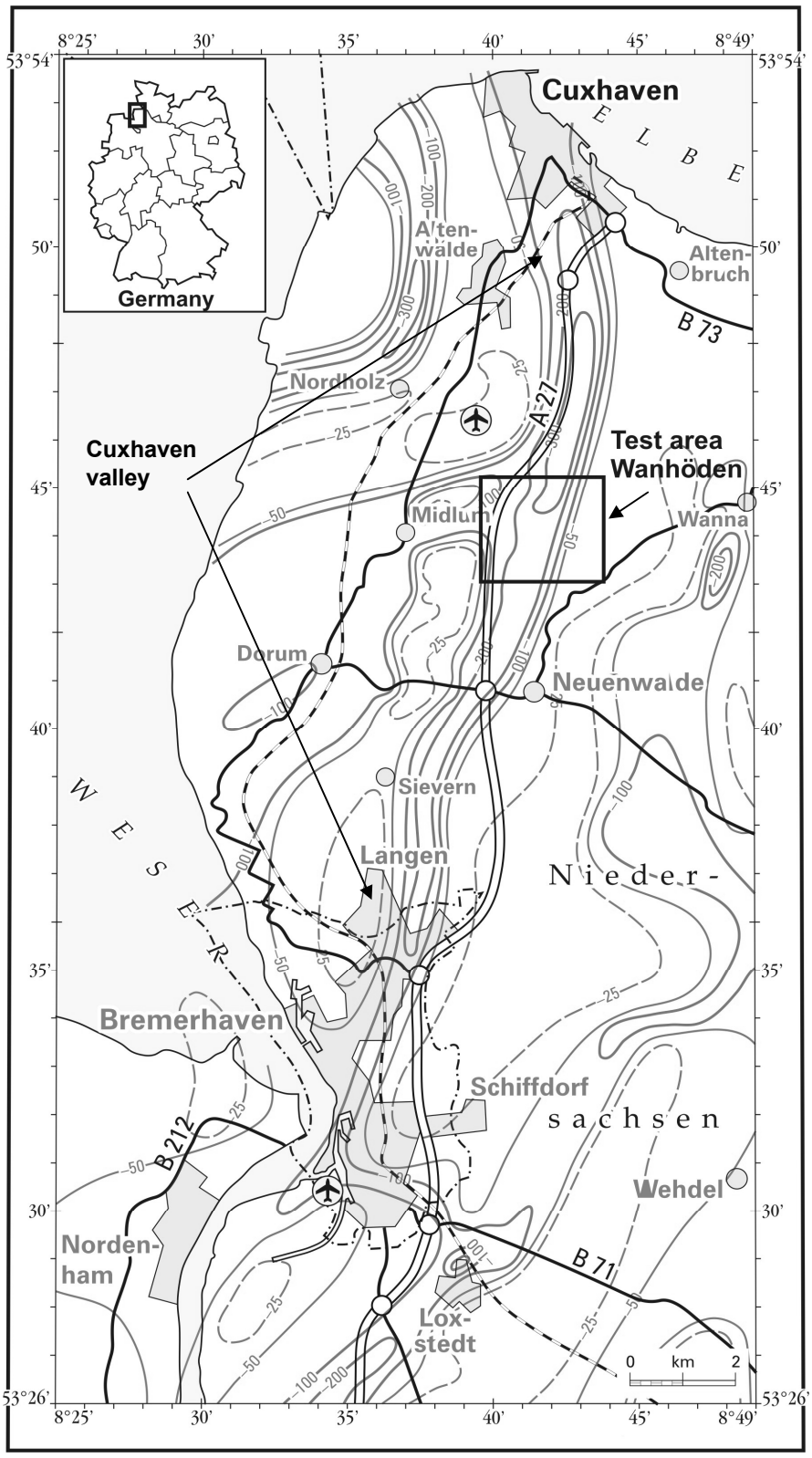

Figure 4.2: *Location of the Cuxhaven valley. The contour lines of the Quaternary base (after Kuster and Meyer [1995]) show that the Cuxhaven valley extends north–south from the city of Cuxhaven to the city of Bremerhaven. The test area Wanhöden (rectangle) is located in the central part of the Cuxhaven valley.*

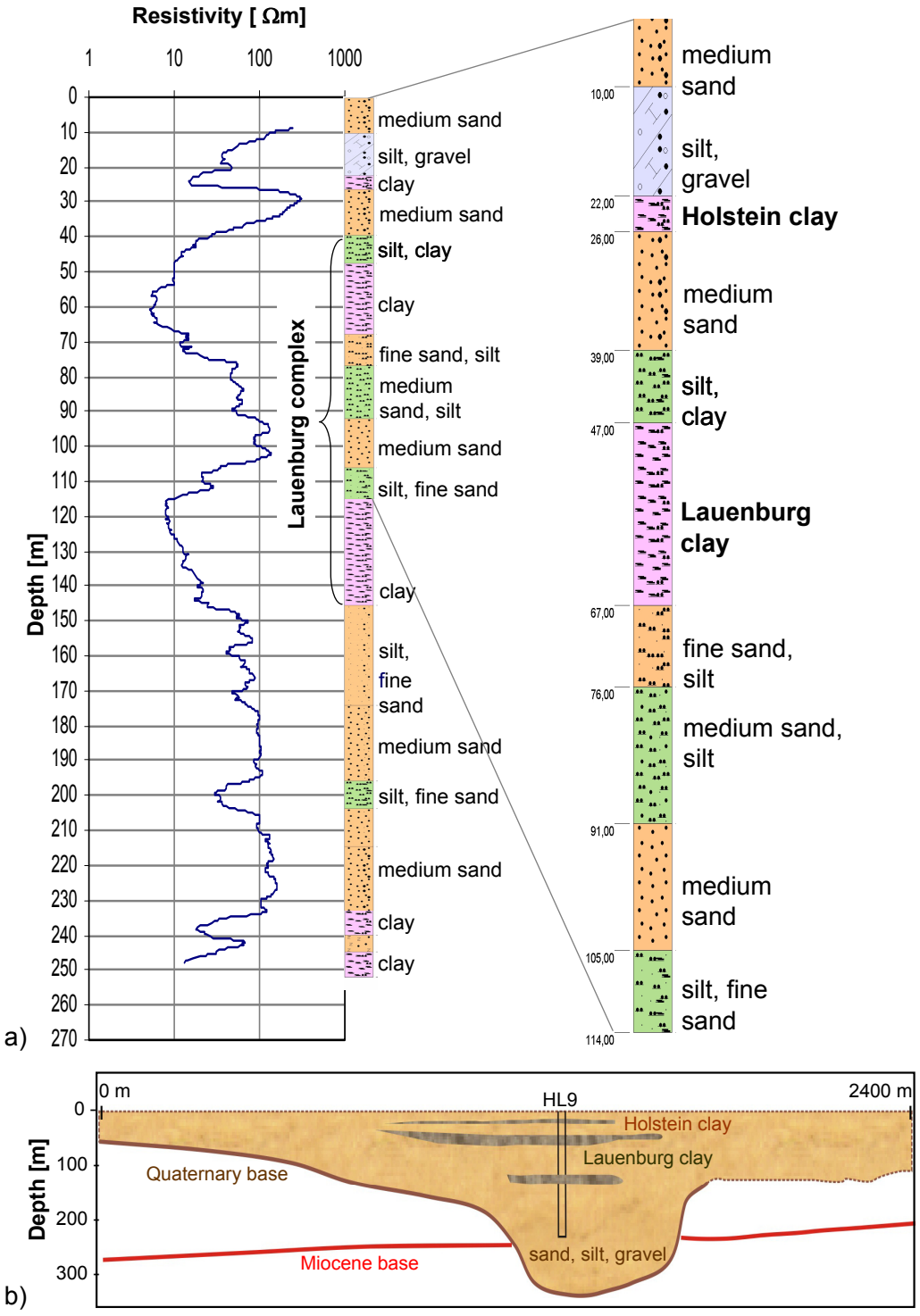

Figure 4.3: *a) The resistivity log and the lithological log of drilling HL9 [Besenecker, 1976] located in the test area Wanhöden (cf. Figure 4.4) show the conductive clay layers which are the target of the EM measurements. b) Sketch of the expected valley fill derived from HL9. Quaternary and Miocene base are derived from a seismic section 300 m northwards of HL9 (cf. Figure 4.5).*

A part of the Cuxhaven valley, the test area Wanhöden, was selected for detailed geophysical surveying including reflection seismics, gravity, DC resistivity, and HEM [*Gabriel et al.*, 2003; *Wiederhold et al.*, 2005], and ground-based and airborne TEM. The locations of the sections of the geophysical methods compared in this study are shown in Figure 4.4.

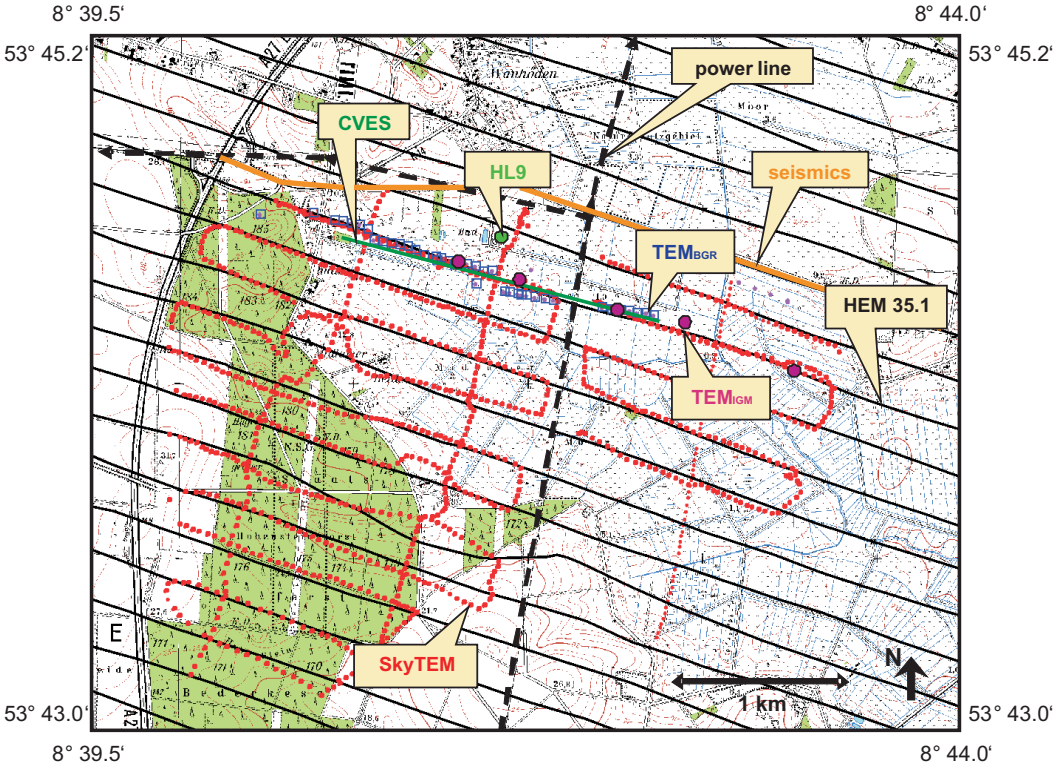

Figure 4.4: *Location map of the test area Wanhöden. The HEM flight lines are black and the SkyTEM lines are dotted red. The TEM sites of the BGR (blue squares), of the IGM (pink points) and the CVES profile (green line) are located parallel to HEM line 35.1. The location of the borehole HL9 (green point) is about 200 m farther north.*

A seismic section of the Wanhöden area (Figure 4.5) describes the shape of the valley and its base at 300 m depth.

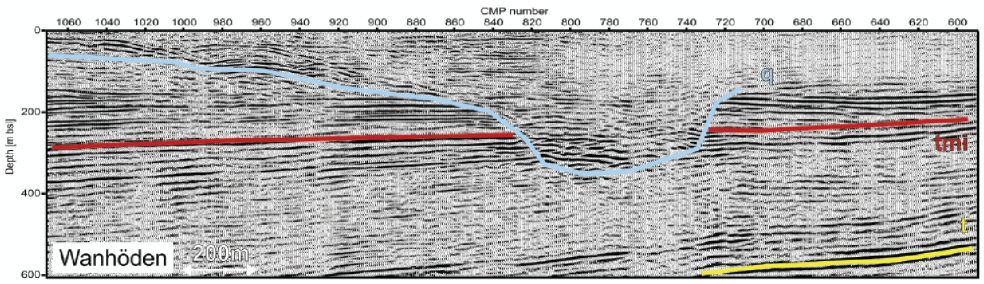

Figure 4.5: *Seismic section at Wanhöden [Rumpel et al., 2006]. For location see Figure 4.4.*

4.3 HEM Survey

The Federal Institute for Geosciences and Natural Resources (BGR) investigated the survey areas Cuxhaven and Bremerhaven in 2000 and 2001 using its helicopter-borne geophysical system (Figure 4.6), which simultaneously records EM, magnetic, and radiometric data. An area of more than 1,000 km^2 was covered within 19 days. The spacing between flight lines was 250 m and the tie-line spacing was 1,000 m; a total of approximately 5,000 line-kilometers was covered [*Siemon et al.*, 2004; *Eberle and Siemon*, 2006].

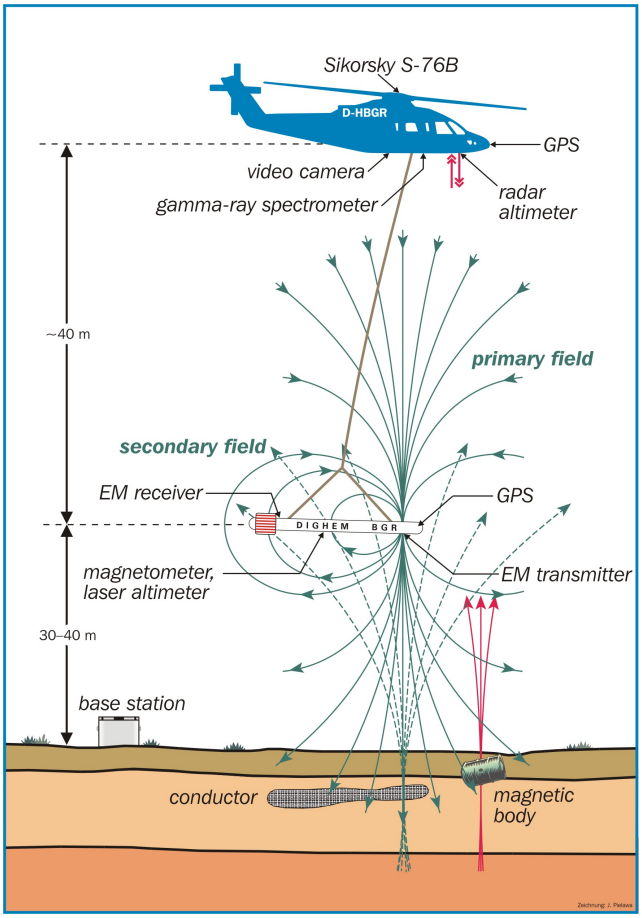

Figure 4.6: *Helicopter-borne geophysical system operated by BGR: The frequency-domain HEM system (Fugro Airborne Surveys) and a cesium magnetometer are installed in the bird. The helicopter is also equipped with a gamma spectrometer, differential GPS, a video camera and a radar-altimeter. (Figure taken from Siemon [2006a].)*

4.3.1 BGR HEM system

The HEM system used for the Cuxhaven survey was an analogue DIGHEM$^{\text{V-BGR}}$ bird manufactured by Fugro Airborne Surveys. It operates at five frequencies ranging from 380 Hz to 192 kHz. The transmitters and receivers of the horizontal coplanar coil system are about 6.7 m apart and installed in a tube about 8 m long, the so-called bird. *Siemon et al.* [2002] describes this analogue HEM system in detail.

In 2004 BGR purchased a digital five-frequency device operating at the frequencies of 387, 1,820, 8,225, 41,550, and 133,200 Hz. Separations of the horizontal coplanar transmitter/receiver coils are about 8 m. In 2006, the digital bird was extended with a sixth frequency of 3,300 Hz using vertical coaxial coils (Figure 4.7).

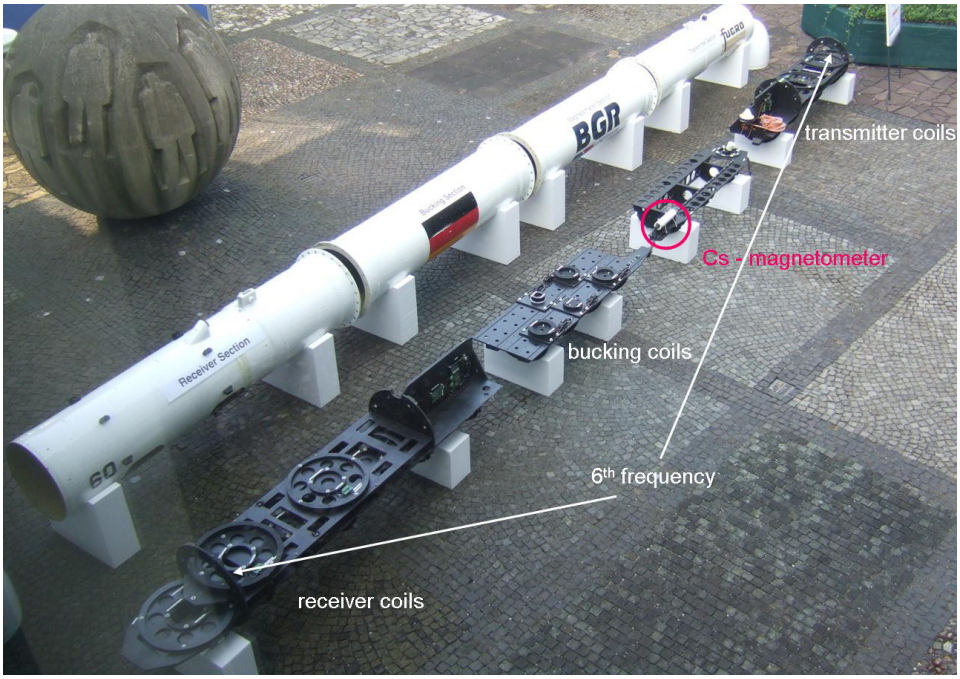

Figure 4.7: *The dip inside the bird bares the six frequency EM coil system and the cesium vapor magnetometer. (Picture: Jens Pielawa, BGR.)*

The positioning of the helicopter and the bird is provided by GPS/GLONASS. Laser and radar altimeters record the altitudes of the HEM system and the helicopter, respectively. The nominal ground clearance of the bird is 30–40 m. The sampling rate of 10 Hz provides sampling distances of about 4 m at a flight velocity of about 140 km/h.

4.3.2 Processing of HEM data

The HEM data are measured as ratios of the secondary to the primary magnetic fields, as discussed in Section 2.4.1. Due to the induction process within the earth, there is a phase shift between the primary and secondary field, *i.e.*, the relative secondary magnetic field is a complex quantity having in-phase and quadrature components. As the secondary field is very small with respect to the primary field, the primary field is generally bucked out and the relative secondary field amplitude and phase is measured in parts per million (ppm).

To obtain useful data, the measured relative secondary field values require careful calibration, leveling, and filtering [*Valleau*, 2000]. These processing techniques are described in detail in *Siemon* [2006*c*; 2007].

Calibration

The HEM system of the BGR was calibrated by the manufacturer (Fugro) on highly resistive ground using well defined external calibration coils. Internal calibration coils (the bucking coils) are used to automatically adjust the phase-shift for each frequency at the beginning of a survey flight. The calibration signals are tuned to generate constant in-phase and maximum quadrature signals. Phase and gain are checked several times during a survey flight at high altitude, *e.g.*, at the end of each flight line. An altitude greater than 350 m above ground level is adequate to decrease the signal of the secondary field below the system noise level. At this high altitude remaining signals due to insufficiently bucked-out primary fields, coupling effects with the helicopter or system drift can be detected.

Standard zero-leveling

The compensation of the primary field using the bucking coil signals is often insufficient. Therefore, the remaining parts of the primary field, the zero levels, are determined at high altitudes where the ground response is negligible. Temperature changes during the survey flight can affect the coil characteristics and the system electronics, which causes a zero-level drift. In order to measure the long-term quasi-linear drift, the zero levels are picked several times during a survey flight. The field values are corrected by subtracting linearly interpolated zero levels.

Microleveling

Short-term zero-level variations caused by temperature changes due to altitude variations can result in stripe patterns on thematic maps and cannot be corrected successfully by standard zero-leveling. As the in-phase and quadrature values are strongly dependent on the sensor altitude, a direct leveling of the relative secondary fields is not suitable in most cases. Instead, the half-space parameters, apparent resistivity and apparent depth, were leveled and then recalculated to the relative secondary field values. The zero-level errors are then derived from the low-pass filtered differences of measured and recalculated secondary field values.

Noise reduction

External noise from, *e.g.*, power lines, radio transmitters, or radar stations are eliminated by weak low-pass filtering or interpolation procedures.

4.3.3 Analysis of the HEM data

After processing of the HEM data, homogeneous and layered half-space inversion [*Sengpiel and Siemon*, 2000] is applied to interpret the data. The inversion results are presented as resistivity maps and vertical resistivity sections.

The leveled in-phase and quadrature values are inverted independently at each site based on both homogeneous half-space and layered half-space models. Homoge-

neous half-space inversion uses single frequency HEM data sets (*i.e.*, the inversion is done for each HEM frequency individually); the multi-layer (1D) inversion uses HEM data from all available frequencies.

Apparent-resistivity and centroid-depth maps

The results of the HEM survey covering the area between the estuaries of the Elbe and Weser rivers provide information about the resistivity distribution of the entire survey area. An apparent resistivity map is shown in Figure 4.8.

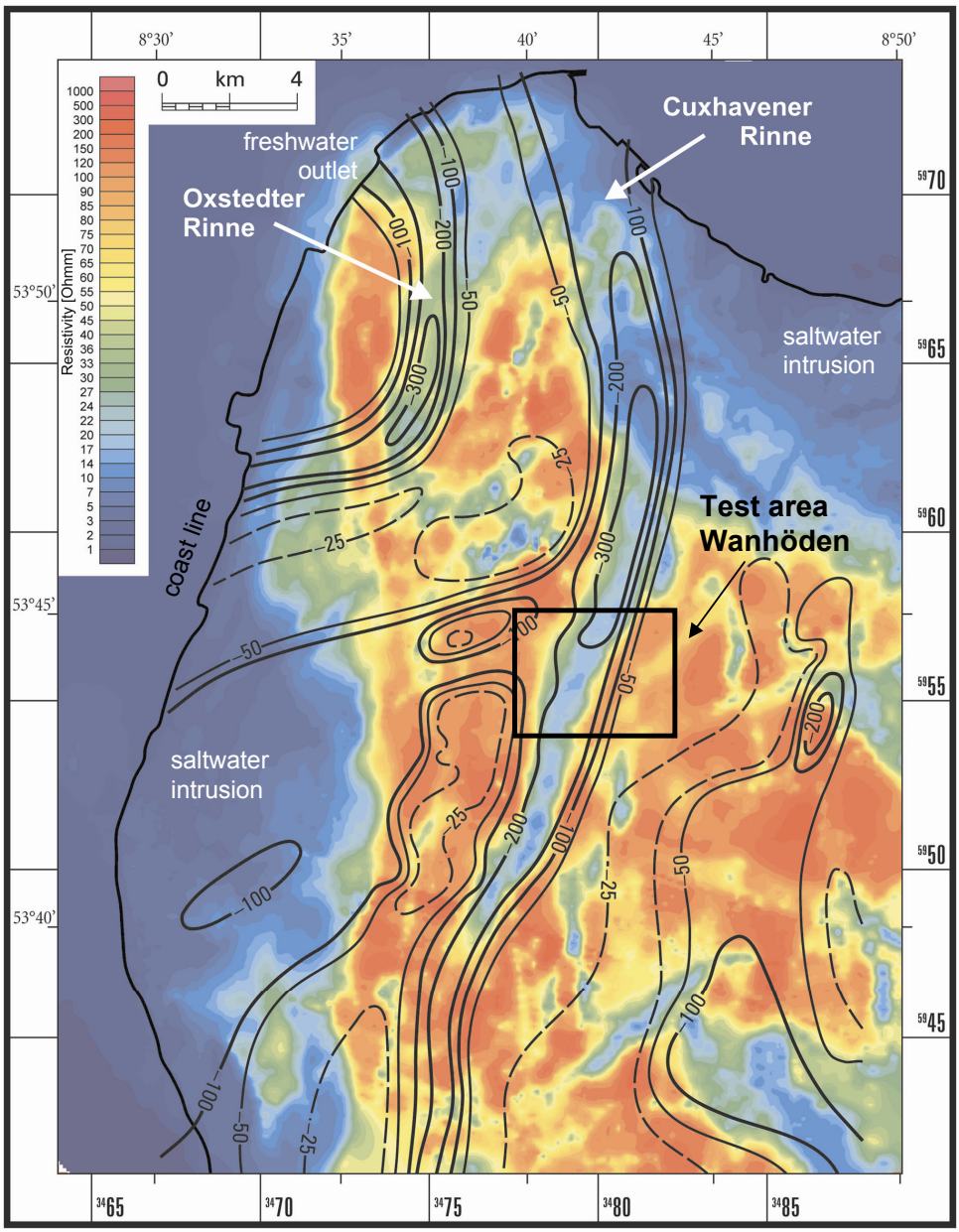

Figure 4.8: *Apparent-resistivity map derived from HEM data at a frequency of 1.8 kHz (after Siemon [2006b] including contour lines of the Quaternary base in meters (after Kuster and Meyer [1995]). The black box shows the location of the test area Wanhöden.*

Saltwater intrusions from the North-Sea into the western and north–eastern part of the survey area are illustrated by blue colors (low resistivities) encroaching from the sea beyond the coastline. A freshwater outlet discharging into the Wadden Sea on the north-west coast is defined by green colors ($\approx$ 17–30 Ωm) extending into the sea from the land. The most prominent feature in Figure 4.8 is an anomalously conductive, linear N–S striking feature, stretching for $\approx$ 20 km through the center of the map. This structure correlates with the Cuxhaven valley [*Kuster and Meyer*, 1995] and was identified by lithological logs (*e.g.*, Figure 4.3) as clay deposits on top of the valley [*Siemon et al.*, 2004].

To focus on the test area Wanhöden, apparent-resistivity maps with their relating centroid-depth maps are displayed in Figure 4.9. These maps display the apparent resistivity structure with increasing depth. The near surface structure is visible at the data of 193 kHz. The course of the valley is indicated by the conductive clay deposited inside the valley at the deeper penetrating frequencies of 384 Hz and 1.8 kHz.

HEM inversion

Marquardt's iterative inversion technique (see Section 3.4.1) using the procedure described by *Fluche and Sengpiel* [1997] and *Sengpiel and Siemon* [2000] is used for 1D inversion. This type of inversion requires a starting model, which is derived from the apparent-resistivity *versus* centroid-depth values obtained from the homogeneous half-space inversion [*Siemon*, 2001]. The inversion procedure is terminated when the reduction of the misfit between measured and modeled data is reaching a given threshold of 10%. The inversion result is a resistivity model described by the resistivities and thicknesses of the model layers.

Starting model The automatically generated standard starting model has as many layers as frequencies used. The resistivities of the starting model are set to the apparent resistivities (previously determined) and the boundaries are chosen as logarithmic means of the corresponding centroid-depth values. The standard starting model settings can be adjusted to allow an additional cover layer, to stretch or compress the depths of the layer boundaries and other scenarios. Thus, a common setting of the *starting model generator* can be defined for the entire survey area, which produces individual starting models for each data set.

Vertical resistivity section In Figure 4.10 HEM 1D inversion results are shown as vertical resistivity section for two 4-layer starting models using different stretching factors for the depth boundaries. Red colors are associated with resistive material of more than 100 Ωm such as sand and gravel layers. Blue colors indicate conductive clay. The inversion results at Figure 4.10b show a better agreement with the lithological log (Figure 4.3) and are therefore used in the following.

HEM detects two conductive layers inside the valley of about 30 Ωm and 7 Ωm at about 20 m and 40 m depth, respectively. The lithological log confirms that the upper conductor consists of silt and Holstein clay and the lower one of silt and Lauenburg clay. The clay layer fades out to the west of the valley whereas no sig-

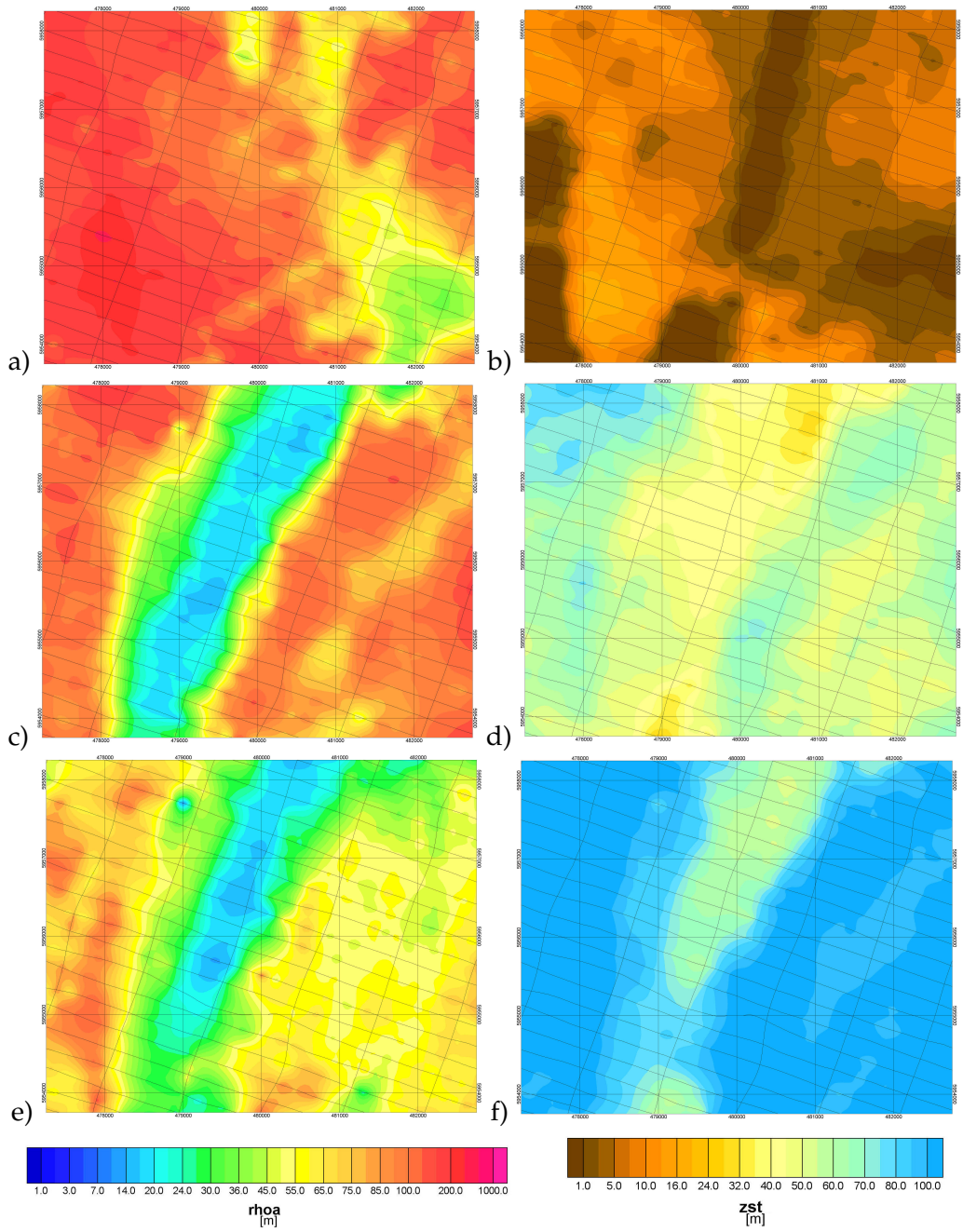

Figure 4.9: *Apparent-resistivity (left) and centroid-depth maps (right) of the Wanhöden area derived for the frequency of: a+b)193 kHz, c+d) 1.8 kHz, and e+f) 384 Hz.*

nificant clay deposits occur in the eastern part of the valley. HEM clearly outlines both lateral extent and depth of the Lauenburg clays. However, the conductive clay and silt layers limit the depth of investigation of the HEM data and the base of this layer is not always resolved.

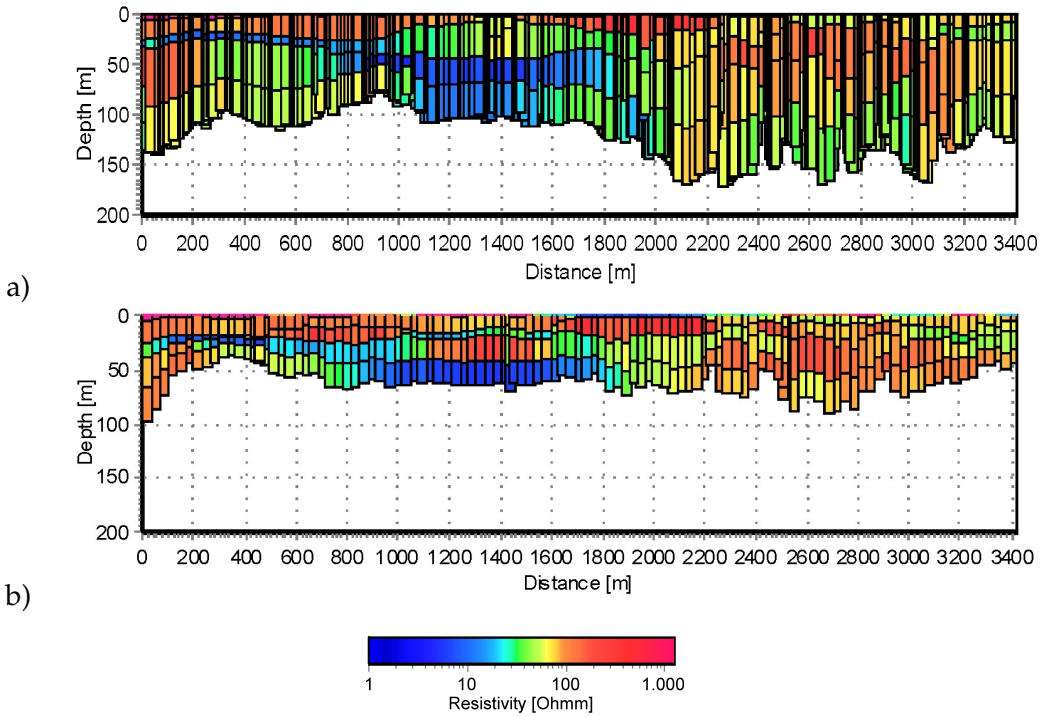

Figure 4.10: *HEM 1D inversion results shown as VRS at line 35.1 obtained by using 4-layer starting models and different stretching factors for the depth boundaries.*

4.4 Continuous Vertical Electrical Soundings

The Leibniz Institute for Applied Geophysics (LIAG) performed 2D resistivity measurements, continuous vertical electrical soundings (CVES), along a profile coincident with line 35.1 (Figure 4.4) to obtain resistivity data which can be compared to the HEM results. A *Geoserve RESECS* multi-electrode system was used, allowing simultaneous setup of 144 electrodes. The data were acquired along a 1,835 m long profile, using a Wenner-Alpha array geometry, with 5, 10, ..., 230, 235 m (max.) electrode separations.

4.4.1 Inversion of the CVES data

The CVES data were inverted using both, conventional 2D inversion (*RES2DINV* code [*Loke and Barker*, 1996]) and laterally constrained inversion (LCI) [*Auken and Christiansen*, 2004]. Figure 4.11 shows a good correlation of both inversion methods. With the LCI technique (Figure 4.11a) is it possible to outline the limits of a shallow clay and a deeper conductive layer of the Lauenburg complex (see Figure 4.3).

In particular the results derived with the LCI technique show a very good correlation with the HEM results. Therefore, only the LCI results are considered in the following text.

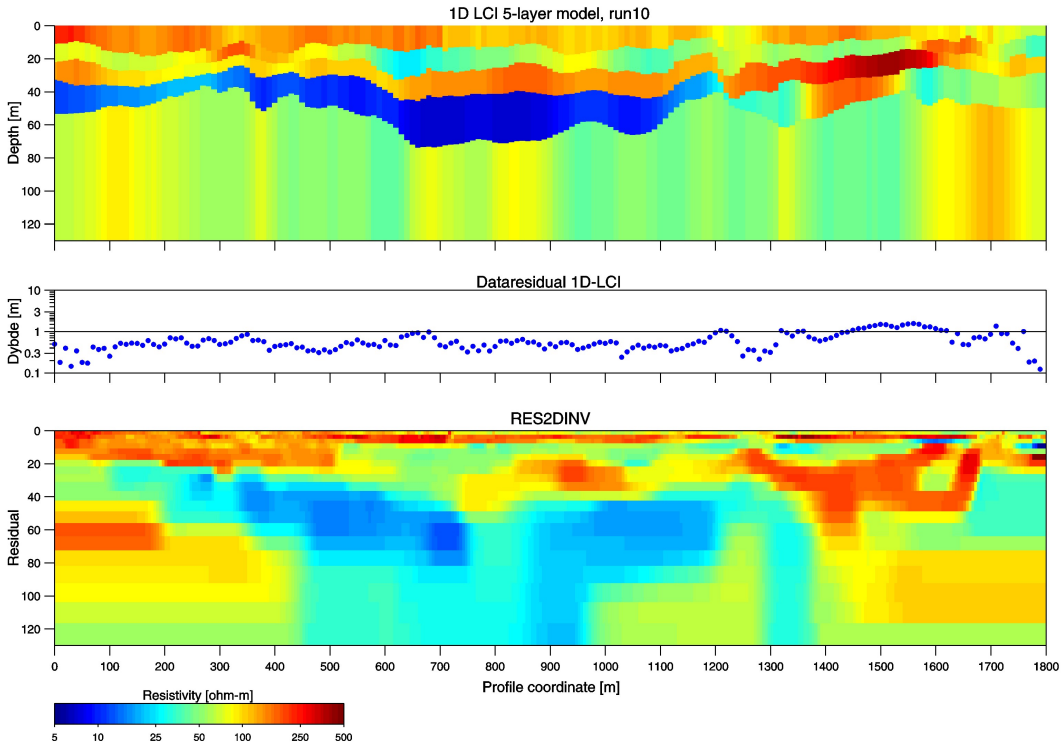

Figure 4.11: *Comparison of the LCI and 2D inversion of CVES data. For location of the section see Figure 4.4.*

4.5 TEM Surveys

A ground-based TEM survey was conducted at the test area Wanhöden in 2005 in order to obtain information about the resistivity distribution at greater depths. The survey line along line 35.1 (Figure 4.4) was chosen for direct comparison with the results from the other geophysical surveys. TEM measurements at 45 sites were carried out along a 2.5 km long section with a site spacing of 50 m inside the valley and 100 m outside the valley.

The TEM measurements were acquired in a central-loop configuration (Figure 2.2) using an analogue *Geonics PROTEM 47* system with a transmitter moment of 30,000 Am^2 (100×100 m^2 transmitter loop and 3 A transmitter current). The effective area of the receiver loop was 31.4 m^2. Three time segments (6–707 μs, 49–2,850 μs, and 101–7,040 μs) with gains of 2, 64, and 128 were measured in order to resolve the signals over the complete voltage range.

In Figure 4.12 the voltage decay over time of two sites is shown. The time range extents from 6 μs to 7 ms after the transmitter current is switched off. Inside the valley, at station 22, the voltage decays less rapidly than outside the valley, at station 10, which is an indication of a conductive structure within the valley.

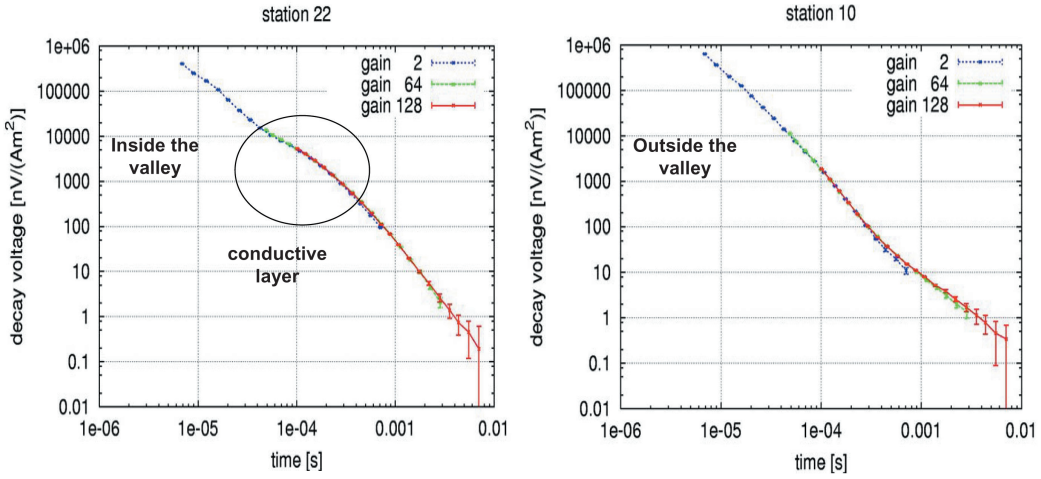

Figure 4.12: *Voltage decay as function of time measured inside (station 22) and outside (station 10) the buried valley. Significant differences occur at medium times around 10^{-4}s. Inside the valley the voltage decays less rapidly than outside the valley, an indication of a conductive structure inside.*

4.5.1 Analysis of the TEM data

Each TEM measurement consists of 6 data sets per time segment with 1,000 stacks per data set. The data were averaged and combined to form one transient decay curve. The standard deviation at times earlier than 3 ms is below 1%, at later times it is on the order of 10%.

The data were inverted individually using *em1dinv* [*HGG*, 2007*b*], a standard least squares inversion algorithm. The 1D forward modeling used in *em1dinv* is de-

scribed in *Auken et al.* [2002]. Residuals and standard deviation factors (STDFs), as defined in Section 3.6.4, were used to evaluate the inversion results.

Figure 4.13 shows a resistivity-depth section derived from the TEM data, residuals and STDFs of an inversion with a 4-layer starting model for each sounding. Nearly all parameters are well resolved (STDF ≤ 1.2) or moderately (STDF ≤ 1.5).

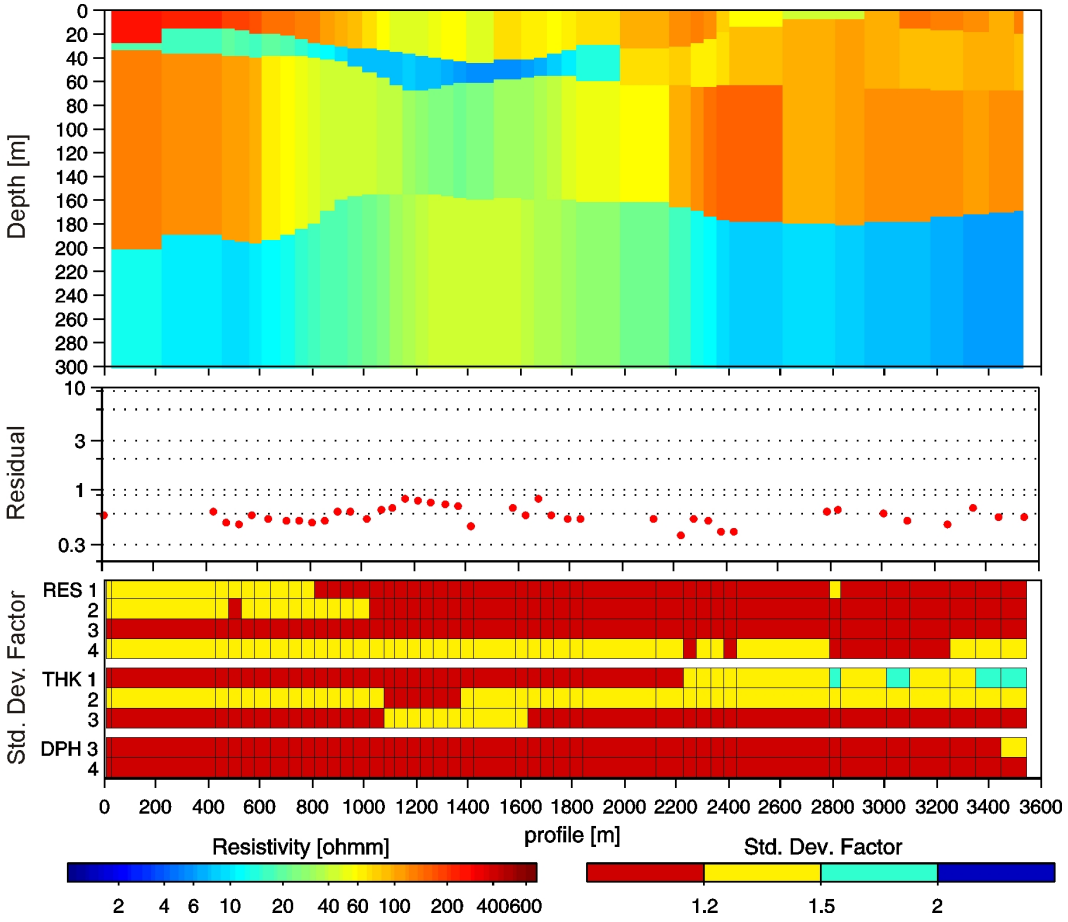

Figure 4.13: *TEM 1D inversion results at line 35.1: resistivity-depth section (top), residuals (middle), and STDFs (bottom).*

The starting models were optimized for each individual sounding by trial and error fine tuning of the model parameters considering their STDFs and the residuals. The optimization procedure resulted in: 4-layers west of the valley, 3-layers over the valley, and 2-layers east of the valley.

The final results are shown in Figure 4.16. The first layer is less resistive above the valley (about 50 Ωm) compared to outside the valley (about 100 Ωm). A conductive layer of approximately 7 Ωm is detected between 40–60 m depth in the center of the valley. This layer can be interpreted as the Lauenburg clay. The layer fades out to the west of the valley with resistivities of about 20 Ωm. Outside the buried valley another conductive layer is revealed at about 180 m depth, which is interrupted by the valley. This layer can be interpreted as a Tertiary clay layer.

The *PROTEM 47* measurements failed to detect a conductive layer at 115–145 m depth which is known to be present from the lithological log (Figure 4.3) and also the basis of the valley at 300 m depth which is known from seismics and where a

resistivity contrast between resistive valley filling and conductive Tertiary clays is expected.

1D forward calculations

I performed 1D forward calculations of 5-layer models with a thick conductive layer at 40–70 m and a conductive half-space in the depth to show that the transmitter moment of the *PROTEM 47* measurements is not strong enough to resolve the base of the valley at 300 m depth known from seismic results. The variation of the interface depth between the fourth layer and the conductive half-space in the range of 270–330 m demonstrates that at 300 m depth it is difficult to distinguish between 30 m depth separation for the time range covered by the *PROTEM 47* device (Figure 4.14). At a time of 5 ms the relative differences of the models are about 12%, which is in the range of the noise level at that time.

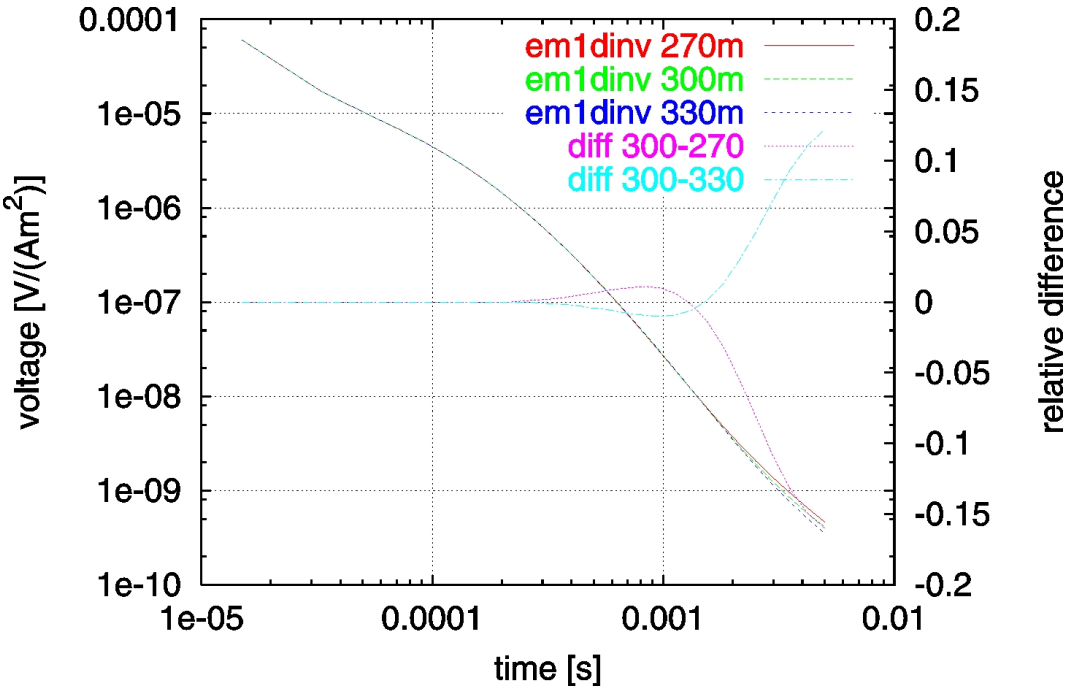

Figure 4.14: *Voltage-time plot of 1D forward calculation results for a 5-layer model with variable boundary depth between the fourth and fifth layer:* ρ_i *= (200, 50, 10, 50, 10)* Ω*m and* $depth_i$ *=(10, 40, 70, 270–330) m.*

4.5.2 TEM with a high transmitter moment

The 1D forward calculation showed that the response of a 300 m deep conductive half-space is detectable at times later than 5 ms. A larger transmitter moment is required to determine the depth of the valley. This produces a higher signal-to-noise ratio at late times and smaller data uncertainties.

Additional ground-based TEM measurements were acquired with a higher transmitter moment by the Institute for Geophysics and Meteorology (IGM) of the University of Cologne at five sites (for locations see Figure 4.4). For late-time measure-

ments a high transmitter moment of 3,200,000 Am^2 was realized using a transmitter size of 400×400 m^2 and a transmitter current of 20 A. For early time measurements a current of 12.7 A was used. The measurements were conducted with the *GGT* transmitter and the *GDP 32* receiver of *Zonge Engineering*. For more details see *Mbiyah* [2006]. The results were published by *Tezkan et al.* [2008].

The transmitter moment of the TEM measurements performed by the IGM, was 100 times greater than the *PROTEM 47* moment. The transmitter moment TM is related to the investigation depth d_{inv} by Equation 4.1, *Spies and Frischknecht* [1991]:

$$d_{inv} \propto TM^{1/5} \tag{4.1}$$

The IGM transmitter therefore has a theoretical investigation depth 2.5 times greater than the *PROTEM 47* moment.

As an example the transient of site 5R is shown in Figure 4.15. The data cover a time range of approximately 100 μs – 400 ms. The standard deviation of the stacked data, which quantifies the noise, is shown as error bars in the late time signals and is less than 10% for the whole time range.

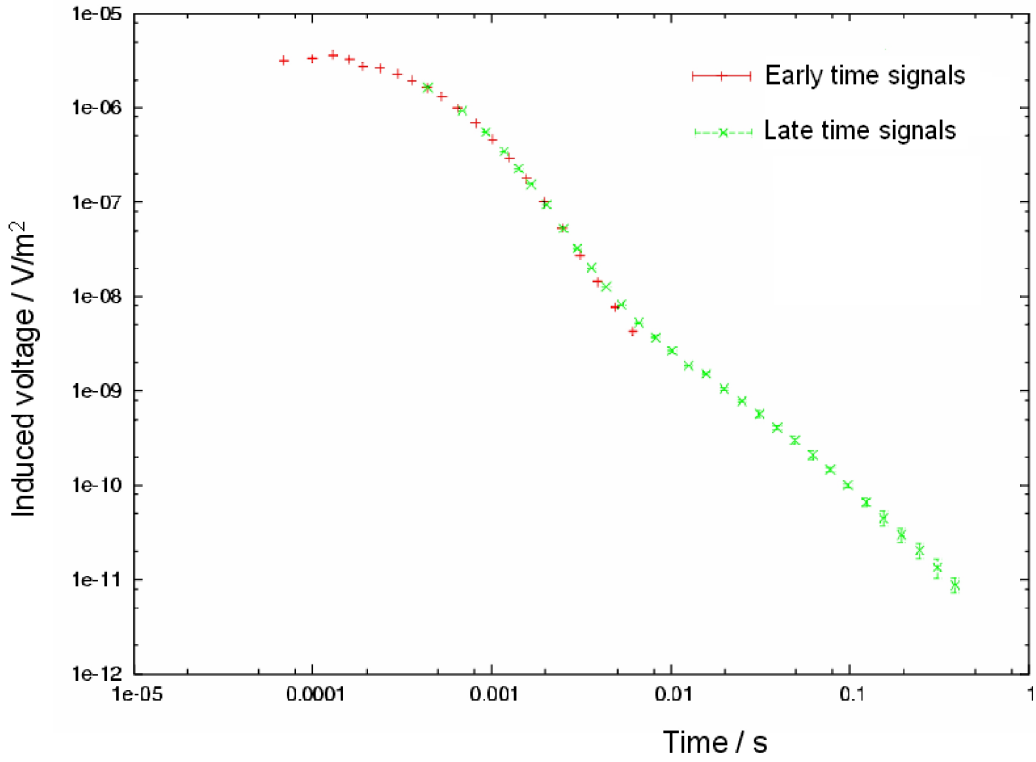

Figure 4.15: *Transient of a high-moment ground-based TEM measurement performed by IGM at site 5R inside the buried valley [Mbiyah, 2006]. The standard deviation of the stacked data is shown as error bars in the late time signals and is less than 10% over the whole time range.*

As seen in Figure 4.16, the high-moment measurements detect a conductive layer at about 300 m depth, which can be interpreted as Tertiary clay and, referring to the seismic section, as base of the valley. The determined thickness of the Lauenburg clay is in the range of the *PROTEM 47* results, but the location is shifted. This is due to the relatively late recording start caused by a long ramp time of 136 μs for early time measurements. As a result, the near surface resistivity structure is not well resolved. Also the high-moment measurements of the IGM failed to detect the conductive layer at 115–145 m depth. A possible explaination is that this layer has a low resistivity contrast and/or is only locally present.

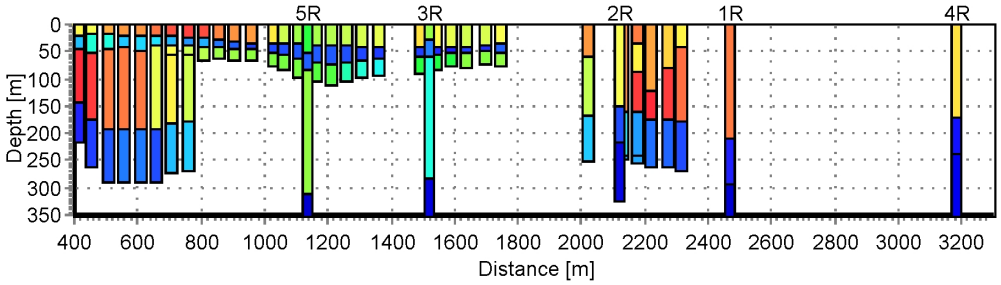

Figure 4.16: *1D inversion results of BGR and IGM ground-based TEM measurements at line 35.1. The labeled columns (1R-5R) are results of IGM measurements with a high transmitter moment.*

4.6 SkyTEM Survey

A SkyTEM survey was conducted at the Wanhöden survey area as part of the BurVal project in 2005 [*Foged et al.*, 2005]. The flight lines of this survey were as coincident as possible with the HEM flight lines and covered an area of about 8 km^2 (Figure 4.4).

4.6.1 The SkyTEM system

Figure 4.17 shows the SkyTEM system developed by the HydroGeophysics Group (HGG) of Aarhus University. Besides TEM equipment, the system comprises two DGPS receivers, two laser altimeters, and two inclinometers mounted on a six-sided lattice frame, made of PVC and Kevlar. The laser altimeters measure the ground clearance and the inclinometers measure the tilt of the frame. The system was flown at an altitude between 10–25 m over ground.

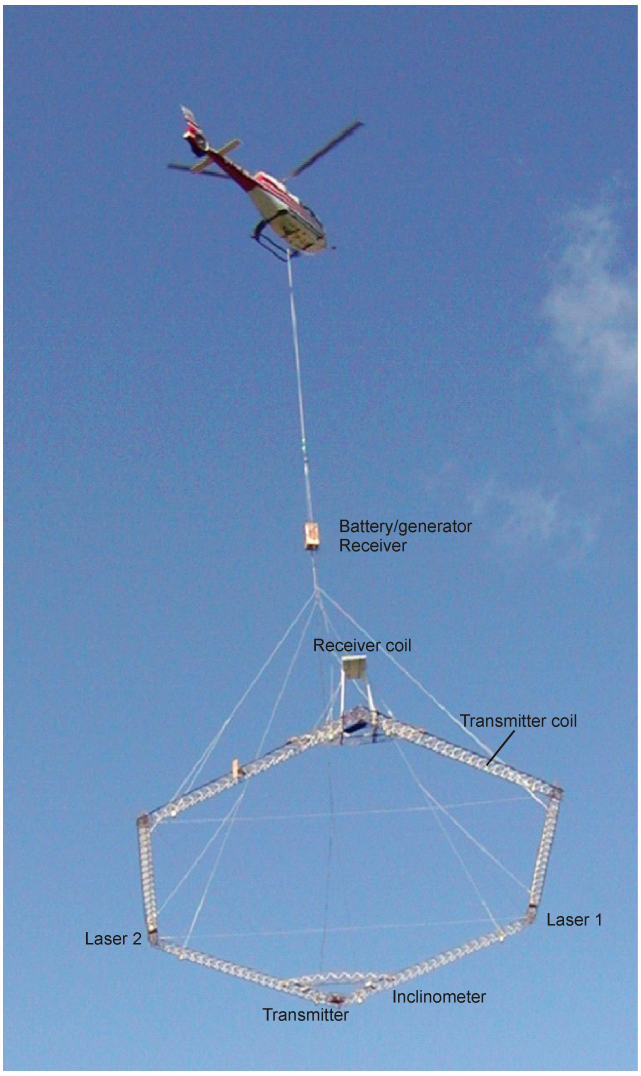

Figure 4.17: *SkyTEM, the time-domain HEM system developed at Aarhus University. (Picture taken from Foged et al. [2005].)*

The transmitter

The transmitter loop used for the SkyTEM survey at the Wanhöden area covers an area of approximately 283 m^2 per turn. The measurements were carried out with low and high transmitter moments. A current of 40 A in one loop turn generated a low transmitter moment of approximately 9,000 Am^2. A high moment of approximately 47,000 Am^2 was obtained with a current of 40–50 A in four loop turns. The waveform was a square wave running a 50% duty cycle at the repetition frequencies of 185 Hz for the low moment and 42 Hz for the high moment. A DC generator provided power for the system. The generator was placed at a safe distance between the helicopter and the transmitter loop to mitigate any noise and bias signals.

The high SkyTEM transmitter moment (TM) was about 1.5 times higher than the *PROTEM 47* moment, so that a 10% higher investigation depth can be theoretically achieved ($d_{inv} \propto TM^{1/5}$; *Spies and Frischknecht* [1991]).

The receiver

The receiver coil was a shielded, over-damped multi-turn loop with a cut-off frequency of 450 kHz. It was placed parallel to, and 1.91 m above the transmitter loop to record the vertical (z-) component of the magnetic field. This configuration is chosen in order to efficiently suppress weak off-time currents in the transmitter loop.

Voltage data of low and high moment measurements were recorded in the time interval of 17–1,400 μs and 150–3,000 μs, respectively. Consequently, the time range is shorter than that of the *PROTEM 47* measurements and the advantage of the higher transmitter moment is lost.

Measurements were gathered in cycles of four data sets with low moment (320 stacks per data set) and four data sets with high moment (192 stacks per data set). The data from each cycle were averaged to one low and one high moment data set which were then interpreted as one geophysical model. At an average flight speed of 18 km/h one sounding per 80 m was obtained.

4.6.2 Analysis of the SkyTEM data

The SkyTEM data were processed using *Workbench* [*HGG*, 2007*c*] software. *Workbench* provides an automatic processing tool including filtering, averaging, and other tools. For the correction of GPS, tilt, and altitude different filters were applied. The processing of the voltage data includes tilt correction, culling of coupled raw data, averaging, and culling of noisy averaged data. After automatic processing is complete, the data have to be inspected and manual corrections can be done. Automatic and manual processing of SkyTEM data with *Workbench* are described in *HGG* [2007*a*].

SkyTEM data were inverted using *em1dinv* [*HGG*, 2007*b*], the same inversion code as for the ground-based TEM soundings (Section 4.5.1). The 1D inversion results at line 35.1 are consistent with the *PROTEM 47* results (Figure 4.18).

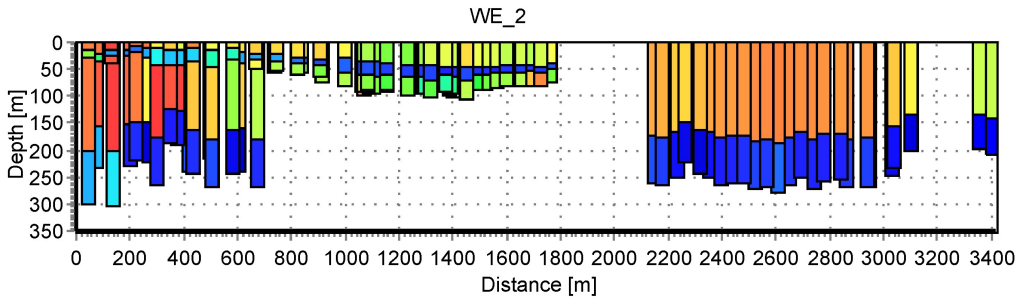

Figure 4.18: *1D inversion results of SkyTEM measurements at line 35.1.*

To evaluate the inversion results I analyzed the significance of the model parameters using the residuals and the standard deviation factors (as defined in Section 3.6.4). Here, I demonstrate this for the second layer, which is the Lauenburg clay layer inside the valley.

Figure 4.19 displays the STDFs of the resistivity and thickness of the second layer as colored maps. The standard deviation factor of the resistivity and thickness of the clay layer is less than 1.2 (Figure 4.19), thus they are well resolved. East of the valley, the second layer is the conductive Tertiary clay (cf. 4.18), and the resistivity is also well resolved (Figure 4.19a). At locations where the data were fitted with a two-layer model, there is no thickness and thereby no standard deviation of thickness of the second layer (Figure 4.19b). West of the valley the second layer is less conductive and both, resistivity and thickness are poorly resolved or unresolved.

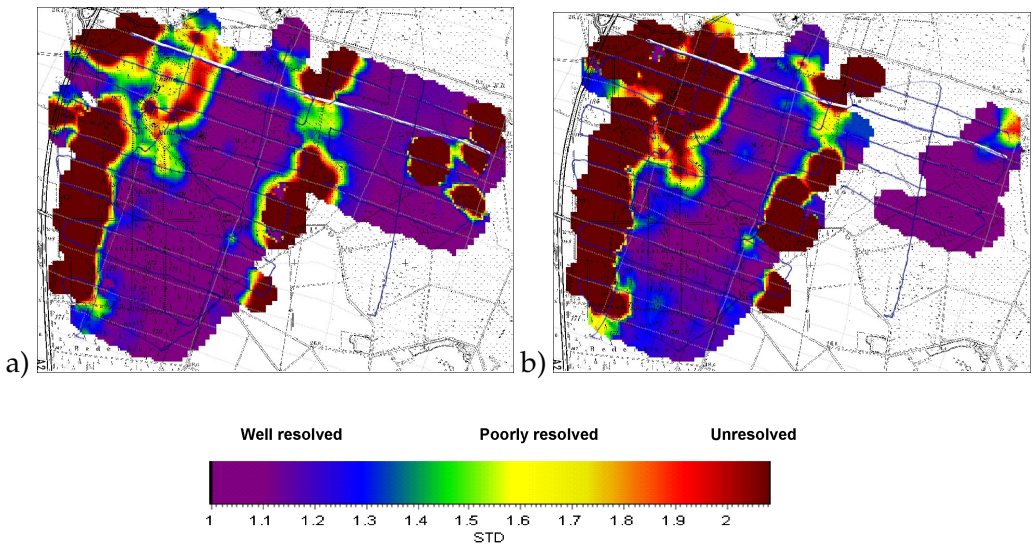

Figure 4.19: *Maps of the standard deviation factors (STDFs) of a) the resistivities of the second layers and b) the thicknesses of the second layers. The white line indicates line 35.1.*

4.7 Comparison of the Inversion Results

In the following, I compare the airborne and ground-based geophysical inversion results of systems with comparable investigation depths, *i.e.*, HEM with CVES, and SkyTEM with TEM, along HEM flight line 35.1 (*cf.* Figure 4.4).

4.7.1 Comparison of HEM and CVES

In Figure 4.20a I compare CVES and HEM results along the profile line shown in Figure 4.4. Red colors are associated with resistive material of more than 100 Ωm, *e.g.*, sand and gravel layers. Blue colors indicate conductive clay or saltwater. Both methods detect conductive layers inside the valley of about 30 Ωm and 7 Ωm at about 20 m and 40 m depth, respectively.

The lithological log (*cf.* Figure 4.3) confirms that the upper conductor consists of silt and Holstein clay and the lower one of silt and Lauenburg clay. The clay layer fades out to the west of the valley whereas no significant clay deposits occur in the eastern part of the valley. East of the valley the Holstein clay is visible in the CVES results out to 2,100 m distance along the profile, while the HEM cannot resolve the Holstein clay beyond 1,700 m distance. The CVES and HEM results differ significantly over the profile interval from 1,750 m to 2,200 m. The HEM system had to be elevated to cross a power line resulting in lower signal amplitudes and data distortions due to an EM field induced by current flowing in the power line.

Both methods agree in outlining the upper boundaries of the conductors inside the valley, but give different thickness and resistivity for the upper conductor. This is explained by low resistivity equivalence: the thickness/resistivity ratio is approximately the same for both methods. The base of the lower conductor is revealed by CVES LCI, but not with HEM single-site inversion. This is because the HEM system has a maximum penetration depth of 60 m due to attenuation of signal within the Lauenburg clay.

4.7.2 Comparison of SkyTEM and TEM

The TEM and SkyTEM inversion results are consistent (Figure 4.20b). The uppermost layer is less resistive inside the valley (about 50 Ωm) compared to outside the valley (about 100 Ωm). The lower resistivity of the layer is caused by the upper conductive layer seen in Figure 4.20a which is not resolved but averaged into the first layer in the TEM models. Both, TEM and SkyTEM detect a conductive layer of approximately 7 Ωm between 40–60 m depth – the Lauenburg clay layer – in the center of the valley. This layer fades out to the west of the valley with resistivities of about 20 Ωm. The TEM methods also detect another conductive layer Outside the buried valley at about 180 m depth, which is interrupted by the valley. This layer is interpreted to be a Tertiary clay layer.

Due to the reduced penetration of the EM field caused by highly conductive clay layers, the deep conducting clay layer at 115–145 m depth inside the valley (as seen in the resistivity log in Figure 4.3) is not detectable.

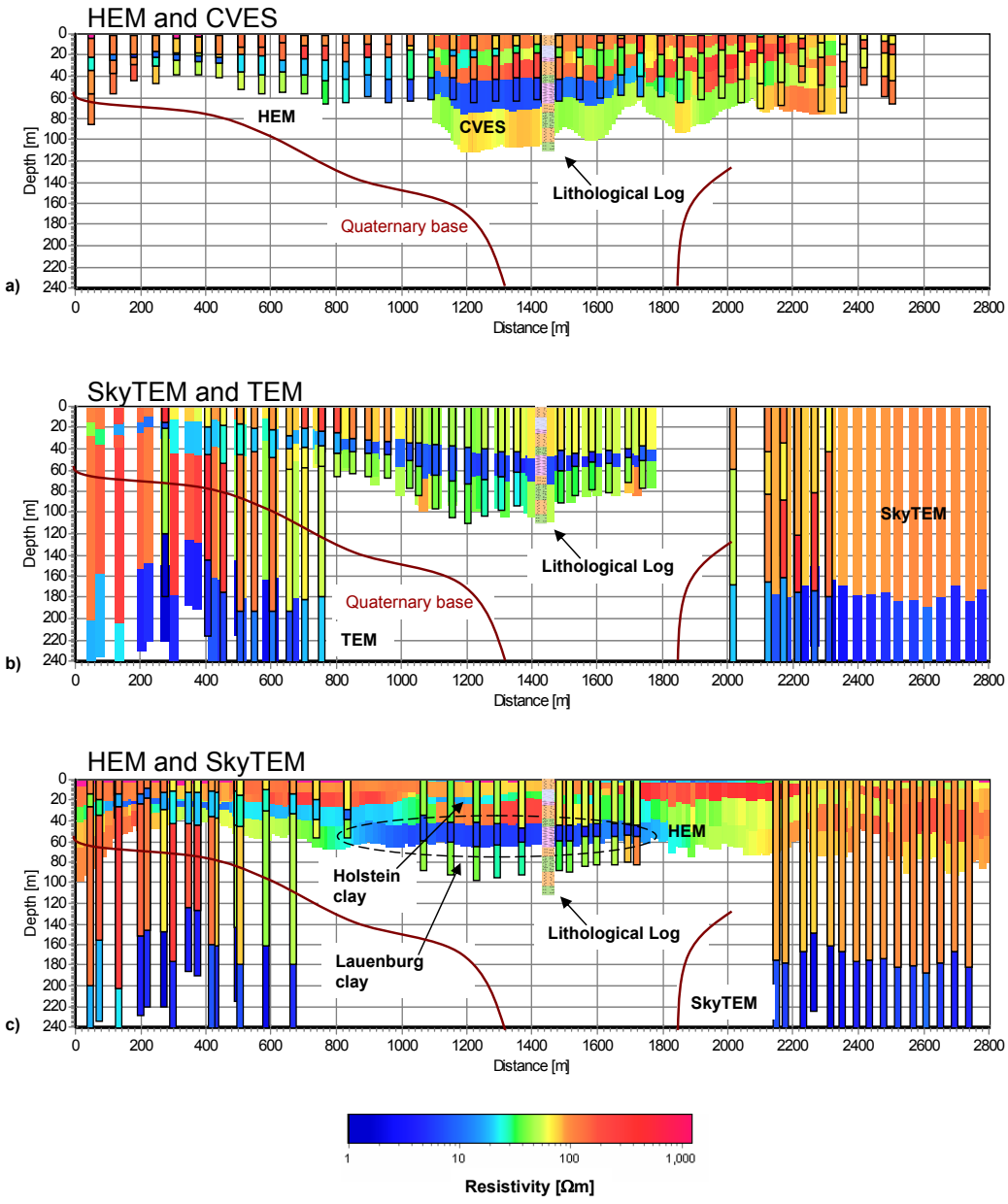

Figure 4.20: *1D inversion results of a) HEM (framed columns, every 8th station of line 35.1) and LCI results of CVES, b) TEM (framed columns) and SkyTEM (broad columns), c) SkyTEM (framed columns) and HEM (broad columns). The Quaternary base (brown line) is interpreted from reflection seismics [Wiederhold et al., 2005].*

4.7.3 Comparison of SkyTEM and HEM

SkyTEM and HEM inversion results (Figure 4.20c) consistently detect the top of the Lauenburg clay at 40 m depth inside the valley. SkyTEM, however, is not able to resolve the Holstein clay at 20 m depth. At the near-surface, HEM has a better resolution and furthermore detects the Holstein clay. SkyTEM reveals the bottom of the Lauenburg clay and a Tertiary clay layer at about 180 m depth outside the valley.

As discussed earlier the HEM resistivities at profile distance 1,750 m to 2,200 m are affected by EM coupling with a power line. The coupling is relatively weak in the higher frequencies and therefore no data have been excluded from the interpretative analysis. The SkyTEM system would have been also affected by the power lines, so the survey was designed to avoid flight lines that cross the power line, which explains the gap in the SkyTEM data (*cf.* Figure 4.4).

Figure 4.21 shows average resistivity maps at different depth ranges derived from 1D inversion models of the HEM and SkyTEM data. Thematic maps like the resistivity maps were generated with *Workbench*. Kriging interpolation with a linear variogram fit, a search radius of 300 m, and a grid line spacing of 50 m was used to produce the resistivity maps.

The valley appears in the SkyTEM maps at shallower depths (0–20 m) than in the HEM maps (Figures 4.21a and b). This is caused by the Holstein clay layer, which is not clearly resolved by SkyTEM, but it does reduce the resistivity values in the upper part of the valley as seen in Figure 4.20b. The SkyTEM and HEM resistivity maps are consistent at 20–40 m depth (Figures 4.21c and d) and the Lauenburg clay is clearly revealed by both methods at 40–60 m depth (Figures 4.21e and f).

Because the penetration depth of HEM is lower than of SkyTEM, the bottom of the Lauenburg clay layer is not resolved by single-site inversion of the HEM data and therefore the clay layer appears to be too broad at 60–80 m (Figures 4.21g). However, the SkyTEM maps show that the valley becomes narrower in the 60–80 m depth interval indicating the base of the clay layer (Figures 4.21h).

As the penetration depth of HEM is lower than that of SkyTEM, with HEM single-site inversions and although it actually narrows as seen on the SkyTEM maps. The greenish areas seen in the south-eastern part of Figure 4.21d are due to extrapolation where there is no data coverage.

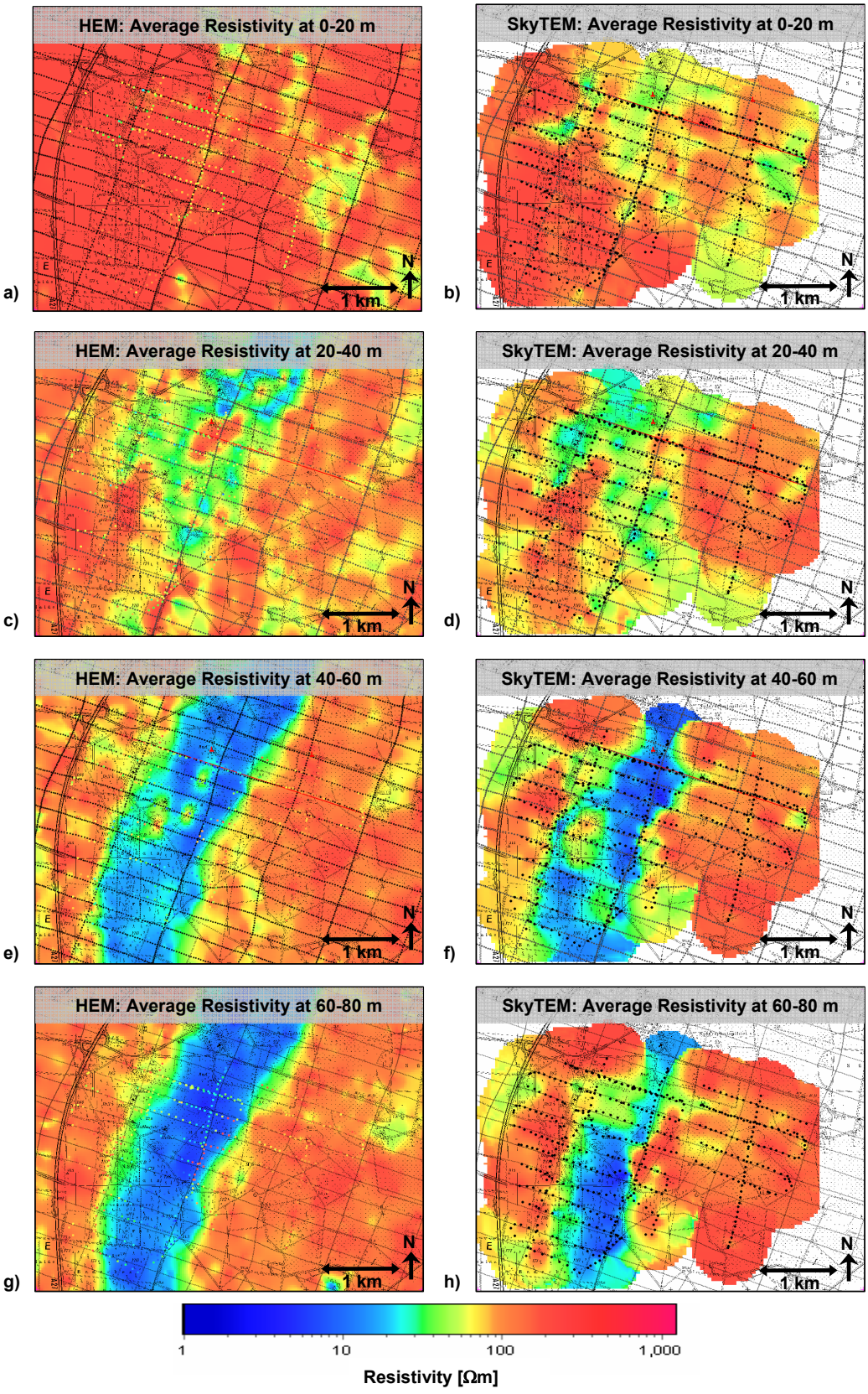

Figure 4.21: *Resistivity maps for different depth ranges derived from 1D inversion results. Maps of the HEM models are in the left, and maps of the SkyTEM models are in the right-hand column. The inversion results of SkyTEM are shown as colored dots in the HEM maps to emphasize differences of both methods.*

Clay thickness maps

Clay layers have a low hydraulic permeability and often serve as protection of underlying aquifers against pollution from the surface. Therefore, the thickness of the clay layer is an important parameter for the protection of groundwater reservoirs and assigned at groundwater protection areas [*Kirsch and Hinsby*, 2006].

The maps in Figure 4.22 show the cumulative thickness of clay layers in the upper 100 m of the valley with resistivities of 5–30 Ωm. Both, SkyTEM and HEM inversions reveal that the cumulative clay thickness inside the valley is greater than 15 m. SkyTEM suggests a smaller clay thickness compared to HEM, because SkyTEM fails to resolve some of the near surface clay layer. However, the clay thickness derived from the HEM data is probably overestimated because the bottom of the Lauenburg clay is not well resolved.

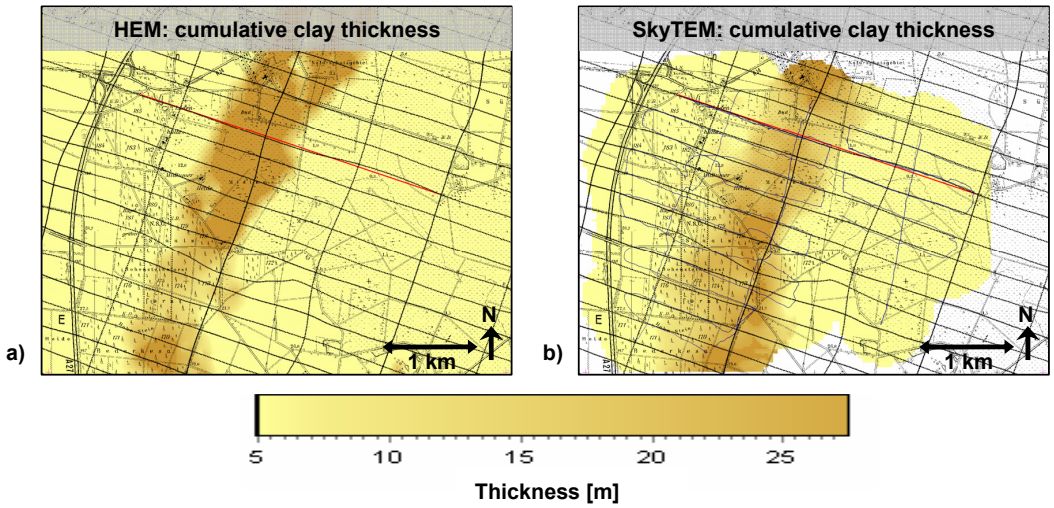

Figure 4.22: *Thickness of the clay layers with resistivities of 5–30 Ωm within the upper 100 m of the buried valley derived from a) HEM and b) SkyTEM data. The red line indicates line 35.1.*

Chapter 5

Spatially Constrained Inversion of SkyTEM and HEM Data

5.1 Introduction

The standard tools for presenting airborne electromagnetic (AEM) data are apparent resistivity maps and conductivity depth sections. As the effort in terms of computing time is high, it is not yet common to carry out 3D inversion in AEM, although large and dense data sets are favorable for 3D interpretation. 1D inversion is the state of the art and cross-sections are derived from stitched together layered half-space models to represent the 3D resistivity distribution.

Viezzoli et al. [2008] developed the spatially constrained inversion (SCI) technique to benefit from the airborne data in another way. Through spatial constraints, information can be spread horizontally to adjacent models. In a sedimentary environment with this technique it is possible to resolve layers which are locally poorly resolved. The theoretical background is described in Section 3.6.5.

I applied the SCI technique to the SkyTEM data set of the Wanhöden survey area, studied the influence of different SCI parameters and compared the SCI results with single-site 1D inversion results. Then I adapted the SCI technique for the use on HEM data, applied it to the Wanhöden data and discussed the improvement compared to individual 1D inversion.

5.2 SkyTEM

The SCI combines a given number of adjacent 1D models with their constraints in one inversion scheme, as described in Section 3.6. This results in a bigger Jacobian matrix. *Viezzoli et al.* [2008] recommend a Jacobian matrix with less than 1,000 model parameters to have reasonable computation times.

The full SkyTEM data set of the Wanhöden survey area contains more than 1,000 soundings and each sounding requires, *e.g.*, 9 parameters if a 5 layer model is

adapted (or 10 parameters if the system altitude is included in the inversion). Thus, the total dimension of the model space is at least 9,000. Consequently, the data set has to be divided into smaller subsets, each of which are individually inverted as a separate unit. The question is how to select survey sites to be combined in a particular subset.

5.2.1 Delaunay triangulation of SkyTEM data

The Delaunay triangulation [*Delaunay*, 1934] is a way to triangulate a set of points in a plane. Thus, the survey sites can be spatially connected for an entire survey area. Figure 5.1 shows the Delaunay triangulation of the SkyTEM sites of the Wanhöden survey area.

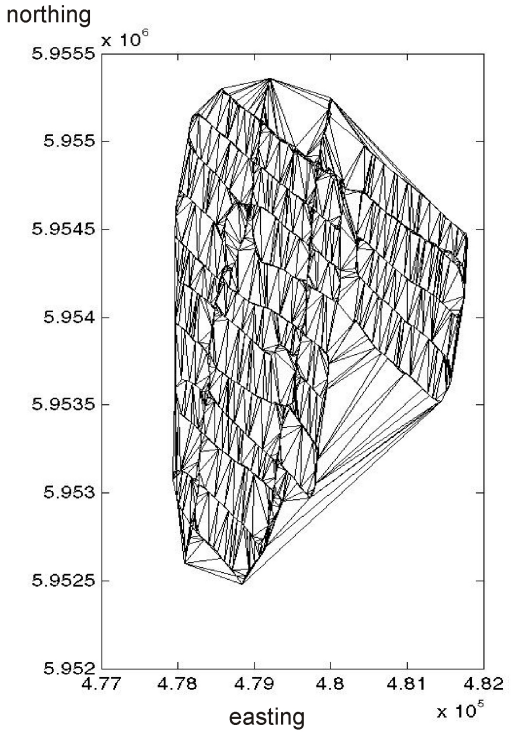

Figure 5.1: *Delaunay triangulation of the SkyTEM sites in the Wanhöden survey area.*

The histogram of the distances between the nearest neighbors (Figure 5.2) is a statistical parameter to describe the result of the triangulation. The maximum at about 40 m indicates the mean site spacing. This is half of the SkyTEM site spacing known from Section 4.6.1, because low and high moment measurements are regarded as separate sounding. The local maxima at 80 m and 120 m (multiples of 40 m) are caused by dropped out soundings. The line separation of 250 m is barely noticeable.

The generation of the subsets (or cells) is initiated at a randomly chosen starting point, which is one of the consecutively numbered survey sites. From that point the cell building runs automatically following the nearest neighbors method considering a predefined cell size. The building of the second cell begins around one of the points at the outer border of the first cell and so on. After all soundings are in-

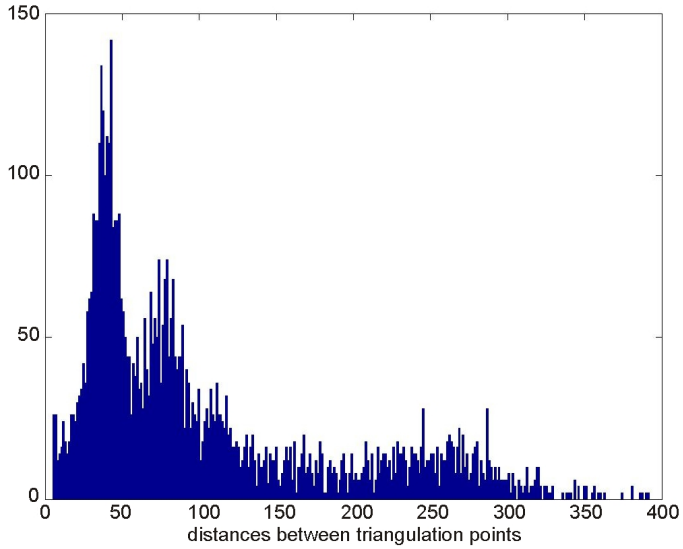

Figure 5.2: *Histogram of the distances between nearest neighbors soundings.*

cluded in a cell, the dimension of these preliminary cells is enlarged by one nearest neighbor in order to get a division of the survey area into overlapping cells. *Viezzoli et al.* [2008] describes this procedure in detail.

The shape and the allocation of the cells vary depending on the used starting point and the desired cell size. In Figure 5.3 the arrangements of the cells for starting point = 1 and starting point = 500 are shown; the desired cell size was 60 for both. The final cell sizes vary and the corresponding histograms show the number of soundings per cell. For example, the configuration with starting point = 1 leads to only 7 cells with less than 15 soundings per cell (Figure 5.3c), whereas the other configuration leads to 12 cells. In this case, the configuration of starting point = 1 is preferred, because small cells may result in discontinuities between adjacent cells. However, a small number of cells minimizes the computing time for inversions. On the other side, a cell with more than 100 soundings slows down the inversion significantly.

5.2.2 Two inversion runs

In a first inversion run the individual cells are inverted via SCI independently of each other. The starting model and the SCI settings have to be defined, the influence is discussed in the following sections. Soundings of overlapping regions belong to at least two cells and are inverted more than once. The output model parameters of those will be the average model parameters defined by the individual cells weighted against their standard deviation.

In order to preserve continuity across the subsets a second inversion run is carried out. Therefore, the inversion models of the first run are used as starting models. The model parameters of the overlapping regions, which contain information of adjacent cells, are fixed as *a priori* information. From there the information is spread within the cells.

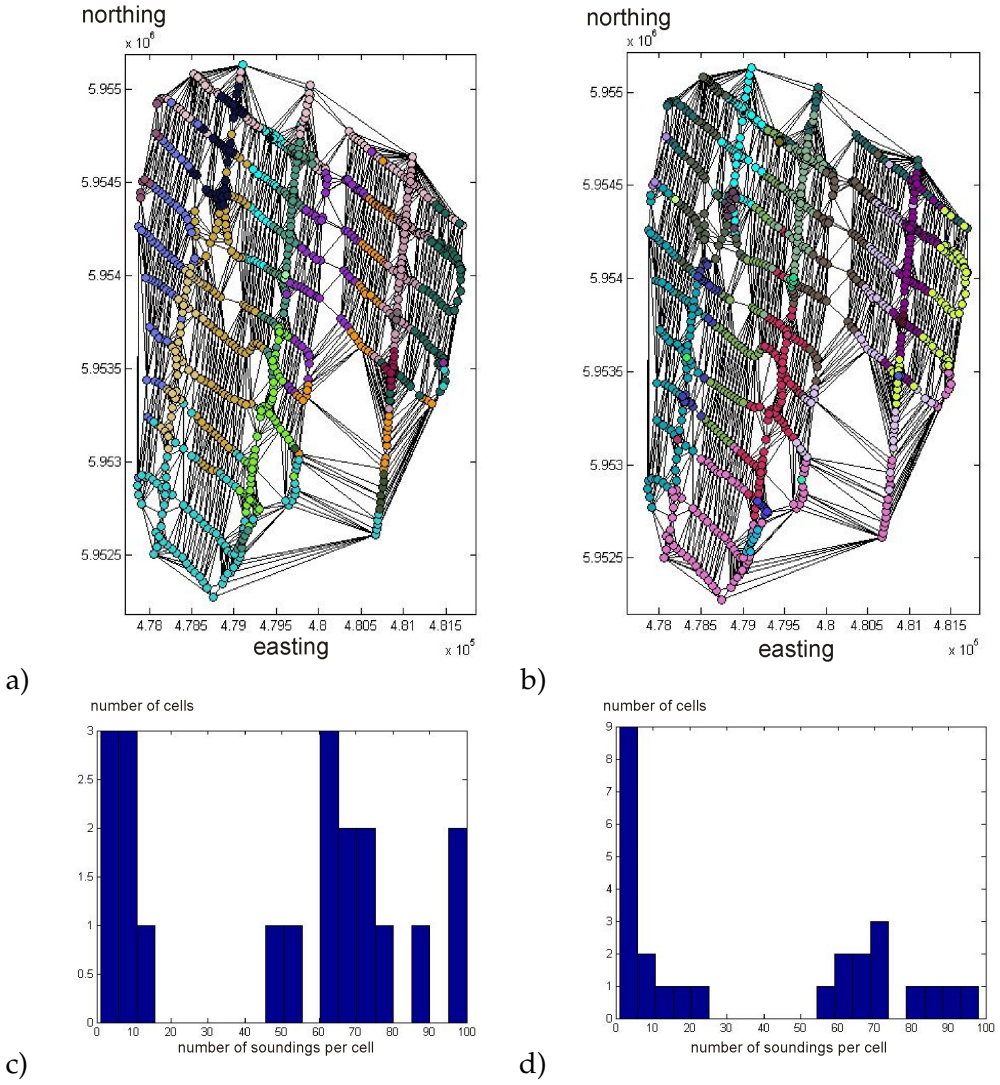

Figure 5.3: *Arrangements of the cells for desired cell size = 60 and a) starting point = 1 and b) starting point = 500. The colored circles indicate the survey sites belonging to a particular cell. c) and d) The corresponding histograms show the distribution of the cell sizes. For example indicates the last column of c) that there are two cells with cell sizes of 95–100 soundings.*

5.2.3 Starting model and SCI settings

The inversion results strongly depend on the used starting model and SCI settings, particularly on the strengths of the constraints $C_{SCI}(d)$, which depend on the reference distance d_{ref}, the reference constraints c_{ref}, and the weighting factor a according to Equation 3.24.

Reference 4-layer starting model

In order to investigate the influence of these settings, calculations with a reference starting model were carried out systematically. The reference model, based on the geological and geophysical information (Chapter 4), should be as simple as possible to evaluate the effects of the SCI parameters to be investigated. Therefore, I defined a 4-layer model with medium constraints.

In Table 5.1 the required parameters and the used values are listed. In this case models with a separation of 40 m were allowed to vary 20% in resistivities and 40%, 20%, and 10% in the first, second, and third layer depths, respectively. No *a priori* information on resistivities were used, this means that no parameters were fixed in the inversion. No lateral constraints on the altitude and no vertical constraints on the resistivities were used.

Meaning	Symbol	Value
Number of layers	n	4
Resistivities in Ωm	ρ_i	[40 20 40 10]
A priori on resistivities		[-1 -1 -1 -1]
Vertical constraints on resistivities		[9.9e9 9.9e9 9.9e9]
Lateral constraints on the altitude		9.9e9
Thicknesses in m	thk_i	[40 30 100]
A priori on thicknesses		[-1 -1 -1]
Depths in m	$depth_i$	[40 70 170]
Reference distance in m	d_{ref}	40
Reference constraints on resistivities	c_{ref,ρ_i}	[1.2 1.2 1.2 1.2]
Reference constraints on depths	c_{ref,d_i}	[1.4 1.2 1.1]
Weight for constraints	a	1

Table 5.1: *Required SCI parameters and values used for the reference starting model for SkyTEM inversion. A model parameter is free if set to -1 and unconstrained if set to 9.9e9.*

The range of 10% on $depth_3$ is consistent with a seismic section (Figure 4.5) which implies an estimated valley slope of 37° in between depths of 200–300 m. This equals an absolute depth constraint of $c_{ref,d4} = 30$ m.

Influence of the starting model

The user has a strong influence on the course of the inversion by the choice of the starting model. The inversion may end in a local minimum, but not in the global

one (*cf.* Figure 3.1). In Figure 5.4 the VRSs along flight line 35.1 of the SCI results with the geologically related starting model are compared with a homogeneously layered starting model usually used when no prior information is known. The constraints were set for all starting models as described in Table 5.1.

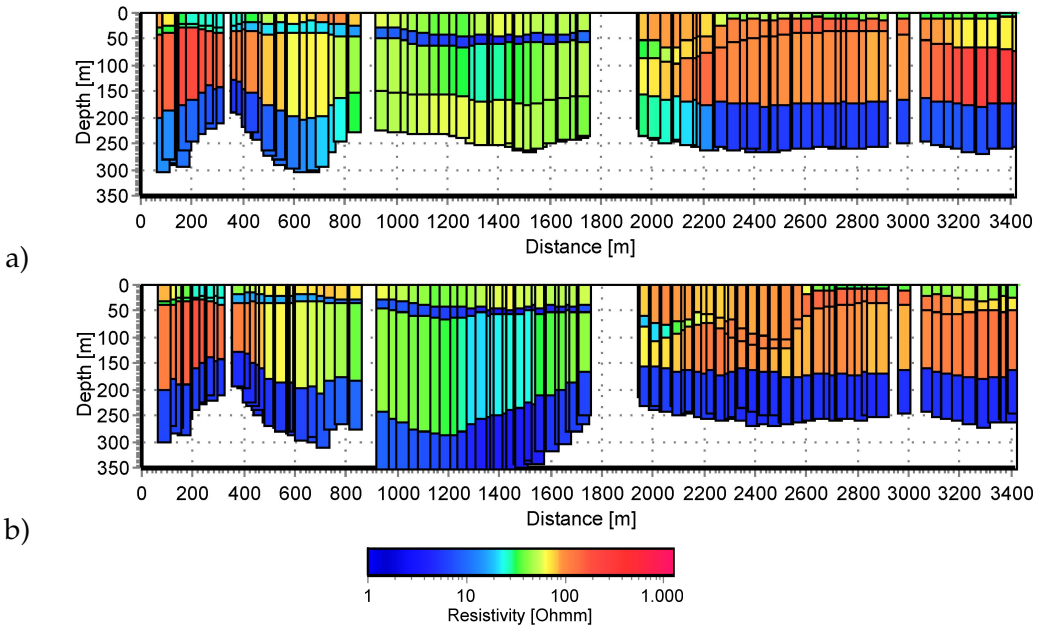

Figure 5.4: *SkyTEM VRSs based on different 4-layer starting models: a) homogeneously layered:* ρ_i *= (50, 50, 50, 50) Ωm,* $depth_i$ *= (40, 70, 170) m and b) based on a priori information:* ρ_i *= (40, 20, 40, 10) Ωm,* $depth_i$ *= (40, 70, 170) m. The constraints were set to:* c_{ref,ρ_i} *= 1.2 and* c_{ref,d_i} *= (1.4, 1.2, 1.1).*

The following features are resolved by both approaches:

1. A conductive layer between 40–60 m inside the valley which could be interpreted as Lauenburg clay.
2. A conductive layer at a nearly constant depth of 170 m east of the valley.
3. West of the valley the depth of the deep conductive layer varies and has a minimum at profile distance 350 m.
4. In the easternmost part a conductive layer occurs at the surface.

If a conductive layer at depth is assumed in the starting model (which is known by the high-moment TEM), then the base of the valley can be exposed (Figure 5.4b).

Influence of subset arrangement

In order to investigate if the subset arrangement, which is derived by a randomly chosen starting point for the triangulation and a desired cell size, has an influence on the inversion results, I carried out SCIs with several different starting points and desired cell sizes. The inversions were carried out using the reference starting model (Table 5.1).

Exemplarily, I show in Figure 5.5 three parallel VRSs generated with a desired cell size of 60, starting point = 1 on the left hand side and starting point = 500 on the right hand side. It is obvious that the influence of the different subset arrangement has only a small influence on the inversion results along the selected VRSs, *e.g.*, the relative conductive cover layer east of the valley differs marginally.

The average resistivity maps for three different depth ranges in Figure 5.6 give an overview of the entire Wanhöden survey area. The maps in the top row were generated with starting point = 1 and the maps in the bottom row with starting point = 500. As the VRSs, the average resistivity maps demonstrate that just artifacts resulting from the extrapolation may occur, *e.g.*, the areas surrounded by the blue circle.

Influence of constraints strengths

In principle the constraints should reflect the expected variations in the geological model. In practice the strengths of the constraints are obtained empirically by model recognition analysis and trial and error fine tuning.

I investigated the influence of the constraints strengths systematically and demonstrate as an example the behavior of the models for doubling and halving the constraints strengths on the resistivities of the reference model. Figure 5.7 shows the VRS of flight line 35.1. In the red surrounded areas it becomes clear that for the stronger constraints on the resistivities, *e.g.*, 10% at Figure 5.7c, the resistivity models are smoother than for the weaker constraints as 40% at Figure 5.7a. Additional, the slope of the valley is smoothed and the valley depth appears shallower.

The influence of the constraints strengths is not as visible in the resistivity maps (Figure 5.8) as in the VRSs, because the maps are the result of an averaging. The red surrounded areas show that for weaker constraints (Figure 5.8a) the maps are less smooth than for stronger constraints (Figure 5.8c).

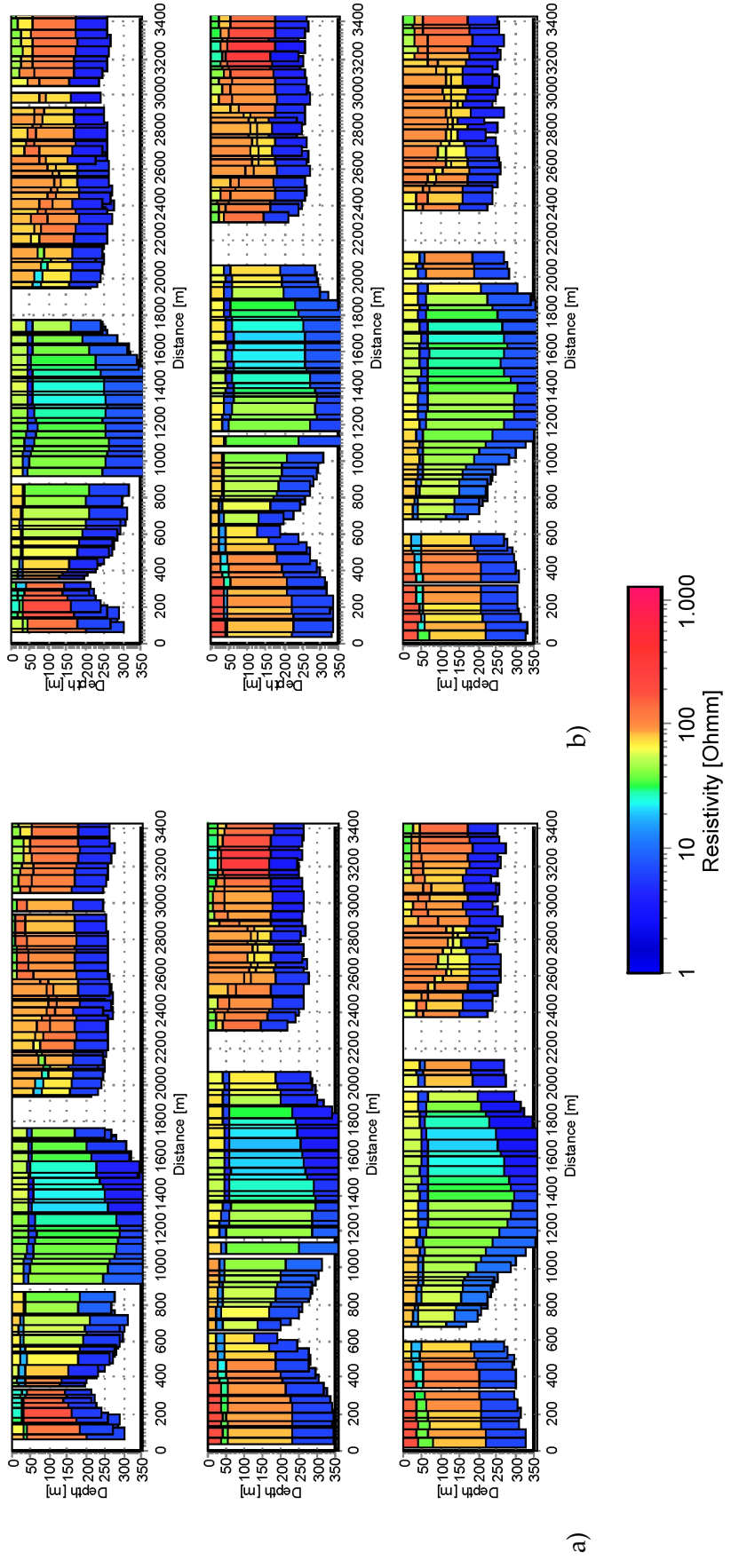

Figure 5.5: *SCI SkyTEM: three parallel VRSs with different subset arrangements. The triangulation settings were a) starting point = 1 and b) starting point = 500 and the desired cell sizes were 60 for both.*

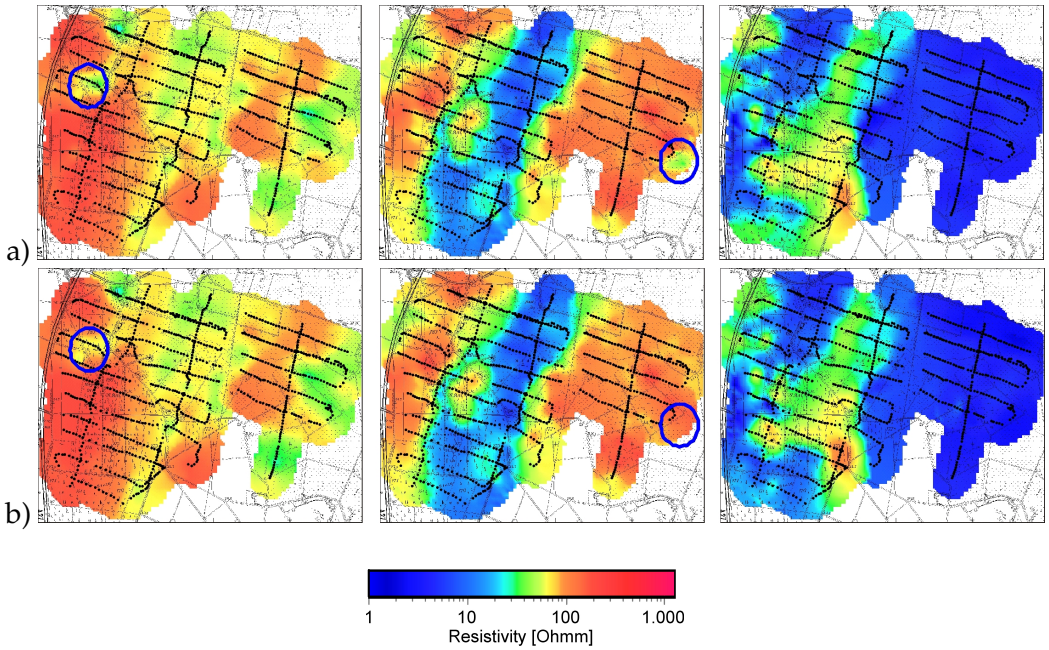

Figure 5.6: *SkyTEM average resistivity maps in 0–20 m, 60–80 m, and 200–250 m for a desired cell size of 60 and a) starting point = 1 and b) starting point = 500.*

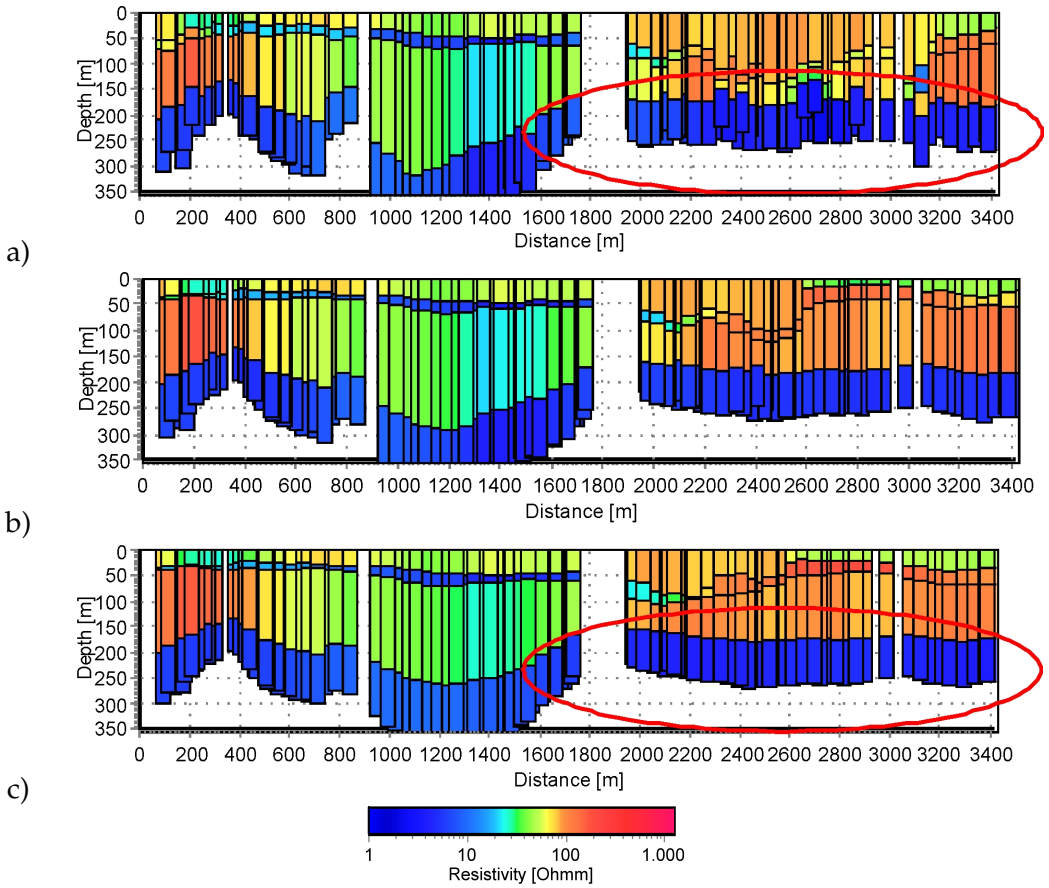

Figure 5.7: *SkyTEM VRS for different strengths of constraints: a) c_{ref,ρ_i} = 1.4, b) c_{ref,ρ_i} = 1.2, and c) c_{ref,ρ_i} = 1.1.*

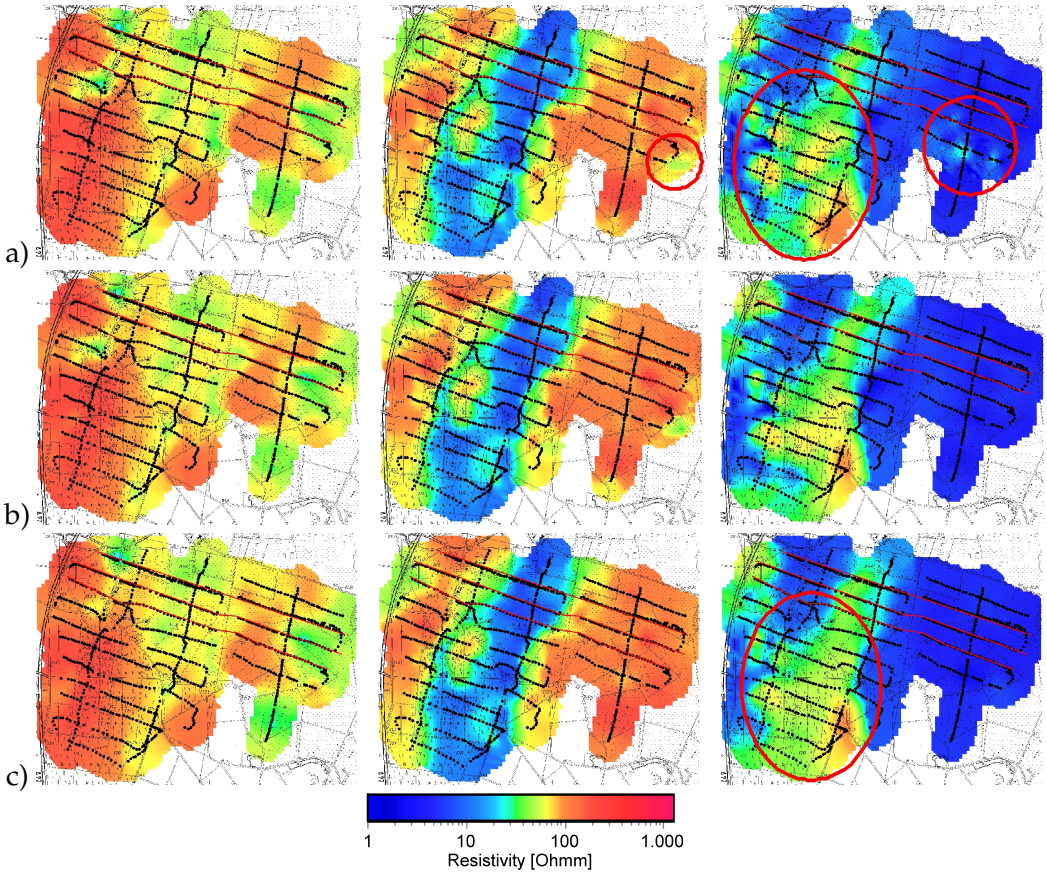

Figure 5.8: *SkyTEM average resistivity maps in 0–20 m, 60–80 m, and 200–250 m for different strengths of constraints: a) c_{ref,ρ_i} = 1.4, b) c_{ref,ρ_i} = 1.2, and c) c_{ref,ρ_i} = 1.1.*

Influence of constraints weighting

The strength of the reference constraints c_{ref} is related to the reference distance d_{ref} which has to be set to the medium distance between the survey sites, *i.e.*, 40 m for the Wanhöden SkyTEM-survey. For nearer or farther sites the exponent a defines the weight of the reference constraints depending on the distance. $a = 1$ defines a linear , $a = 2$ a square, and $a = 0.5$ a square-root dependency (see Table 5.2).

C_{SCI}	d [m]	10	20	40	80	160
linear	a=1	1.05	1.1	1.2	1.4	1.8
square	a=2	1.00125	1.05	1.2	1.8	4.2
square root	a=0.5	1.1	1.14	1.2	1.28	1.4

Table 5.2: *Influence of the exponent a on the strengths of constraints C_{SCI} at different distances d for a reference distance of $d_{ref} = 40$ m and a reference constraint of $c_{ref} = 1.2$.*

The influence of the weighting is less apparent in the VRS at line 35.1 (Figure 5.9) than in the resistivity maps (Figure 5.10). By using a square dependency of the distance the model parameters of the nearer sites have a stronger influence compared to the linear weighting and the farther sites a weaker influence.

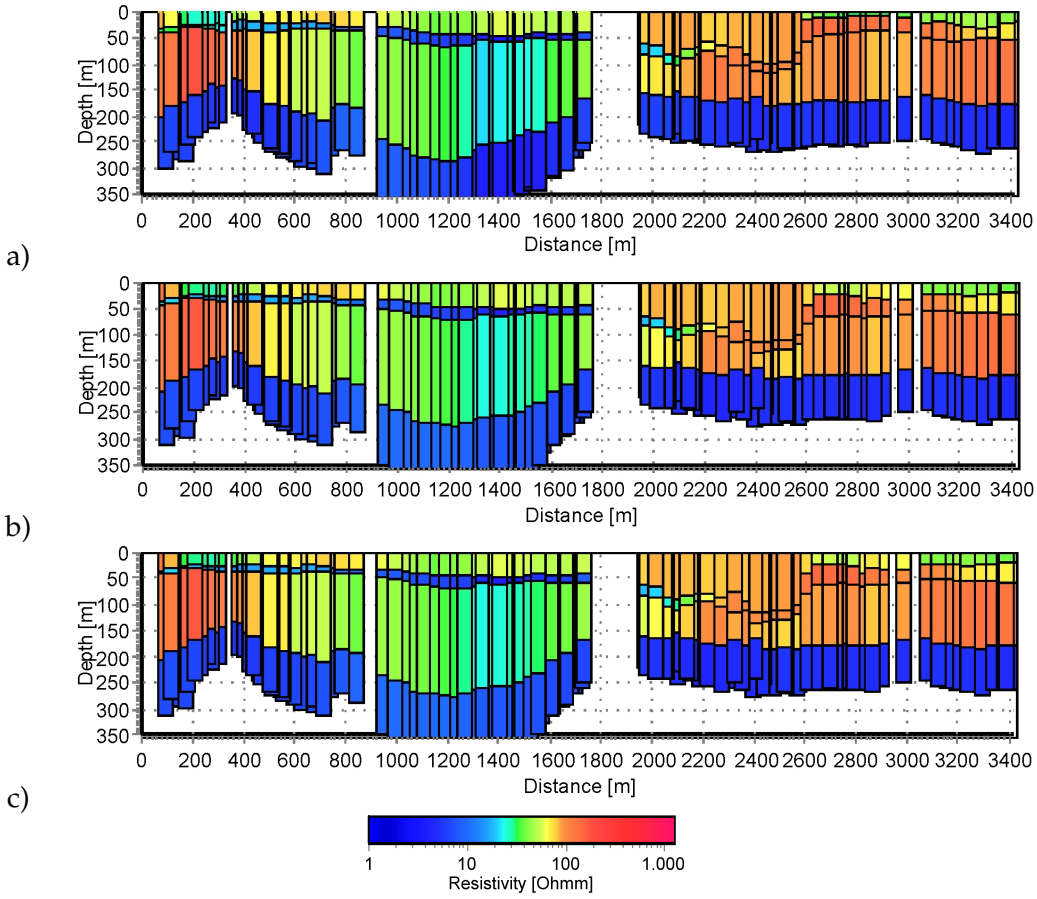

Figure 5.9: *SkyTEM VRS at line 35.1 for different weightings of constraints: a) a = 1, b) a = 2, and c) a = 0.5.*

Applying a square root weighting, also the farther sites have a relative strong influence resulting in smoother models, which is pointed out at the surrounded areas of Figure 5.10c.

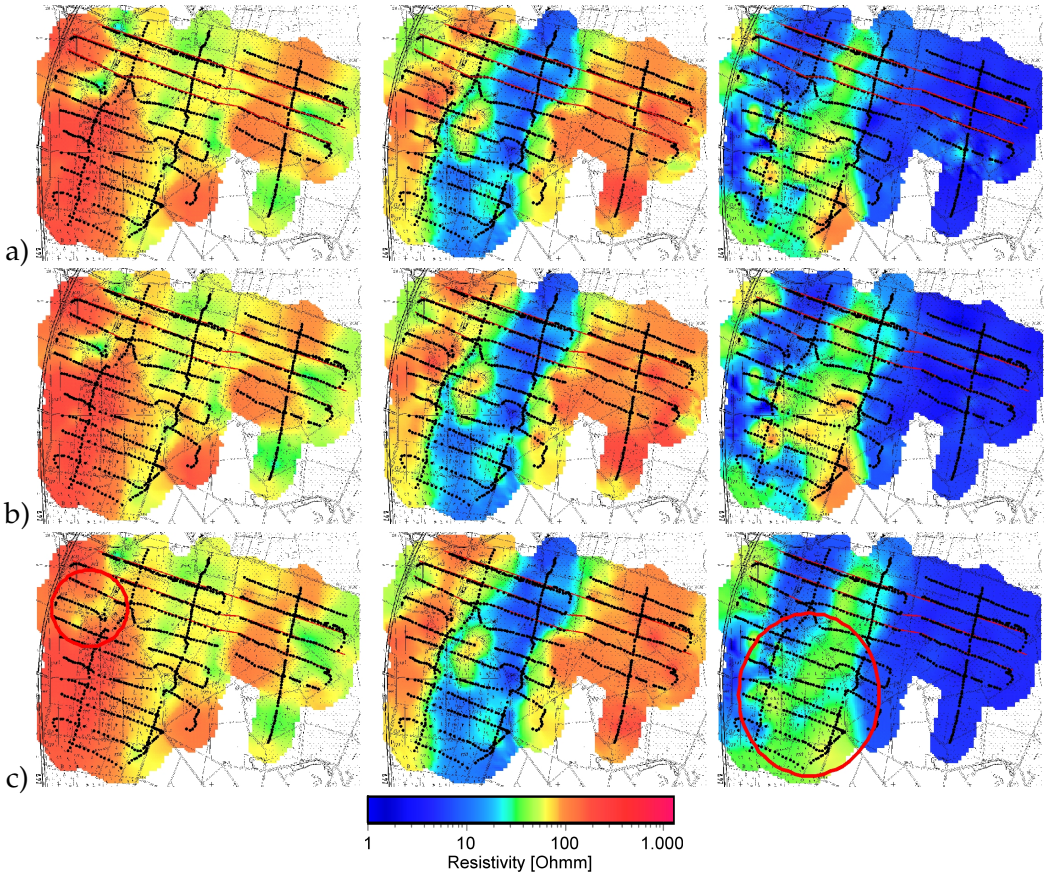

Figure 5.10: *SkyTEM average resistivity maps in 0–20 m, 60–80 m, and 200–250 m for different weightings of constraints: a) a = 1, b) a = 2, and c) a = 0.5.*

5.2.4 SCI and single-site 1D inversion

In Figure 5.11 I demonstrate the difference between the best single-site 1D inversion result of the SkyTEM data, obtained by considering the residuals and the STDFs, and the SCI result obtained using the reference 4-layer starting model which considers geophysical information for the definition of the model parameters and the constraints.

The advantage of the SCI becomes apparent in the VRSs. Here, especially the interface to the Tertiary clay can be modeled smoothly. The most important advantage is that the base of the Cuxhaven valley can be revealed. This interface is poorly resolved by single-site 1D inversion because of the limited investigation depth caused by the thick conductive Lauenburg clays.

In the resistivity maps (Figure 5.11) the difference between SCI and single-site 1D inversion becomes barely apparent. As noted above, the maps are the product of an averaging procedure.

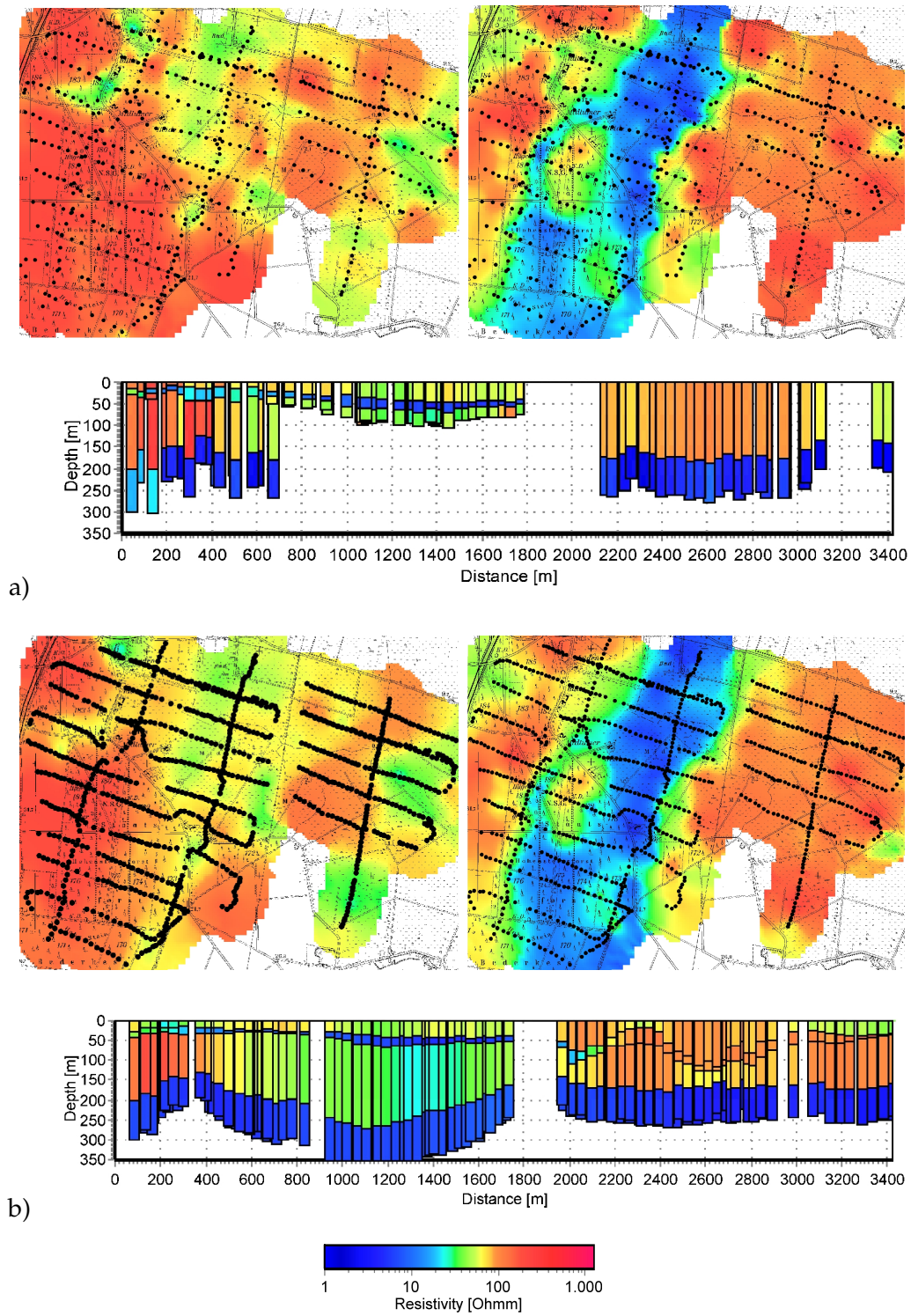

Figure 5.11: *SkyTEM average resistivity maps in 0–20 m and 40–60 m and the VRS at line 35.1 for inversions a) without constraints and b) with constraints as defined in Table 5.1.*

5.2.5 Standard deviation factors of the SCI results

As for single-site inversions also for the SCI STDFs can be calculated. Figure 5.12 shows STDFs of two interesting model parameters of the 4-layer reference model. The resistivity of the fourth layer (Tertiary clay) as well as the interface between third and fourth layer are well resolved in the entire survey area.

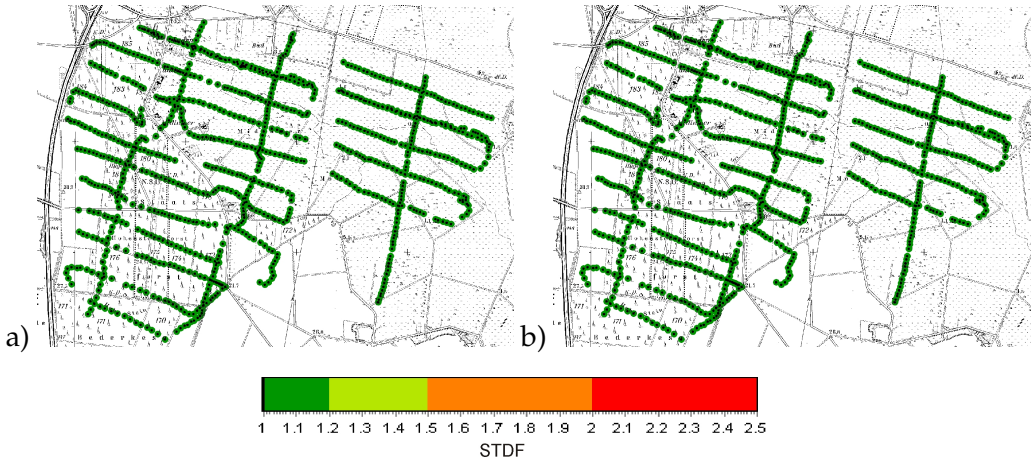

Figure 5.12: *SkyTEM SCI: STDFs of a) ρ_4 and b) $depth_3$. The resistivity of the fourth layer (Tertiary clay) and the interface between third and fourth layer is well resolved in the entire survey area.*

If a resulting model parameter matches the requirement of the constraint, it is per definition well resolved. Therefore, the STDFs can not be used to differentiate if a model parameter is the result of the constraints or of the information in the data.

5.2.6 Increasing the number of layers

With the studies on the reference 4-layer model the influence of the various SCI parameters could be demonstrated. Being on *the search for a more useful model* I try to approach reality by increasing the number of layers in the following. The basis for the starting model is again the lithological log HL9 (Figure 4.3). Here, we see that the Lauenburg complex consists of two clay blocks. The first one between 40–70 m that I considered in the 4-layer model, and a second one between 115–145 m. This one I added to the 4-layer reference model and got a 6-layer starting model.

The result of the 6-layer SCI is shown on six VRSs in Figure 5.13. The locations of the VRSs are indicated with red lines at Figure 5.14.

With this 6-layer starting model an additional conductive layer of about 20 Ωm (the missing one which is known by the lithological log) can be modeled inside the valley between 100–150 m depth. This layer fades out to the west of the valley and is not visible east of the valley. It is less conductive than the upper Lauenburg clay and the Tertiary clay below. Due to the fact that this layer does not appear east of the valley, I suggest that it is not just an artificial product of the constraints.

If no other duties call, you may iterate the process of enhancing your model for a long time. But is that useful? We should not forget, however, that we are *searching*

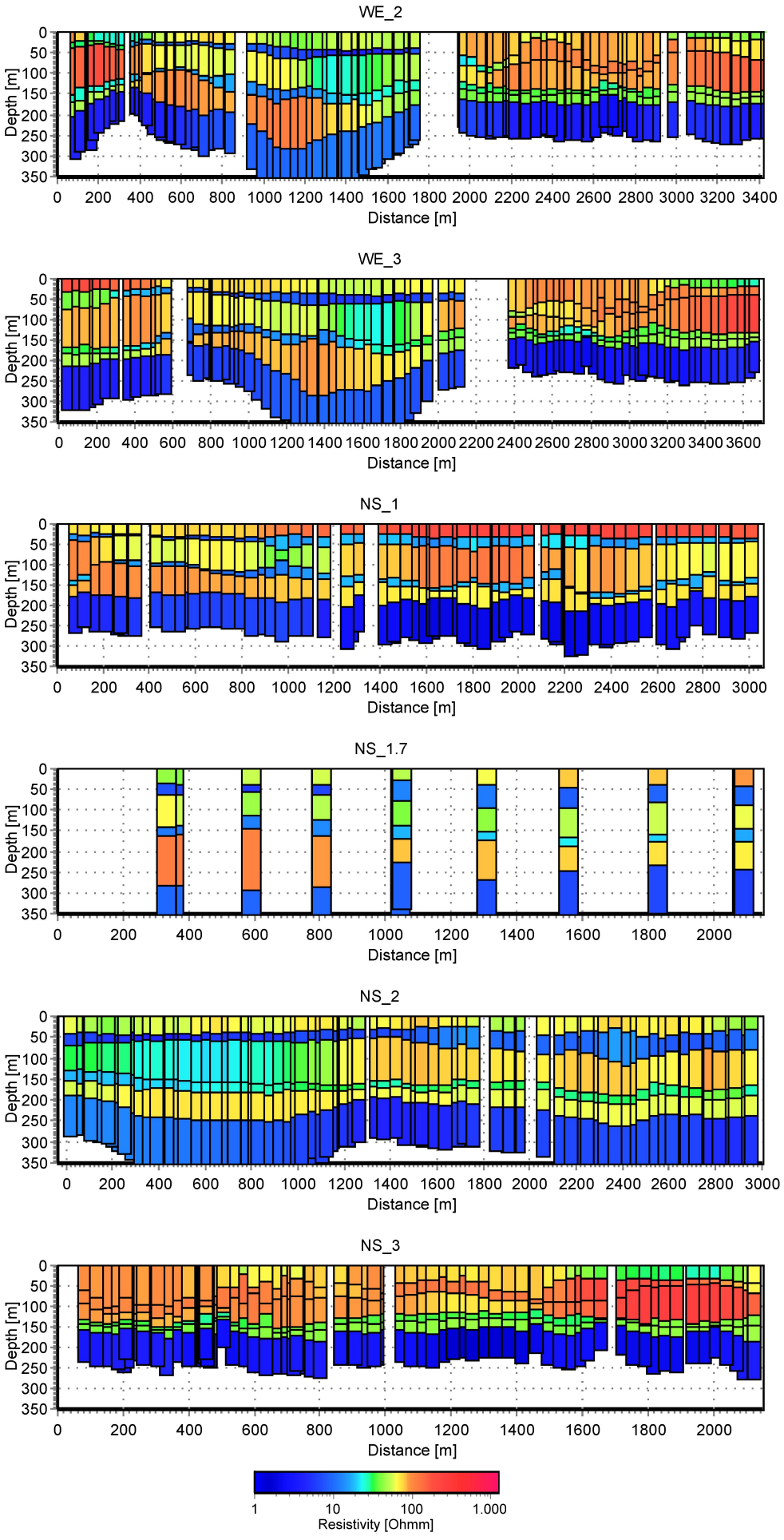

Figure 5.13: *SkyTEM VRSs of a 6-layer case. The locations are show at Figure 5.14.*

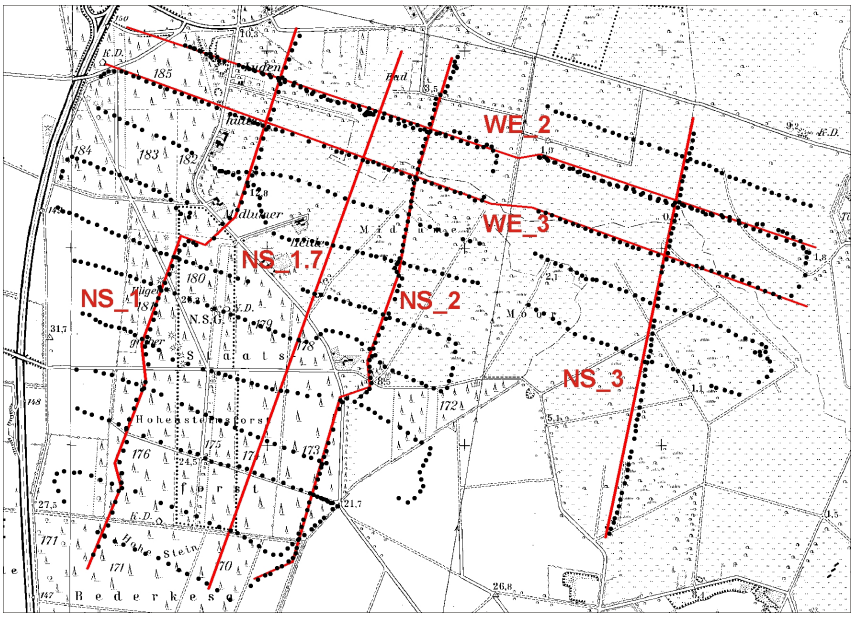

Figure 5.14: *Location map of the VRSs used for the 6-layer SCI.*

for a useful model and therefore we have to find it in a reasonable time. In this case I have a data set of more than thousand soundings, so this is impractical.

For hydrogeological questions, such as groundwater protection, the modeling with 6 layers is more useful than with 4 layers, because we probably get a more realistic cumulative clay thickness of the upper 150 m depth. The lower resistive third layer of the single-site inversion result (Figure 5.11a) inside the valley suggests a higher clay content (30 Ωm) than outside the valley (100 Ωm). Nevertheless, this information is not used in the calculation of the cumulative clay thickness, which considers resistivities below 30 Ωm only. In the 6-layer case, a layer with a medium resistivity of about 20 Ωm is revealed inside the valley, which contributes to the cumulative clay thickness.

5.3 Adaption for HEM data

I followed *Viezzoli et al.* [2008] and adapted the concept of the SCI to the HEM method.

5.3.1 Delaunay triangulation of HEM data

The data density of HEM measurements along the flight lines (about 4 m site spacing) is much higher than between lines (about 250 m line spacing). To reduce the data quantity I used every 10th dataset.

The plots and the explicit peaks in the histogram of the Delauny triangulation (Figure 5.15) show that the HEM sites distribution is more uniform than the distribution of the SkyTEM sites (Figure 5.2). As expected, the peak of the most frequent site spacings is at 40 m and the line-spacing peak at 250 m.

5.3.2 Starting model and SCI settings

Reference 5-layer starting model

Similar to the SkyTEM SCI I defined a reference starting model for the HEM SCI (Table 5.3), which is based on *a priori* information of the lithological log (Figure 4.3).

Meaning	Symbol	Value
Number of layers	n	5
Resistivities in Ωm	ρ_i	[40 20 40 20 40]
A priori on resistivities		[-1 -1 -1 -1 -1]
Vertical constraints on resistivities		[9.9e9 9.9e9 9.9e9 9.9e9]
Lateral constraints on the altitude		9.9e9
Thicknesses in m	thk_i	[15 10 15 30]
A priori on thicknesses		[-1 -1 -1 -1]
Depths in m	$depth_i$	[15 25 40 70]
Reference distance in m	d_{ref}	40
Reference constraints on resistivities	c_{ref,ρ_i}	[1.4 1.4 1.4 1.4 1.4]
Reference constraints on thicknesses	c_{ref,t_i}	[1.3 1.2 1.15 1.1]
Weight for constraints	a	1

Table 5.3: *Required SCI parameters and values used for the reference starting model for HEM inversion. A model parameter is free if set to -1 and unconstrained if set to 9.9e9.*

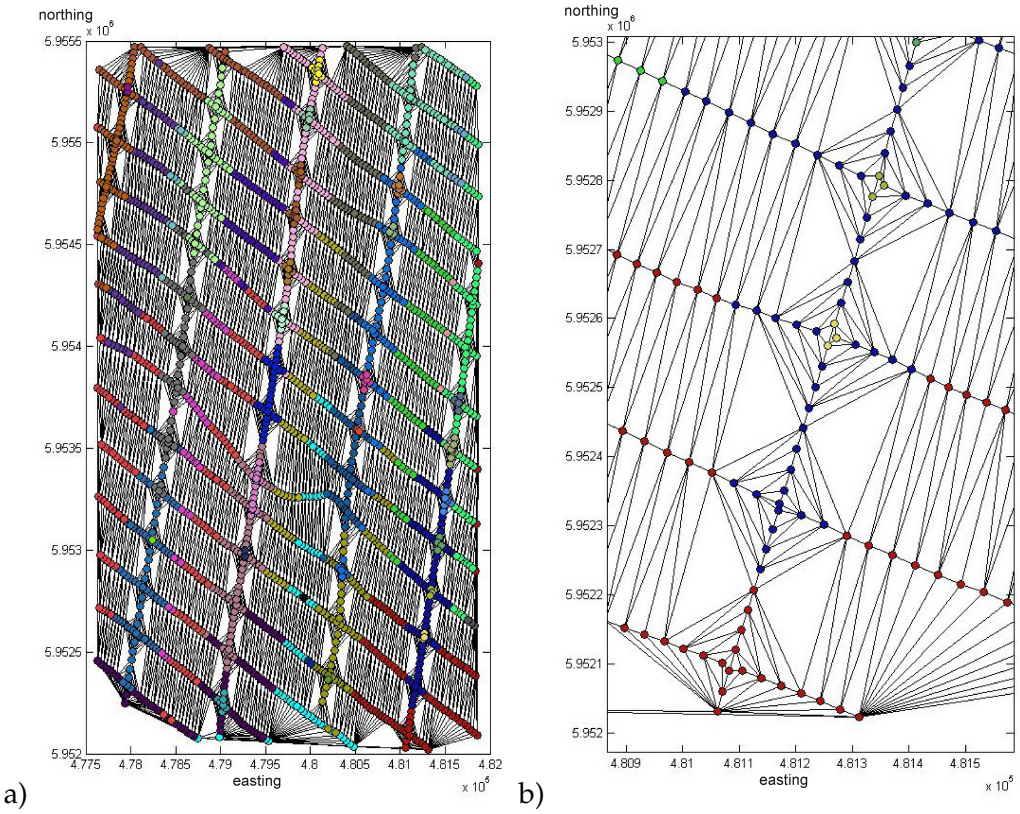

Figure 5.15: *a) Delaunay triangulation with subsets of the HEM sites in the Wanhöden survey area. The colored circles indicate the survey sites belonging to a particular subset. b) The close-up demonstrates uniformity of the HEM sites distribution. c) Histogram of the distances between nearest neighbors soundings.*

Influence of the starting model

In Figure 5.16 the results of the SCI for different starting models are shown. I got the best results with a layered model, 40% constraints on the resistivities, and decreasing constraints from 30–10% on the thicknesses (Figure 5.16b). Stronger constraints for greater depths are useful due to the reduced resolution of the model parameters at depth.

The resolution of the shallow clay at about 20 m was nearly independent of the starting model. This is not the case for the single-site inversion (Figure 4.10), where the shallow clay sometimes was suppressed. SCI also enables to model the base of the Lauenburg clays.

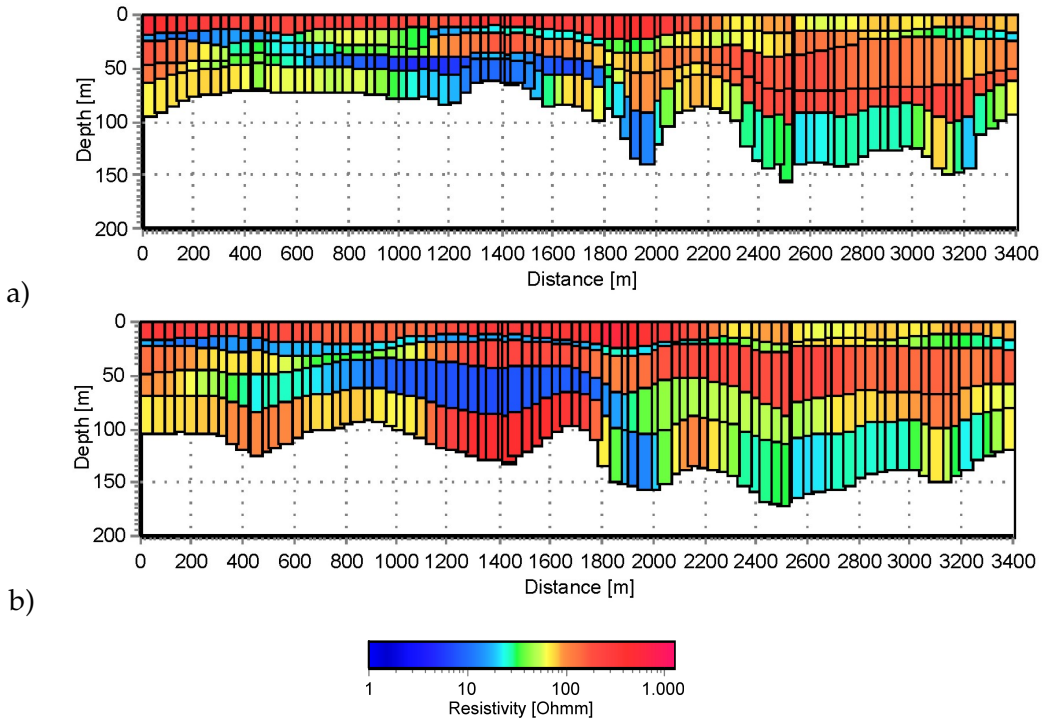

Figure 5.16: *HEM VRSs at line 35.1 obtained by SCI using different starting models: a)* ρ_i *= (40, 40, 40, 40, 40)* Ωm*,* thk_i *= (10, 10, 10, 10) m,* $c_{ref,\rho_i} = 1.8$*,* $c_{ref,t_i} = 1.2$ *and b)* ρ_i *= (40, 20, 40, 20, 40)* Ωm*,* thk_i *= (15, 10, 15, 30) m,* $c_{ref,\rho_i} = 1.4$*,* c_{ref,t_i} *= (1.3, 1.2, 1.15, 1.1).*

Influence of the constraints strengths

As for the SCI on SkyTEM data, I investigated the behavior of the models for doubling and halving the constraints strengths on the resistivities of the reference model for SCI on HEM data. The results are shown in Figure 5.17. The differences are marginal.

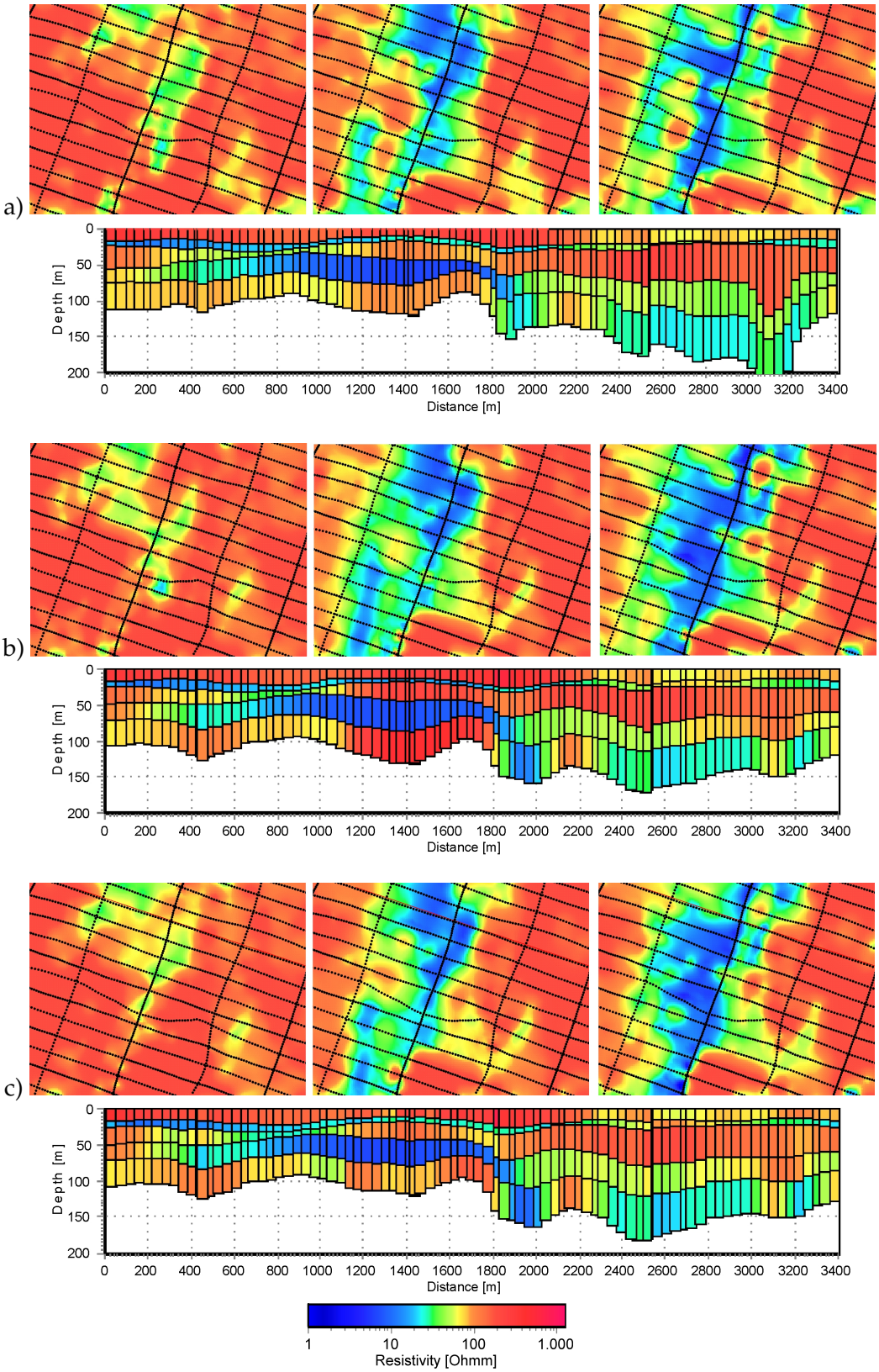

Figure 5.17: *HEM average resistivity maps in 0–20 m, 40–60 m, and 60–80 m; and HEM VRSs for different constraints strengths: a) c_{ref,ρ_i}= 1.8, b) c_{ref,ρ_i}= 1.4, and c) c_{ref,ρ_i}= 1.2.*

5.3.3 SCI and single-site 1D inversion

In Figure 5.18 the SCI (Figure 5.18b) results using constraints parameters as defined in Table 5.3 are compared to the single-site inversion results (Figure 5.18a). The averaged resistivity map is, as expected, smoother for the SCI between 20–40 m. Between 40–60 m this does not seem not to be the case, because the base of the Lauenburg clay is not resolved with single-site 1D inversion. As a result, the map is distorted.

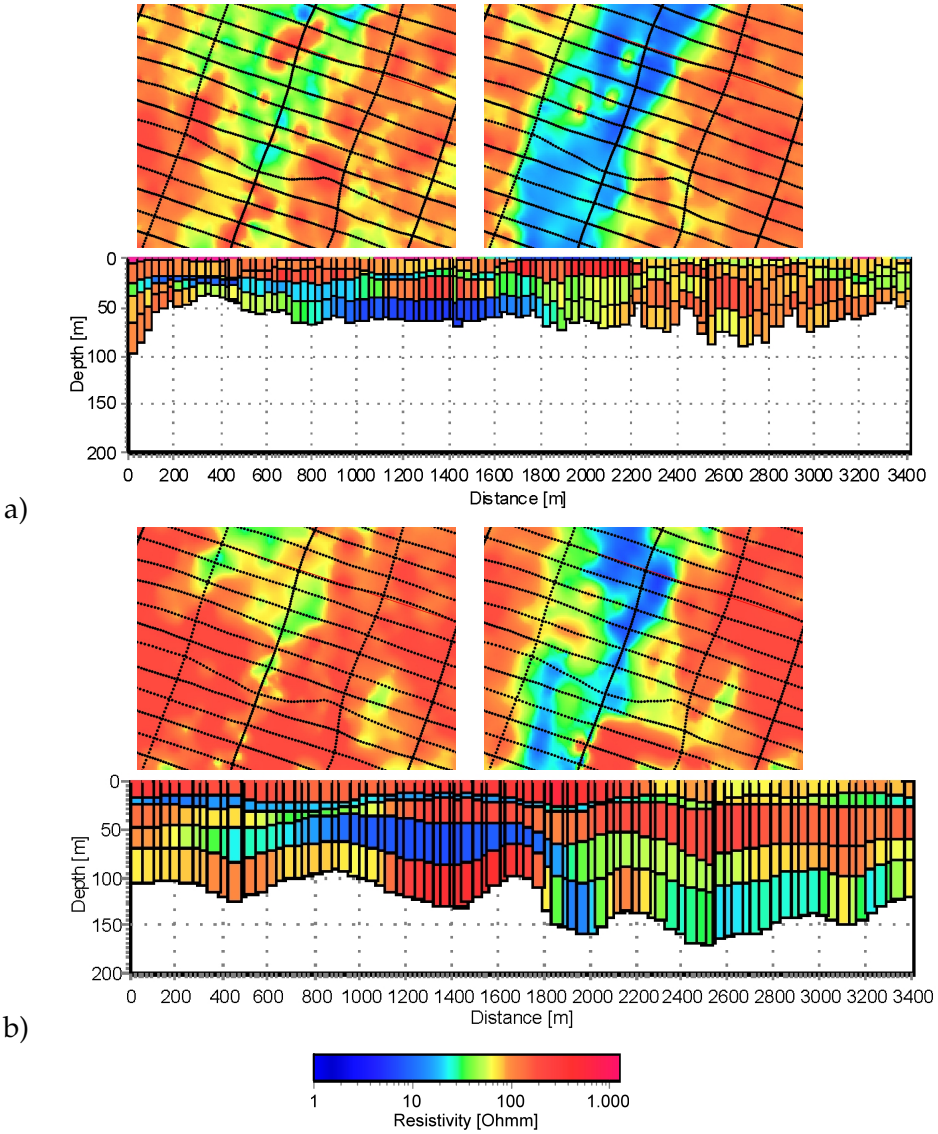

Figure 5.18: *HEM average resistivity maps in 20–40 m (left) and 40–60 m depth (right) and the VRS at line 35.1 for inversions a) without constraints and b) with constraints.*

HEM single-site inversions generally result in acceptable models if variable starting models are used, which are automatically generated from apparent resistivities and centroid depths. Nevertheless, the shallow clay sometimes was suppressed. With SCI the dependency on the starting model decreases and the base of the Lauenburg clay could be modeled.

5.4 Conclusion

Systematic studies of the SCI parameters showed that by strengthen the constraints smoother inversion models can be achieved. To avoid misinterpretations it is important to consider the geological variability and *a priori* information, if available. In comparison to single-site inversion the inversion results applying SCI are less dependent on the starting model.

SCI is particularly useful for large data sets as obtained in AEM and allows to resolve layers which are locally poorly resolved, such as the base of the valley for SkyTEM or the base of the Lauenburg clay for HEM.

An open question is if the shape of the valley, especially the valley slopes, was modeled correct by using SCI or if the shape was caused by the constraints. A 3D modeling study helps to answer this question.

Chapter 6

3D Modeling of a Buried Valley

6.1 Introduction

The interpretations of the TEM and HEM data in the previous sections were based on layered earth models. The question is up to what kind of lateral inhomogeneity a multidimensional earth can be regarded as quasi one-dimensional model. In this context, we should always keep in mind the words of *Box* [1979]: *"All models are wrong, some are useful."* The aim of geophysical modeling is to find the most useful models explaining the subsurface sufficiently. The influence of multidimensional structures on 1D inversions of HEM data is demonstrated by *Sengpiel and Siemon* [1998] for several examples. In this chapter I analyze, exemplary for TEM, the influence of a valley structure on 1D inversions. Furthermore, I investigate how the application of constraints influence the inversion results.

6.2 The Forward Code

For the 3D modeling of the TEM data I used the finite differences code *sldmem3* of *Druskin and Knizhnerman* [1988]. As conventional time-stepping algorithms can be very time consuming for large scale 3D problems, the *spectral Lanczos decomposition method* (SLDM) is used to solve the differential equations. The computation of direct current, time-, and frequency-domain fields for any source configurations is provided.

The theory of the SLDM can be found in *Druskin and Knizhnerman* [1988].

6.3 TEM Modeling

6.3.1 The construction of the grid

The convergence of the algorithm strongly depends on the appropriate construction of the grid. For the design of the grid spacings the diffusion depth d_{dif} can be

used. *Hördt et al.* [1992] recommend $3/d_{dif}$ as value for the minimum grid spacing and $3 \times d_{dif}$ as maximum grid spacing. The grid spacing should be small at boundaries to conductors and around the transmitter, and increase in- and outwards. Over-discretization slows down the convergence significantly.

In Figure 6.1 a part of the final grid for a 100×100 m^2 transmitter is shown. It was constructed using a grid generator with the upper thumb rules for the minimum and maximum grid spacings. In the z-direction I inserted additional grid lines at the layer boundaries. In the x- and y- directions the grid has 80 grid lines, in the z-direction it has 65 grid lines. The whole grid is 16 km wide and 8 km deep.

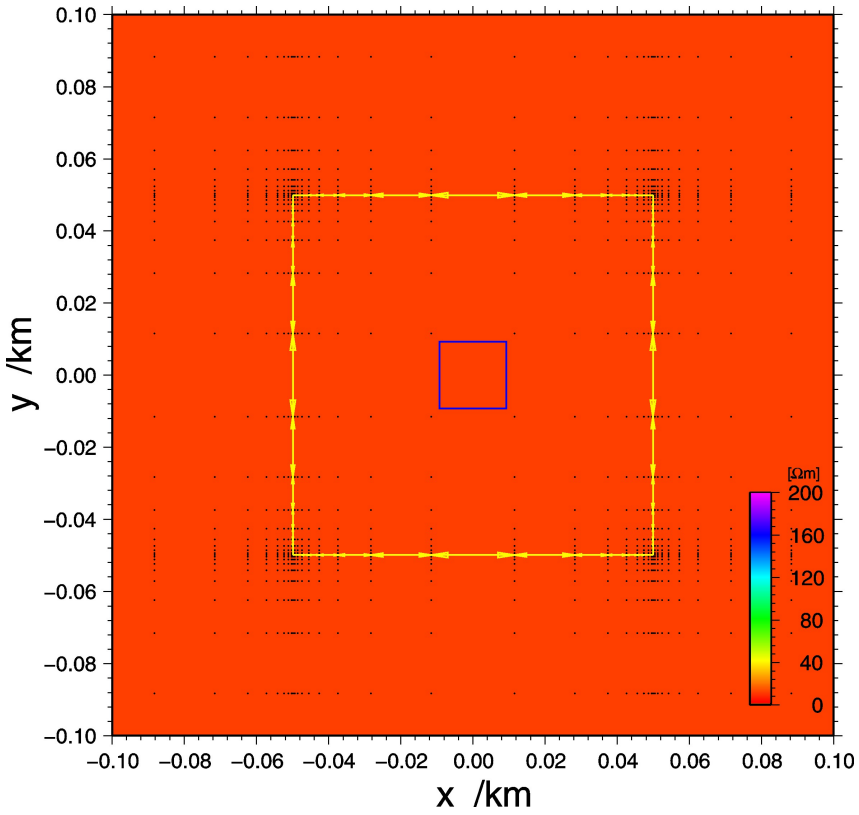

Figure 6.1: *Grid in x/y plane. The grid spacing is narrow around the transmitter loop (yellow rectangle) and increases in- and outward. The receiver loop (blue rectangle) is located at the origin, the center of the transmitter loop.*

6.3.2 The definition of the transmitter and the receiver

The positions of transmitter and receiver are related to the grid, therefore the transmitter was constructed by 68 electrical dipoles stitched together to a rectangular loop (see Figure 6.1). A magnetic receiver is located in the center of the grid and oriented in the z-direction.

6.3.3 Validation of the grid

First, the constructed grid is validated for a homogeneous half-space of the lowest and the highest resistivity of the model used for the study against a 1D forward code. Figure 6.2 shows the comparison of the model data calculated with *sldmem3* and *em1dinv* [*HGG*, 2007*b*].

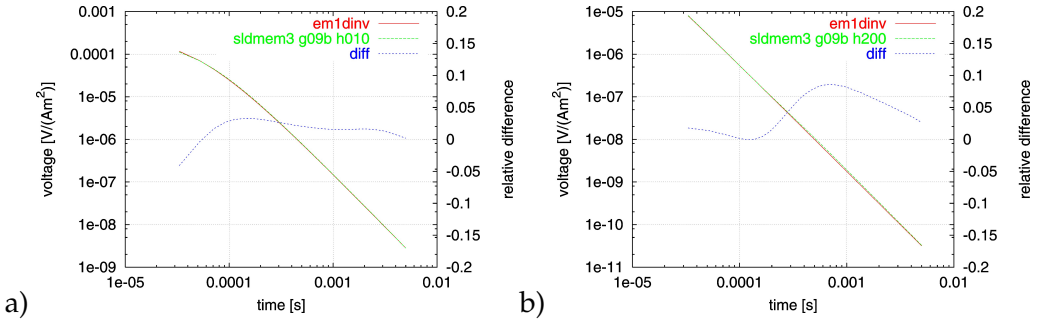

Figure 6.2: *Model data calculated with sldmem3 and the 1D code em1dinv. a) Homogeneous half-space with 10 Ωm and b) homogeneous half-space with 200 Ωm.*

I calculated the transients for time ranges of 15-5,000 μs, that is the range, where the *PROTEM 47* data have a data uncertainty of less than 10%.

The relative difference of the voltages U_i, $diff = \frac{U_1 - U_2}{U_1}$, results in values mostly below 5%, which are small enough. Only at medium times the relative difference for the 200 Ωm homogeneous half-space model data is over 5% (Figure 6.2b). As I use a thin cover layer with 200 Ωm in the model study, this difference is acceptable.

A second test of the grid should show that the grid is suited for the occurring resistivity contrasts. In *sldmem3* anomalies are described by conductive blocks, a layering by very long blocks.

The 5-layer model and the model data of *sldmem3* and *em1dinv* are shown in Figure 6.3. The relative difference below 3% justifies the used grid.

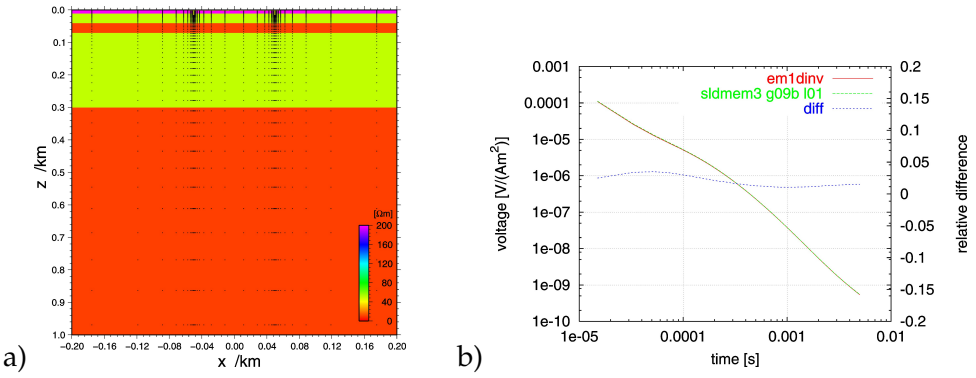

Figure 6.3: *a) 400 m × 1,000 m zoom into the x/z-plane of the 5-layer model with* $\rho_i = (200, 50, 10, 50, 10)$ *Ωm and* $depth_i = (10, 40, 70, 300)$ *m. The grid spacing is narrow at the layer boundaries and around the transmitter loop, and increases in- and outward. b) Comparison of model data derived with sldmem3 and em1dinv.*

6.3.4 3D modeling of 2D valleys

To get an impression of the 2D effects, I modeled valleys with different depths and widths and investigated the effect of the slope angle. The shape of the valleys vary just in the x-direction and strictly speaking these are 2D models. Since I use a 3D code which also calculates the propagation in the y-direction I use the term 3D modeling (applied to 2D valleys). Figure 6.4 shows three examples of them, the valleys 06, 07 and 08.

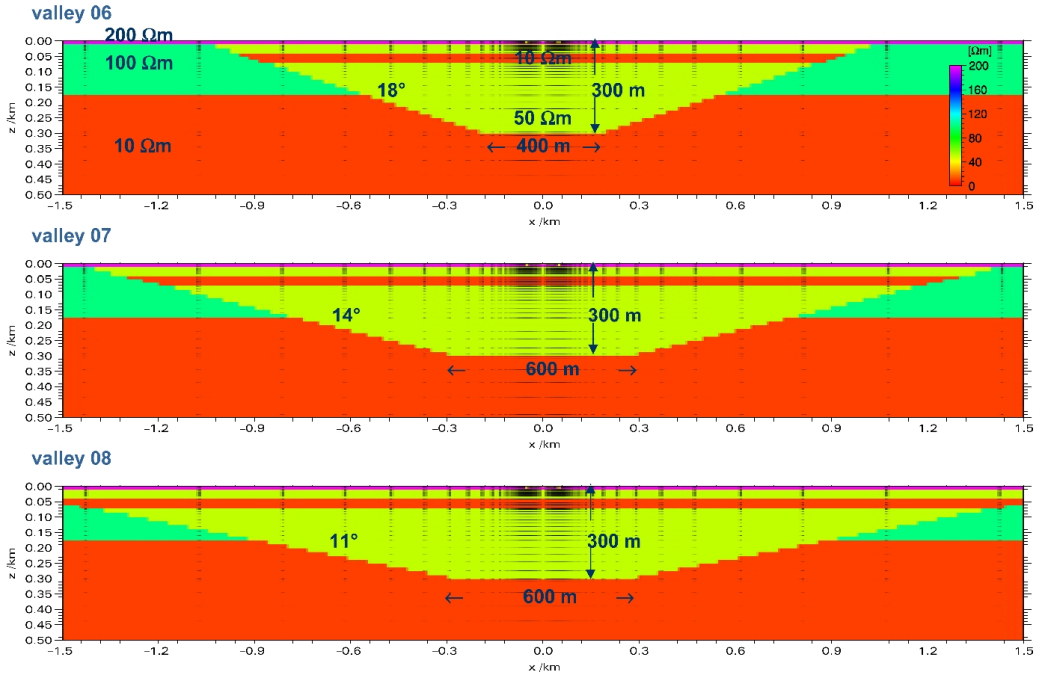

Figure 6.4: *2D models of a buried valley: Valley 06 has a slope angle of 18°. The base of the valley is at 300 m depth and the width of the base is 400 m. Valley 07 and valley 08 differ in the slope angle of 14° and 11°, respectively. Both have a base width of 600 m and a base depth of 300 m.*

Each model consists of 71 conductive blocks. The resistivity distribution of the valleys are equal. A thin resistive 200 Ωm layer at 0–10 m depth covers a valley constructed by 50 Ωm blocks and 10 Ωm blocks between 40–70 m depth. The blocks outside the valley have a resistivity of 100 Ωm between 10–170 m depth and 10 Ωm below.

In Figure 6.5 the model data calculated using *sldmem3* for valley 07 are compared to the model data calculated for the corresponding 5-layer model using the 1D code *em1dinv*. By following Figure 6.5 from a to d, the effect of the slope and the base width gets apparent. The nearer the slope, the slower reduces the transient at late times. This is, because the conductive half-space appears earlier in the data. In the center of the valley (300 m apart the slope) the difference between 1D and 3D model data is minimal (below 3%) (Figure 6.5a). At the beginning of the slope (300 m apart the center), the transients differ clearly (more than 10%) at late times (Figure 6.5d).

For valley 08 with only 11° slope this effect is much smaller as shown at Figure 6.6 for data calculated at the beginning of the slope 300 m apart the center.

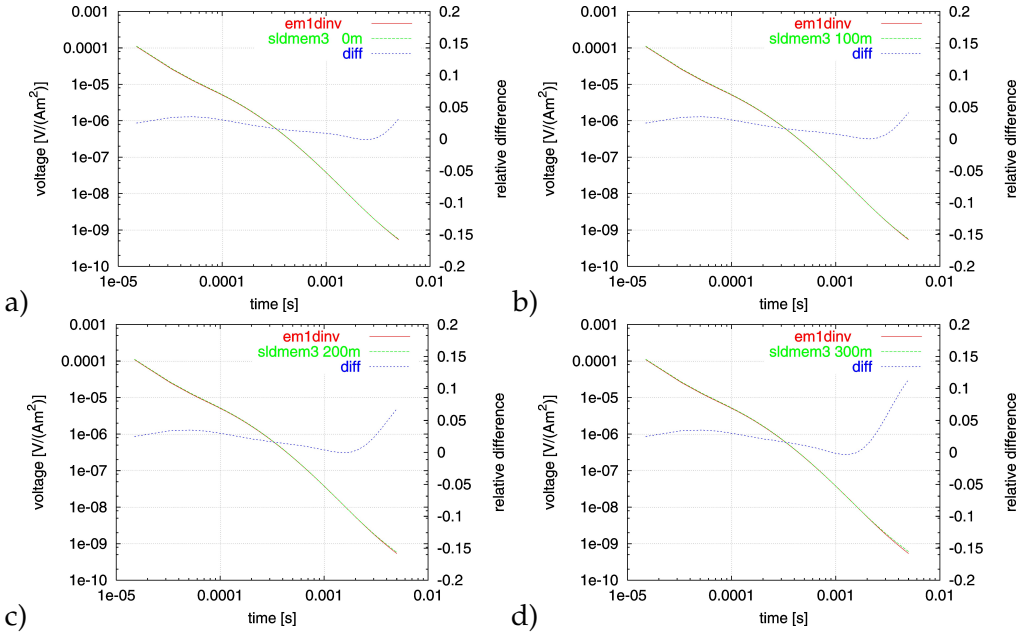

Figure 6.5: *Model data of em1dinv compared with model data of sldmem3: a) at the center of valley 07 and b) – d) 100 m, 200 m and 300 m apart the center.*

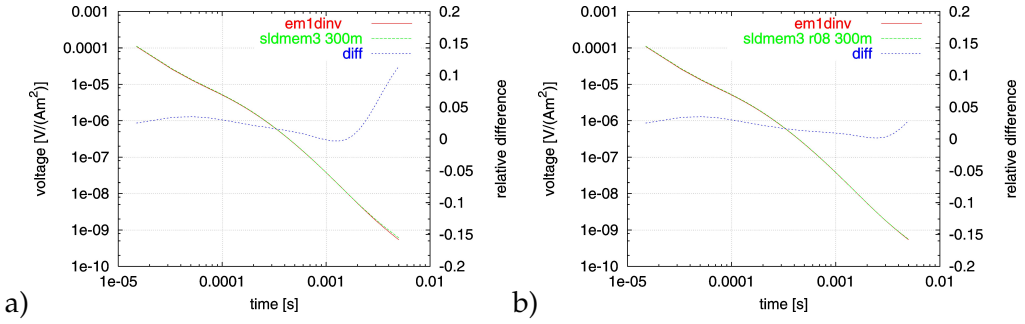

Figure 6.6: *Model data of em1dinv compared with model data of sldmem3: a) 300 m apart the center, at the beginning of the slope, of a) valley 07 with 14° slope angle and b) valley 08 with 11° slope angle.*

Concluding, I want to mention that for shallow slope angels, such as 11°, a 1D assumption is legitimated because the data are only slightly distorted by the slope. The 2D effect in the data is smaller than the data uncertainty, *e.g.*, of the *PROTEM 47* data. If the 2D effect in the data is greater than the data uncertainty, *e.g.*, at a slope angle of 14°, then a 1D assumption is incorrect and the danger of misinterpretations rises.

6.4 Inversion of Synthetic Data

In this section I discuss the validity of the 1D assumption by using 1D inversion codes even though the data are from a 2D resistivity structure. I investigate different valley shapes and show how the use of constraints can improve the inversion result.

6.4.1 Valley 08

Valley 08 has a slope of 11°, the most shallow slope of the regarded three valley models. In Figure 6.7 the 1D inversion results of the synthetic TEM data with different 5-layer starting models are shown as colored bars. The original 2D model is indicated by solid black lines and resistivity values. First, 5-layer models with homogeneous resistivities of 20 Ωm and 50 Ωm, then, the original resistivity distribution at the center were used as starting models. For all stations on the profile the same starting models were used. On the left-hand side the inversions were carried out without any constraints, on the right-hand side the first and/or the fifth resistivity was constrained to 5%. I constrained these model parameters because these are continuous layers.

In the case that the starting model is far from the original model the inversion process ends up in a local minimum like in the middle part of Figure 6.7a. Here, the depth of the underlying half-space is preset to 80 m and the depth of the 10 Ωm half-space at 300 m can not be found. By increasing the depth range to 210 m and using a starting resistivity of 20 Ωm instead of 50 Ωm, the underlying homogeneous half-space of 10 Ωm can be resolved, and the depth at the center is within about 280 m very near the original depth of 300 m (Figure 6.7c). The best inversion result can be achieved by using the original resistivity distribution at the center as starting model (Figure 6.7e). Here, the depth and the shape of the valley can be reconstructed as well as the location of the clay between 30–70 m depth. Only the parts from ± 1,000 m to ± 1,400 m do not conform to the original model. For that parts a 6-layer model would need to be taken.

The use of constraints improves the inversion results for all starting models. Especially for the first starting model the improvement is significant (Figure 6.7a and b). By constraining the resistivity of the underlying half-space to 5% the inversion was pushed to the correct direction and the shape of the valley is revealed. In Figure 6.7d the resistivities of the first and the fifth layer were constrained to 5% and thereby the base of the valley was pushed to the true depth of 300 m at the center. Between Figure 6.7e and f the improvement consists mainly in the reduction of the 2D effect at ± 1,400 m.

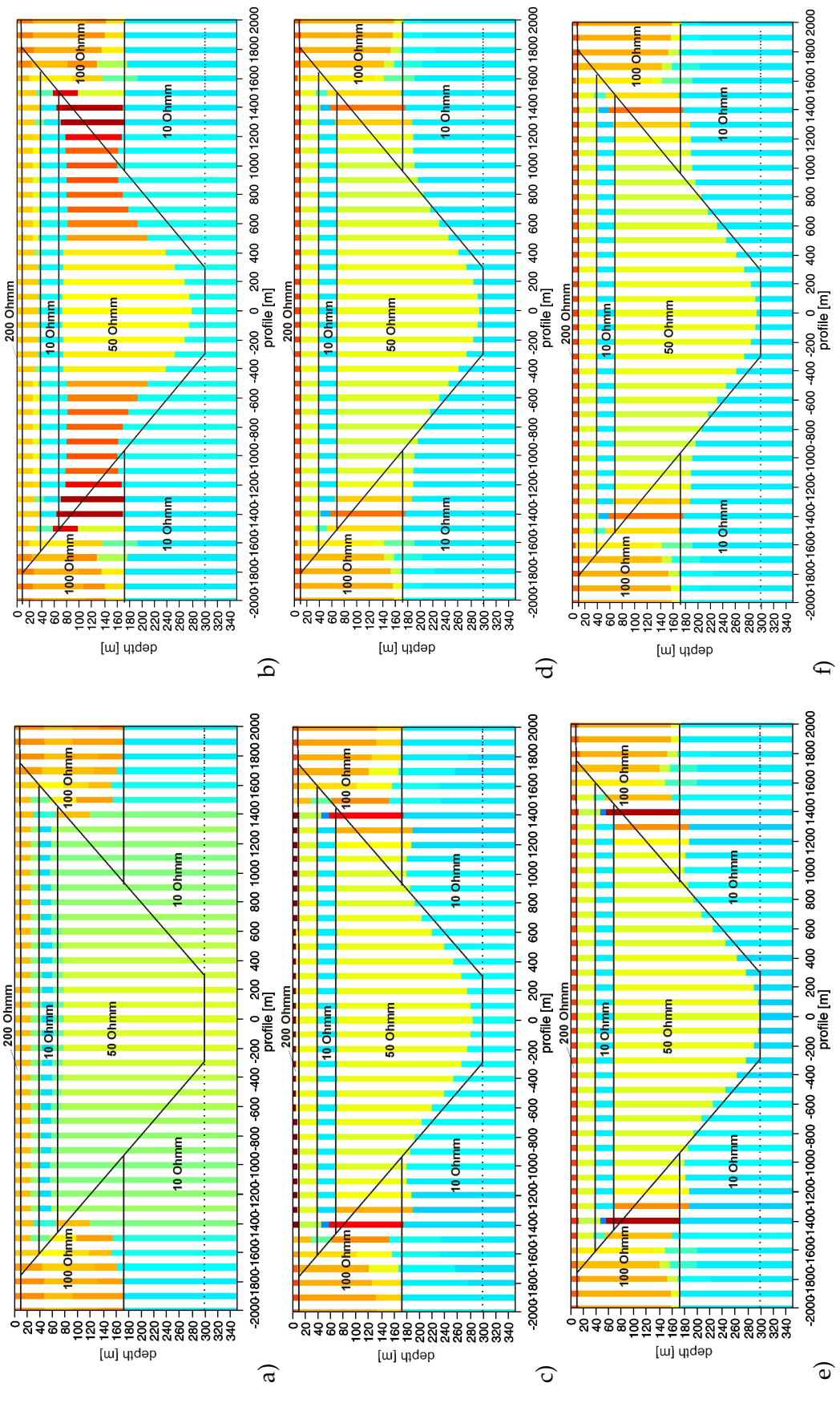

Figure 6.7: *1D inversion results of synthetic data of valley 08 with different starting models. The original valley model is indicated by solid lines and resistivity values.*
a) $\rho_i = (50, 50, 50, 50, 50)\ \Omega m$, $depth_i = (20, 40, 60, 80)\ m$, *b)* $\rho_i = (50, 50, 50, 50, 50)\ \Omega m$, $depth_i = (20, 40, 60, 80)\ m$, $c_{ref,\rho_5} = 1.5$,
c) $\rho_i = (20, 20, 20, 20, 20)\ \Omega m$, $depth_i = (10, 50, 50, 100)\ m$, *d)* $\rho_i = (20, 20, 20, 20, 20)\ \Omega m$, $depth_i = (10, 50, 50, 100)\ m$, $c_{ref,\rho_1,\rho_5} = 1.5$,
e) $\rho_i = (200, 50, 10, 50, 10)\ \Omega m$, $depth_i = (10, 40, 70, 300)\ m$, *f)* $\rho_i = (200, 50, 10, 50, 10)\ \Omega m$, $depth_i = (10, 40, 70, 300)\ m$, $c_{ref,\rho_1,\rho_5} = 1.5$.

6.4.2 Valley 07

The slope of Valley 07 is with an angle of 14° a little steeper. The 1D inversion results of the synthetic TEM data in Figure 6.8 demonstrate that also for this valley the inversion results can be improved by using constraints and the dependency of the starting model decreases. First, 5-layer models with homogeneous resistivities of 50 Ωm (Figure 6.8a and b), then, the original resistivity distribution at the center were used as starting models (Figure 6.8c and d). At Figure 6.8a and c the inversions were carried out without any constraints, at Figure 6.8b and d the first and/or the fifth resistivity was constrained to 5%.

Nevertheless, the danger of misusing the constraints should not be underestimated. If the geological variability is not considered and the constraints are set too strong, the resulting model is too smooth. Figure 6.8e shows an example of this. Here, the absolute constraints on $depth_4$ are set to 5 m, *i.e.*, $depth_4$ is not allowed to differ more than 5 m between neighboring models. This is not consistent with the 14° slope of the original model which has a variability of about 25 m depth on 100 m station distance. A variability of 5 m depth per 100 m station distance would correspond to a slope of $\alpha = \arctan(5/100) \approx 3°$.

6.4.3 Valley 06

Valley 06 has the steepest slope of 18°. Due to this, and to the fact that this valley is relative narrow with a base width of only 400 m, significant 2D effects occur in the 1D inversion results shown at Figure 6.9.

First, 5-layer models with homogeneous resistivities of 50 Ωm and 30 Ωm, then, the original resistivity distribution at the center were used as starting models. Generally the slope seems to be less steep and the base less wide. Depending on the starting model, the depth of the valley base can not be modeled (Figure 6.9a) or it occurs shallower, *e.g.*, at about 280 m depth (Figure 6.9c). According to the previous section that is consistent with the 2D effect in the data.

Again, the use of constraints improves the inversion results. Despite the initial half-space depth of 80 m, used in the starting model for Figure 6.9b, is faraway of the original model, this depth is pushed to the correct direction by constraining the resistivities of the fifth layers. Nevertheless, the valley base is modeled at 260 m depth, due to the 2D effect in the data simulating a shallower valley shape.

The clay layer between 40–70 m depth is reproduced by the inversion nearly independently of the starting model. Here, 2D effects occur at the edges (at ± 800–900 m of the profile).

The example of valley 06 shows that the exact reconstruction of a relative steep and narrow valley from synthetic data is hardly possible through 1D inversions. Even the use of constraints can only marginally improve the results.

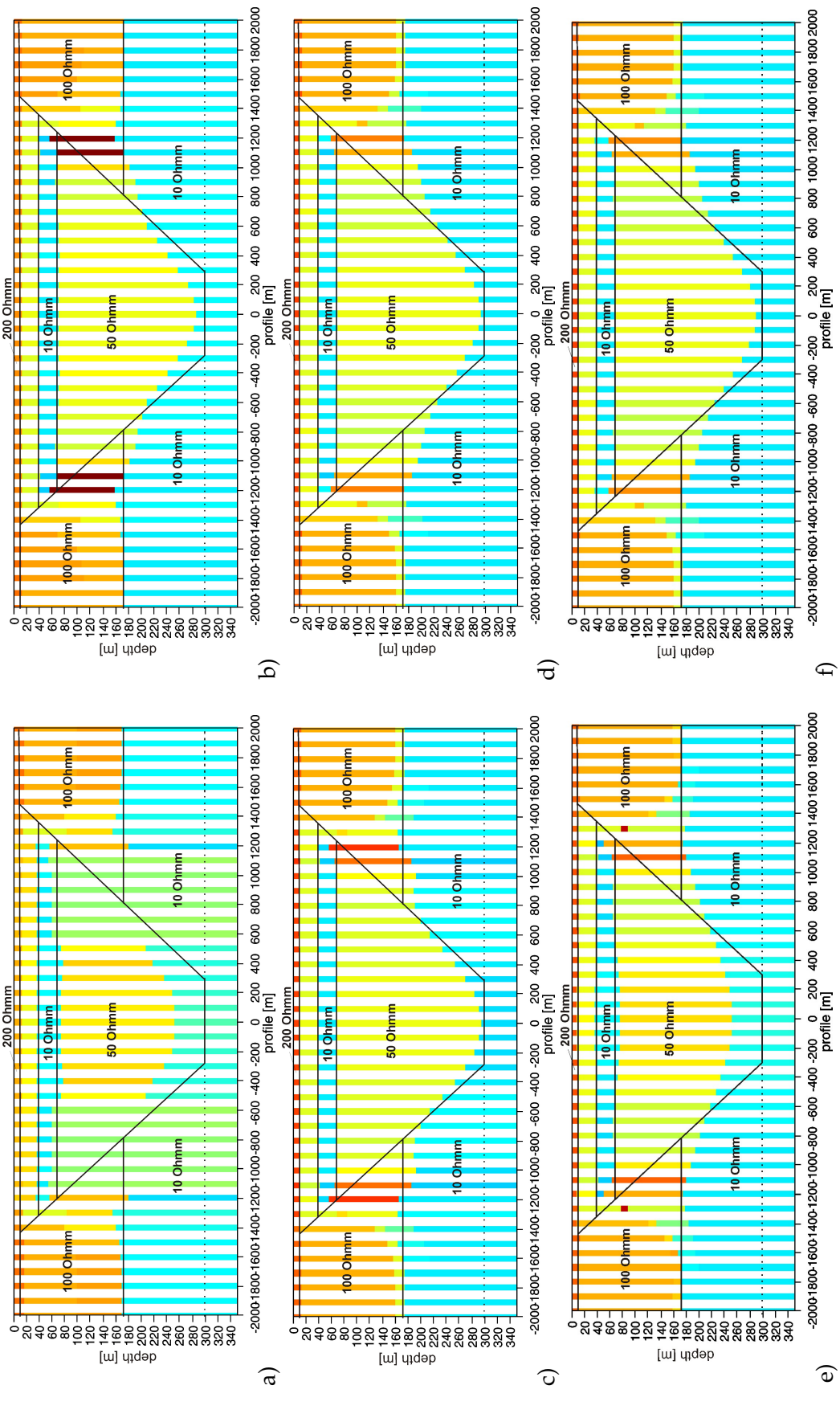

Figure 6.8: *1D inversion results of synthetic data of valley 07 with different starting models. The original valley model is indicated by solid lines and resistivity values.*
a) $\rho_i = (50, 50, 50, 50)\ \Omega m$, $depth_i = (10, 40, 70, 300)\ m$, *b)* $\rho_i = (50, 50, 50, 50)\ \Omega m$, $depth_i = (10, 40, 70, 300)\ m$, $c_{ref,\rho_1,\rho_5} = 1.5$,
c) $\rho_i = (200, 50, 10, 50, 10)\ \Omega m$, $depth_i = (10, 40, 70, 300)\ m$, *d)* $\rho_i = (200, 50, 10, 50, 10)\ \Omega m$, $depth_i = (10, 40, 70, 300)\ m$, $c_{ref,\rho_1,\rho_5} = 1.5$,
e) $\rho_i = (200, 50, 10, 50, 10)\ \Omega m$, $depth_i = (10, 40, 70, 300)\ m$, $c_{ref,\rho_1,\rho_5} = 1.5$, $c_{ref,d4} = 1.17\ (5\ m)$,
f) $\rho_i = (200, 50, 10, 50, 10)\ \Omega m$, $depth_i = (10, 40, 70, 300)\ m$, $c_{ref,\rho_1,\rho_5} = 1.5$, $c_{ref,d_4} = 1.67\ (20\ m)$.

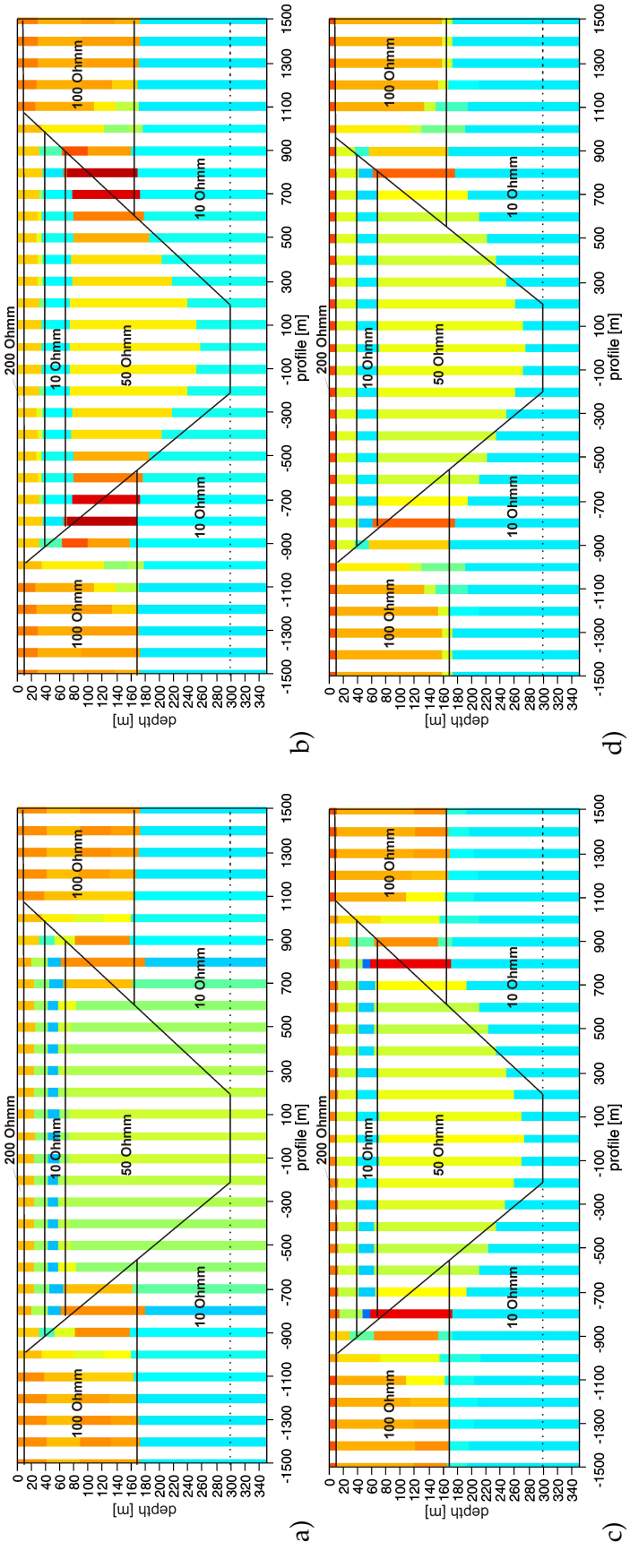

Figure 6.9: *1D inversion results of synthetic data of valley 06 with different starting models. The original valley model is indicated by solid lines and resistivity values. a)* $\rho_i = (50, 50, 50, 50)\ \Omega m$, $depth_i = (20, 40, 60, 80)\ m$, *b)* $\rho_i = (50, 50, 50, 50)\ \Omega m$, $depth_i = (20, 40, 60, 80)\ m$, $c_{ref,\rho_5} = 1.5$, *c)* $\rho_i = (30, 30, 30, 30)\ \Omega m$, $depth_i = (10, 40, 70, 300)\ m$, $c_{ref,\rho_5} = 1.5$, *d)* $\rho_i = (200, 50, 10, 50, 10)\ \Omega m$, $depth_i = (10, 40, 70, 300)\ m$, $c_{ref,\rho_1,\rho_5} = 1.5$.

6.5 Conclusion

A 3D modeling study of a buried valley showed the limitations of the 1D methods. I demonstrated that a 1D assumption is legitimated as long as the data are only slightly influenced by 2D effects. If the 2D effect in the data is greater than the data uncertainty, a 1D assumption can lead to misinterpretations, *e.g.*, a slower reducing transient, caused by the slopes of a steep valley, simulates a shallower valley and it is not possible to reconstruct a steep and narrow valley through 1D inversions.

Thus it can be understand, if the slopes of the Cuxhaven valley are not resolved correctly by SCI although the geological variability was considered that can be caused by 2D effects of the slope.

Chapter 7

Conclusions

Resistivity models derived from two different helicopter-borne electromagnetic methods were compared to each other and to ground-based resistivity models in a part of the Cuxhaven valley, northern Germany. Frequency-domain helicopter-borne EM data were inverted into layered earth resistivity models by applying the Marquardt-Levenberg inversion procedure routinely used at BGR. A similar single-site 1D inversion technique developed at University of Aarhus was used to invert ground-based and helicopter-borne TEM data. The CVES data were inverted using the laterally constrained inversion.

Although differently acquired geophysical data sets and different inversion techniques were applied, the inversion results of all methods are consistent in locating the top of a strong conductor, the Lauenburg clay, at 40 m depth having resistivities between 5–10 Ωm.

The thick Lauenburg clay layer reduces the EM investigation depths within the Cuxhaven valley. Where a thick clay layer exists, HEM is not always able to penetrate it completely using single-site 1D inversion. HEM and CVES provide detailed information about the resistivity distribution in the near-surface area and both detect a shallow conductor at 20 m depth, the Holstein clay. The existence of the clay layer is confirmed by a drilling and a resistivity log.

SkyTEM and TEM, however, are not able to resolve the shallow area of the valley. The TEM methods determine the base of the Lauenburg clay at 60 m depth and additionally a Tertiary clay layer outside the valley at about 180 m depth, but they fail to reveal the clay layer indicated by the lithological log at 115–145 m depth inside the valley.

Neither the frequency-domain method nor the normal-moment time-domain methods were able to reach the base of the valley using single-site inversions. Only high-moment ground-based TEM measurements determined a resistivity contrast at about 300 m depth. This kind of measurements, however, can only be carried out at a few distantly separated sites due to the bulky transmitter loop of 400 × 400 m.

To get more information out of the SkyTEM data I applied the SCI technique, which increases the inversion capabilities, particularly of noisy field data, and layers with

little information in the data are resolved better.

I showed, using SCI for the interpretation of the SkyTEM data that the modeling of the valley base is possible. Here, it is important to consider the geological variability and *a priori* information when defining the constraints to avoid misinterpretations. The question was, whether the result is caused by information in the data or as a product of the constraints. I showed by a 1D forward calculation that theoretically there is information in the data for the covered time range, but this is below the noise level in practice.

Furthermore, I adapted the concept of the SCI on HEM data. I showed that the modeling of the shallow Holstein clay layer is less dependent on the starting model compared to single-site inversion and that the base of the Lauenburg clay is definitely revealed by this technique. An outlook for HEM could be to replace the extensive leveling procedure by SCI.

By a TEM 3D modeling study of a buried valley I demonstrated the limitations of the 1D methods. I demonstrated that a 1D assumption is legitimated as long as the data are only slightly distorted and the 2D effect in the data is smaller than the data uncertainty. If the 2D effect in the data is greater than the data uncertainty, a 1D assumption can lead to misinterpretations.

This is clarified by the smoke-rings concept where the EM fields propagate downward and outward, depending on the resistivity distribution. The secondary field is induced by the current systems which extend with depth. Thus, the so-called *footprint* increases with depth. In the case of the modeled valley structures, the slopes may appear earlier in the data than the base, affecting a slower reducing transient due to the underlying conductive half-space. This simulates a shallower valley base. As long as the 3D effect is smaller than the data uncertainty (which is considered in the inversion), it is possible to model the valley base at the correct depth using a starting model based on *a priori* information.

In reality, there is not always *a priori* information available. I showed for the synthetic data that constraints help to push the model in the correct direction. In order to emphasize the importance of the consideration of the geological variability, I demonstrated the danger of misuse at an example, where too strong constraints on the depths result in a too shallow valley.

The technical potential of the SkyTEM system was not fully utilized in the Cuxhaven survey. The state of the art 2008 is a transmitter moment of 100,000–150,000 Am^2, which means a 15% increase in investigation depth can be achieved. Furthermore, the system now has the first time gate at 10 μs at standard measurements, and both horizontal and vertical components are measured and inverted.

The investigation depth of the HEM method is limited by the lowest frequency, but with lower frequencies the signal-to-noise ratio decreases and the weight of the system increases. The lowest HEM frequency used is of the order of 100 Hz [*Won et al.*, 2003], *i.e.*, an increase in investigation depth of about 45% compared to that of the BGR system is possible but technically challenging.

For both methods holds that a lower noise level would result in a higher investigation depth.

Airborne electromagnetic surveying rapidly produces resistivity maps with high lateral resolution. The HEM system is cost-efficient and fast, but the more expensive and time-consuming SkyTEM system can resolve deeper structures. Ground-based geophysical surveys are often more accurate, but are considerably slower and often more restricted than airborne surveys. The method or combination of methods used in a particular survey will depend on the targets of interest, time, budget, and man-power available. A combination of methods is often useful for obtaining a detailed understanding of the subsurface resistivity distribution.

Bibliography

Archie, G. E., The electrical resistivity log as an aid in determining some reservoir characteristics, *Trans. Am. Inst. Min. Metal. and Petr. Eng.*, *146*, 54–62, 1942.

Auken, E. and A. V. Christiansen, Layered and laterally constrained 2D inversion of resistivity data, *Geophysics*, *69*, 752–761, 2004.

Auken, E., L. Nebel, K. I. Sørensen, M. Breiner, L. Pellerin and N. Christensen, EMMA — A Geophysical Training and education Tool for Electromagnetic Modelling and Analysis, *Journal of Environmental and Engineering Geophysics*, *7*, (2), 57–68, 2002.

Auken, E., F. Jørgensen and K. I. Sørensen, Large-scale TEM investigation for groundwater, *Exploration Geophysics*, *34*, 188–194, 2003.

Auken, E., A. V. Christiansen, B. H. Jacobsen, N. Foget and K. I. Sørensen, Piecewise 1d laterally constrained inversion of resistivity data, *Geophysical Prospecting*, *53*, 497–506, 2005.

Besenecker, H., Bohrdatenbank Niedersachsen, Bohr-ID: 3028HY0304, technical report, Accessibility of the mining authority management of the State Authority for Mining, Energy and Geology (LBEG), Hannover, 1976.

Box, G. E. P., Robustness in the strategy of scientific model building, in *Robustness in Statistics*, edited by R. Launer and G. Wilkinson, Academic Press, New York, 1979.

Chen, J., A. Raiche, F. Sugeng and J. Macnae, Inverting aem data using a damped eigenparameter method, *Exploration Geophysics*, *29*, 128–132, 1998.

Christensen, N. B. and K. I. Sørensen, Surface and borehole electric and electromagnetic methods for hydro-geophysical investigations, *European Journal of Environmental and Engineering Geophysics*, *3*, 75–90, 1998.

Cofaigh, C. O., Tunnel valley genesis, *Progress in Physical Geography*, *20*, 1–19, 1996.

Commer, M., *Three-dimensional inversion of transient electromagnetic data: A comparative study*, Dissertation, University of Cologne, 2003.

Dahlin, T., 2D resistivity surveying for environmental and engineering applications, *First Break*, *14*, 275–284, 1996.

Danielsen, J. E., E. Auken, F. Jørgensen, V. Søndergaard and K. I. Sørensen, The application of the transient electromagnetic method in hydrogeophysical surveys, *Journal of Applied Geophysics*, *53*, 181–198, 2003.

Davis, J. L. and A. P. Annan, Ground-penetrating radar for high-resolution mapping of soil and rock stratigraphy, *Geophysical Prospecting*, *37*, 531–551, 1989.

Delaunay, B., *Bulletin of Academy of Sciences of the USSR 7*, chapter Sur la sphere vide, 793–800, Class. Sci. Math., 1934.

Dijke, J. J. v. and A. Veldkamp, Climate-controlled glacial erosion in the unconsolidated sediments of northwestern europe based on a genetic model for tunnel valley formation, *Earth Surface Processes and Landforms*, *21*, 327–340, 1996.

Druskin, V. L. and L. A. Knizhnerman, A spectral semidiscrete method for the numerical solution of 3-d nonstationary problems in electrical prospecting., *Phys. Sol. Earth*, *24*, 641–648, 1988.

Eberle, D. G. and B. Siemon, Identification of buried valleys using the bgr helicopter-borne geophysical system, *Near Surface Geophysics*, *4*, 125–133, 2006.

Ellis, R. G., Inversion of airborne electromagnetic data, *Exploration Geophysics*, *29*, 121–127, 1998.

Fitterman, D. V. and M. Deszcz-Pan, Using airborne and ground electromagnetic data to map hydrologic features in everglades national park, in *Proceedings of the Symposium on the Application of Geophysics to Engineering and Environmental Problems SAGEEP 2001, Denver (Colorado), Environmental and Engineering Geophysical Society*, 2001.

Fitterman, D. V. and M. T. Stewart, Transient electromagnetic sounding for groundwater, *Geophysics*, *51*, (4), 995–1005, 1986.

Flathe, H., Possibilities and limitations in applying geoelectrical methods to hydrogeological problems in the coastal areas of north west germany, *Geophysical Prospecting*, *3 (2)*, 95–110, 1955.

Fluche, B., Verbesserte Verfahren des direkten und des inversen Problems in der Hubschrauber-Elektromagnetik, in *Protokoll Kolloquium Elektromagnetische Tiefenforschung*, edited by V. Haak and J. Homilius, 249–266, 1990.

Fluche, B. and K.-P. Sengpiel, Grundlagen und Anwendungen der Hubschrauber-Geophysik, in *Umweltgeophysik*, edited by M. Beblo, 363–393, Ernst und Sohn, Berlin, 1997.

Foged, N., E. Auken and K. I. Sørensen, Skytem survey cuxhaven - data report. repro number 20041006, technical report, Department of Earth Sciences, University of Aarhus, Denmark, 2005.

Fountain, D., Airborne electromagnetic systems — 50 years of development, *Exploration Geophysics*, *29*, 1–11, 1998.

Fountain, D., 60 years of airborne EM — Focus on the last decade, in *AEM2008 - 5th International Conference on Airborne Elecrtomagnetics*, 2008.

Fraser, D. C., Resistivity mapping with an airborne multicoil electromagnetic system, *Geophysics*, *43*, 144–172, 1978.

Frischknecht, F., *Fields about an oscillating magnetic dipole over a two-layer earth, and application to ground and airborne electromagnetic surveys*, Quaterly of the Colorado School of Mines, 1967.

Frischknecht, F. C., V. F. Labson, B. R. Spies and W. L. Anderson, Profiling Methods Using Small Sources, in *Electromagnetic Methods in Applied Geophysics*, edited by M. N. Nabighian, Bd. 2, chapter 3, Soc. Expl. Geophys., 1991.

Gabriel, G., R. Kirsch, B. Siemon and H. Wiederhold, Geophysical investigation of buried Pleistocene subglacial valleys in Northern Germany, *Journal of Applied Geophysics*, *53*, 159–180, 2003.

Griffiths, D. H. and J. Turnbull, A multi-electrode array for resistivity surveying, *First Break*, *3*, 16–20, 1985.

Griffiths, D. H., J. Turnbull and A. I. Olayinka, Two-dimensional resistivity mapping with a computer- controlled array, *First Break*, *8*, 121–129, 1990.

HGG, Guide to processing and inversion of SkyTEM data, technical report, HydroGeophysics Group, Department of Earth Sciences, University of Aarhus, 2007*a*.

HGG, Manual for the inversion program em1dinv, technical report, HydroGeophysics Group, Department of Earth Sciences, University of Aarhus, 2007*b*.

HGG, Workbench, technical report, Hydrogeophysics Group, Department of Earth Sciences, University of Aarhus, Denmark, 2007*c*.

Hodges, G. and B. Siemon, Comparitive analysis of one-dimensional inversions of helicopter-borne frequency-domain electromagnetic data, in *AEM2008 — 5th International Conference on Airborne Electromagnetics, Finland*, 2008.

Hördt, A., V. L. Druskin and L. A. Knishnerman, Interpretation of 3-D effects on long-offset transient electromagnetic (LOTEM) soundings in the Münsterland area/Germany, *Geophysics*, *57*, 1127–1137, 1992.

Huang, H. and G. J. Palacky, Damped least-squares inversion of time-domain airborne EM data based on singular value decomposition, *Geophysical Prospecting*, *39*, 827–844, 1991.

Huuse, M. and H. Lykke-Andersen, Overdeepend quaternary valleys in the eastern danish north srea: morphology and origin, *Quaternary Science Review*, *19*, 1233–1253, 2000.

Jackson, D. D., The use of a priori data to resolve non-uniqueness in linear inversion, *Geophys. J. R. astr. Soc.*, *57*, 137–157, 1979.

Jäger, W., Elektrische Eigenschaften, in *Handbuch zur Erkundung des Untergrundes von Deponien und Altlasten - Geophysik*, edited by K. Knödel, H. Krummel, and G. Lange, Bd. 3, chapter 14.7, 986–992, Springer-Verlag, Berlin, 1997.

Johanson, H. K. and K. Sørensen, The fast Hankel transform, *Geophys. Prospect.*, *27*, 876–901, 1979.

Jørgensen, F. and P. Sandersen, Buried and open tunnel valleys in denmark- erosion beneath multiple ice sheets, *Quaternary Sciences Reviews*, *25*, 1339–1363, 2006.

Jørgensen, F., H. Lykke-Andersen, P. B. E. Sandersen, E. Auken and E. Nørmark, Geophysical investigations of buried quaternary valleys in denmark: an integrated application of transient electromagnetic soundings, reflection seismic surveys and exploratory drillings, *Journal of Applied Geophysics*, *53*, 215–228, 2003.

Jørgensen, F., R. Johnsen, J. Pedersen, J. F. Christensen and P. B. E. Sandersen, Tyrsting valley, in *Groundwater Resources in Buried Valleys – a Challenge for Geosciences*, edited by R. Kirsch, H.-M. Rumpel, W. Scheer, and H. Wiederhold, chapter 5.2, 181–190, Leibniz Institute for Applied Geophysics (LIAG), Hannover, Germany, 2006.

Jupp, D. L. B. and K. Vozoff, Stable iterative methods for the inversion of geophysical data, *Geophys. J. R. astr. Soc.*, *42*, 957–976, 1975.

Keller, G. V., Rock and mineral properties, in *Electromagnetic Methods in Applied Geophysics*, edited by M. N. Nabighian, Bd. 1, chapter 2, 13–51, Soc. Expl. Geophys., 1988.

Kirsch, R. and K. Hinsby, Aquifer vulnerability, in *Groundwater Resources in Buried Valleys – a Challenge for Geosciences*, edited by R. Kirsch, H.-M. Rumpel, W. Scheer, and H. Wiederhold, 149–155, Leibniz Institute for Applied Geophysics (LIAG), Hannover, Germany, 2006.

Kirsch, R., W. Scheer and H. Wiederhold, Introduction – buried valleys and the burval project, in *Groundwater Resources in Buried Valleys – a Challenge for Geosciences*, edited by R. Kirsch, H.-M. Rumpel, W. Scheer, and H. Wiederhold, 3–7, Leibniz Institute for Applied Geophysics (LIAG), Hannover, Germany, 2006.

Kjærstrup, M. and P. Erfurt, Bording valley, in *Groundwater Resources in Buried Valleys – a Challenge for Geosciences*, edited by R. Kirsch, H.-M. Rumpel, W. Scheer, and H. Wiederhold, 171–179, Leibniz Institute for Applied Geophysics (LIAG), Hannover, Germany, 2006.

Kuster, H. and K.-D. Meyer, Glaziäre Rinnen im mittleren und nordöstlichen Niedersachsen, *Eiszeitalter und Gegenwart*, *29*, 135–156, 1979.

Kuster, H. and K.-D. Meyer, Quartärgeologische Übersichtskarte von Niedersachsen und Bremen, 1:500000, Hannover, 1995.

Loke, M. H. and R. D. Barker, Rapid least-squares inversion of apparent resistivity pseudosections using a quasi-newton method, *Geophysical Prospecting*, *44*, 131–152, 1996.

Macnae, J., A. King, N. Stolz, A. Osmakoff and A. Blaha, Fast AEM data processing and inversion, *Exploration Geophysics*, *29*, 163–169, 1998.

Marquardt, D. W., An algorithm for least-squares estimation of non-linear parameters, *Journal of the Society for Industrial and Applied Mathematics*, *11*, 431–441, 1963.

Mbiyah, M. H., Time domain electromagnetic (TEM) measurements on a buried subglacial valley in Northern Germany, Diplomarbeit, Institute of Geohysics and Meteorology, University of Cologne, 2006.

McNeill, J. D., Use of Electromagnetic Methods for Groundwater Studies, in *Geotechnical and Environmental Geophysics — Volume I: Review and Tutoriel*, edited by S. H. Ward, Bd. no. 5 von *Investigations in geophysics*, Soc. Expl. Geophys., 1990.

Meju, M. A., *Geophysical Data Analysis: Understanding Inverse Problem Theory and Practice*, 6, Society of Exploration Geophysicists, Tulsa, 1994.

Meju, M. A., S. L. Fontes, M. F. B. Oliveira, J. P. R. Lima, E. U. Ulugergerli and A. A. Carrasquilla, Regional aquifer mapping using combined VES-TEM-AMT/EMAP methods in the semiarid eastern margin of Parnaiba, Brazil, *Geophysics*, *64*, (2), 337–356, 1999.

Menke, W., *Geophysical Data Analysis: Discrete Inverse Theory*, Academic Press Inc., Orlando, 1984.

Mundry, E., On the interpretation of airborne electromagnetic data for the two-layer case, *Geophyical Prospecting*, *32*, 336–346, 1984.

Nabighian, M. N. and J. C. Macnae, Time Domain Electromagnetic Prospecting Methods, in *Electromagnetic Methods in Applied Geophysics*, edited by M. N. Nabighian, Bd. 2, chapter 6, Soc. Expl. Geophys., 1991.

Nabighian, M. N. and J. C. Macnae, Electrical and EM methods, 1980-2005, *The Leading Edge*, *24*, 42–45, 2005.

Newman, G. A. and M. Commer, New advances in transient electromagnetic inversion, *Geophysical Journal International*, *160*, 5–32, 2005.

Nobes, D. C., Troubled waters, Environmental applications of electrical and electromagnetic methods, *Surveys in Geophysics*, *17*, 393–454, 1996.

Oristaglio, M. and B. Spies, *Three-dimensional electromagnetics, Geophysical development series: v. 7*, Soc. Expl. Geophys., Tulsa, 1999.

Palacky, G. J., Tutorial: Application in electrical and electromagnetic methods, *Geophys. Prospect.*, *31*, 861–872, 1983.

Palacky, G. J. and G. F. West, Airborne Electromagnetic Methods, in *Electromagnetic Methods in Applied Geophysics*, edited by M. N. Nabighian, Bd. 2, 811–879, Soc. Expl. Geophys., 1991.

Pellerin, L., Applications of electrical and electromagnetic methods for environmental and geotechnical investigations, *Surveys in Geophysics*, *23*, 101–132, 2002.

Piotrowski, J. A., Tunnel-Valley Formation in Northwest Germany – Geology, Mechanisms of Formation and Subglacial Bed Conditions for the Bornhoeved Tunnel Valley, *Sedimentary Geology*, *89*, 107–141, 1994.

Piotrowski, J. A., Subglacial hydrogeology in north-western Germany during the last glaciation: groundwater flow, tunnel valleys, and hydrological cycles, *Quaternary Sciences Reviews*, *16*, 169–185, 1997.

Rodi, W. and R. L. Mackie, Nonlinear conjugate gradients algorithm for 2-D magnetotelluric inversion, *Geophysics*, *66*, (1), 174–187, 2001.

Rumpel, H.-M., F. Binot, G. Gabriel, K. Hinsby, B. Siemon, A. Steuer and H. Wiederhold, Cuxhavener Rinne, in *Groundwater Resources in Buried Valleys – a Challenge for Geosciences*, edited by R. Kirsch, H.-M. Rumpel, W. Scheer, and H. Wiederhold, 227–239, Leibniz Institute for Applied Geophysics (LIAG), Hannover, Germany, 2006.

Sattel, D., A brief discussion of helicopter time-domain EM systems, in *Expanded Abstracts Book, Australian Earth Sciences Convention 2006, Melbourne, Australia*, 2006.

Scheer, W., J. Kröger, R. Kirsch and M. Zarth, Ellerbeker Rinne, in *Groundwater Resources in Buried Valleys – a Challenge for Geosciences*, edited by R. Kirsch, H.-M. Rumpel, W. Scheer, and H. Wiederhold, 205–226, Leibniz Institute for Applied Geophysics (LIAG), Hannover, Germany, 2006.

Schmucker, U., Anomalies of geomagnetic variations in the southwestern United States, *Bull. Sripps Inst. Oceanogr., Univ. Calif.*, *13*, 1–165, 1970.

Schwarz, G. and D. Krüger, Resistivity cross section through the southern central Andes as inferred from magnetotelluric and geomagnetic deep soundings, *J. Geophys. Res.*, *102*, (B6), 11,957–11,978, 1997.

Sengpiel, K.-P., Approximate inversion of airborne EM data from a multilayered ground, *Geophys. Prospect.*, *36*, 446–459, 1988.

Sengpiel, K.-P. and B. Siemon, Examples of 1D inversion of multifrequency AEM data from 3D resistivity distributions, *Exploration Geophysics*, *29*, 133–141, 1998.

Sengpiel, K.-P. and B. Siemon, Advanced inversion methods for airborne electromagnetic exploration, *Geophysics*, *65*, 1983–1992, 2000.

Siemon, B., Improved and new resistivity-depth profiles for helicopter electromagnetic data, *J. Appl. Geophys.*, *46*, 65–76, 2001.

Siemon, B., Electromagnetic methods – frequency domain: Airborne techniques, in *Groundwater Geophysics – A Tool for Hydrogeology*, edited by R. Kirsch, 155–170, Springer, Berlin, Heidelberg, 2006*a*.

Siemon, B., Frequency-domain helicopter-borne electromagnetics, in *Groundwater Resources in Buried Valleys – a Challenge for Geosciences*, edited by R. Kirsch, H.-M. Rumpel, W. Scheer, and H. Wiederhold, 89–98, Leibniz Institute for Applied Geophysics (LIAG), Hannover, Germany, 2006*b*.

Siemon, B., HEM data processing and interpretation at BGR, in *AEM Workshop Hannover 2006, Airborne EM - Recent Activities and Future Goals*, edited by A. Steuer and U. Meyer, BGR, 2006*c*.

Siemon, B., Levelling of helicopter-borne frequency-domain electromagnetic data, *Journal of Applied Geophysics*, doi: 10.1016/j.jappgeo.2007.11.001, 2007.

Siemon, B., C. Stuntebeck, K.-P. Sengpiel, B. Röttger and D. G. Eberle, Investigation of hazardous waste sites and their environment using the BGR helicopter geophysical system, *J. Environ. Eng. Geophys.*, *7*, 169–181, 2002.

Siemon, B., D. Eberle and F. Binot, Helicopter-borne electromagnetic investigation of coastal aquifers in North–West Germany, *Zeitschrift für Geologische Wissenschaften*, *32 (5/6)*, 385–395, 2004.

Siemon, B., E. Auken and A. Christiansen, Laterally constrained inversion of helicopter-borne electromagnetic data, *Journal of Applied Geophysics*, doi: 10.1016/j.jappgeo.2007.11.003, 2007*a*.

Siemon, B., A. Steuer, U. Meyer and H.-J. Rehli, HELP ACEH — a post-tsunami helicopter-borne groundwater project along the coasts of Aceh, Northern Sumatra, *Near Surface Geophys.*, *5*, 231–240, 2007*b*.

Siripunvaraporn, W. and G. Egbert, An efficient data-subspace inversion method for 2-D magnetotelluric data, *Geophysics*, *65*, 791–803, 2000.

Spies, B. R., Depth of investigation in electromagnetic sounding methods, *Geophysics*, *54*, 872–888, 1989.

Spies, B. R. and F. C. Frischknecht, Electromagnetic Sounding, in *Electromagentic Methods in Applied Geophysics*, edited by M. N. Nabighian, Bd. 2, chapter 5, Soc. Expl. Geophys., 1991.

Sørensen, K., Pulled Array Continuous Electrical Profiling, *First Break*, *14*, 85–90, 1996.

Sørensen, K. and E. Auken, SkyTEM – a new high-resolution helicopter transient electromagnetic system, *Exploration Geophysics*, *35*, 191–199, 2004.

Stadtler, C., F. Fielitz, B. Röttger, F. Schildknecht, B. Siemon and W. Voß, Hubschrauber- (HEM) und Transientelektromagnetische (TEM) Messungen zur Grundwassererkundung in Namibia, in *Abstract Book of the 64th Annual Meeting of the German Geophysical Association (DGG 2004), Berlin, HGP09*, 2004.

Steuer, A., Airborne and Ground-based Elecrtomagnetic Investigations of the Fresh-water Potential in the Tsunami-hit Area Sigli, Northern Sumatra, *J. Environ. Eng. Geophys.*, *13*, (1), 49–50, 2008.

Strack, K. M., *Exploration with Deep Transient Electromagnetics*, Methods in Geochemistry and Geophysics, Bd. 30, Elsevier, Amsterdam, 1992.

Tarantola, A., *Inverse Problem Theory and Methods for Model Parameter Estimation*, Society for Industrial and Applied Mathematics, Philadelphia, 2005.

Telford, W. M., L. P. Geldart and R. E. Sheriff, *Applied Geophysics*, Cambridge University Press, 2. Auflage, 1990.

Tezkan, B., A review of environmental application of quasi-stationary electromagnetic techniques, *Surveys in Geophys.*, *20*, 279–308, 1999.

Tezkan, B., M. H. Mbiyah, S. L. Helwig and R. Bergers, Time Domain Electromagnetic (TEM) Measurements on a buried subglacial valley in Northern Germany by using a large transmitter size and a high current., *submitted to ZDGG*, 2008.

Turberg, P., I. Müller and F. Flury, Hydrogeological investigation of porous environments by radio magnetotelluric-resistivity (RMT-R 12–240 kHz), *Journal of Applied Geophysics*, *31*, 133–143, 1994.

Valleau, C. V., Hem data processing — a practical overview, *Exploration geophysics*, *31*, 584–594, 2000.

Viezzoli, A., A. Christiansen, E. Auken and K. Sørensen, Quasi-3D modeling of airborne TEM data by spatially constrained inversion, *Geophysics*, *73*, F105–F113, 2008.

Wait, J. R., Propagation of radio waves over stratified ground, *Geophysics*, *18*, 416–422, 1953.

Wait, J., *Electromagnetic waves in stratified media*, Macmillan, New York, 1962.

Wait, J. R., *Geo-Electromagnetism*, Academic Press, New York, 1982.

Ward, S. H. and G. W. Hohmann, Electromagnetic theory for geophysical applications, in *Electromagnetic methods in applied geophysics*, edited by M. N. Nabighian, Bd. 1, chapter 4, 131–311, Soc. Expl. Geophys., 1988.

Waxman, M. H. and L. Smits, Electrical conductivities in oil-bearing shaly sands, *Trans. Am. Inst. Min., Met. and Petr. Eng.*, *243*, 107–122, 1968.

Weidelt, P., Einführung in die Elektromagnetik, Skript, Technical University of Braunschweig, Germany, 1988.

Weidelt, P., Geoelektrik, in *Handbuch zur Erkundung des Untergrundes von Deponien und Altlasten - Geophysik*, edited by K. Knödel, H. Krummel, and G. Lange, Bd. 3, chapter 5.1.5, 65–232, Springer-Verlag, Berlin, 1997.

Wiederhold, H., G. Agster, G. Gabriel, R. Kirsch, P. S. abd W. Südekum and W. Voss, Geophysikalische Erkundung eiszeitlicher Rinnen im südlichen Schleswig-Holstein, *Zeitschrift Angewandte Geologie*, *1*, 2002.

Wiederhold, H., G. Gabriel and M. Grinat, Geophysikalische Erkundung der Bremerhaven-Cuxhavener Rinne im Umfeld der Forschungsbohrung Cuxhaven, *Zeitschrift für Angewandte Geologie*, *1/2005*, 28–38, 2005.

Witherly, K., The Quest for the Holy Grail in Mining Geophysics: A review of the development and application of airborne EM systems over the last 50 years, *The Leading Edge*, *19*, 2000.

Won, I. J., A. Oren and F. Funak, Gem-2a: A programmable broadband helicopter-towed electromagnetic sensor, *Geophysics*, *68*, 1888–1895, 2003.

Xie, G. and J. Li, A new algorithm for 3-D nonlinear electromagnetic inversion, in *Three-dimensional electromagnetics*, edited by M. Oristaglio, B. Spies, and M. R. Cooper, 193–207, SEG, 1999.

Yin, C. and G. Hodges, Influence of displacement currents on the response of helicopter electromagnetic systems, *Geophysics*, *70*, G95–G100, 2005.

Yin, C. and G. Hodges, Simulated annealing for airborne EM inversion, *Geophysics*, *72*, 189–195, 2007.

Acknowledgments

I would like to thank Prof. Dr. Bülent Tezkan and Dr. Bernhard Siemon for being the doctoral thesis supervisor and for providing advice for this work. Especially Bernhard Siemon has supported me during the whole time of this work at the BGR. Also many thanks to Prof. Dr. Andreas Kemna for appraising this thesis.

The CVES, TEM, and SkyTEM surveys were part of the BURVAL project, which was co-financed by Interreg IIIB North Sea Programme of the European Regional Development Fund.

The HEM survey was funded by the Federal Institute for Geosciences and Natural Resources (BGR) and carried out by the BGR helicopter group, thanks to them all. I also thank my BGR colleagues Gert Sandmann, Robert Koch, and Hanno Schmidt for their assistance in the TEM survey.

The HydroGeophysics Group of Aarhus University provided the SkyTEM data. I thank especially Esben Auken, Nikolai Foged, and Joakim Westergaard for the instruction in SkyTEM processing and interpretation. Andrea Viezzoli for the introduction to SCI.

I thank Michael Grinat and Franz Binot of the Leibniz Institute for Applied Geophysics, for providing the CVES data and for assistance in the geological interpretation, respectively.

Thanks to Bernhard Siemon, Suzannah Toulmin, David Smith, Uwe Meyer, Katrin Schwalenberg, Heiko Backes, and Lars Nieradzik for their critical reviews which improved the manuscript.

At last thanks to my partner Thomas Kurz and my parents Christiane and Klaus Steuer.

Erklärung

Ich versichere, dass ich die von mir vorgelegte Dissertation selbständig angefertigt, die benutzten Quellen und Hilfsmittel vollständig angegeben und die Stellen der Arbeit — einschließlich Tabellen, Karten und Abbildungen —, die anderen Werken im Wortlaut oder dem Sinn nach entnommen sind, in jedem Einzelfall als Entlehnung kenntlich gemacht habe; dass diese Dissertation noch keiner anderen Fakultät oder Universität zur Prüfung vorgelegen hat; dass sie — abgesehen von unten angegebenen Teilpublikationen — noch nicht veröffentlicht worden ist sowie, dass ich eine solche Veröffentlichung vor Abschluss des Promotionsverfahrens nicht vornehmen werde. Die von mir vorgelegte Dissertation ist von Prof. Dr. Bülent Tezkan betreut worden.

Nachfolgend genannte Teilpublikation liegt vor:

Steuer, A., Siemon, B. and Auken, E., 2009. A comparison of helicopter-borne electromagnetics in frequency- and time-domain at the Cuxhaven Valley in Northern Germany. *Journal of Applied Geophysics*, 67, 194–205, doi: 10.1016/j.jappgeo.2007.07.001.

Ich versichere, dass ich alle Angaben wahrheitsgemäß nach bestem Wissen und Gewissen gemacht habe und verpflichte mich, jedmögliche, die obigen Angaben betreffenden Veränderungen, dem Dekanat unverzüglich mitzuteilen.

Hannover, 23. September 2008